The Role of Acidity, Viscosity, and Morphology on Atmospheric Aerosol Physicochemical Properties and Impacts

by

Ziying Lei

A dissertation submitted in partial fulfillment
of the requirements for the degree of
Doctor of Philosophy
(Environmental Health Science)
in the University of Michigan
2021

Doctoral Committee:

Associate Professor Andrew P. Ault, Co-Chair
Associate Professor Joseph T. Dvonch, Co-Chair
Associate Professor Richard L. Neitzel
Associate Professor Kerri A. Pratt
Professor Jason D. Surratt

Ziying Lei

lziying@umich.edu

ORCID iD: 0000-0003-3071-0698

Dedication

This dissertation is dedicated to my beloved parents, in gratitude for their unconditional love and endless support. Along with all hard working and respected professors and collaborators.

此论文献给我最亲爱的父母，感恩一路有你们无私的爱与陪伴

以及所有尊敬的教授和同事们

Acknowledgements

First and foremost, I would like to express my sincere gratitude to my Ph.D. advisor, Dr. Andrew Ault, for all your mentorship and encouragement in the past years. Your motivation, immense knowledge, and passion for science has always inspired me and helped me to grow as an independent research scientist. Your advice on both research as well as on my career have been invaluable. Without your mentorship and hard work my graduate school success would not have been possible, and for that I will forever be grateful.

I would also like to thank my dissertation committee, Dr. Joseph Dvonch, Dr. Kerri Pratt, Dr. Jason Surratt, and Dr. Richard Neitzl for your advice and support as I progressed through this program. Specifically, I would like to thank Dr. Jason Surratt, who is collaborator on my research projects since I came to Michigan. You have provided extensive guidance and feedback on much of my work, and it has been a great pleasure working with you. To Dr. Mark Banaszak Holl, thank you for inviting me to Australia and allowing me to use the fascinating instrument in your lab, which was a wonderful research experience during my Ph.D. life.

I would like to thank my Michigan family, the supportive group of Ault and Pratt lab members, for your care and help throughout graduate school. I am very lucky and truly grateful to have you all in my life, you are not just great colleagues but even better friends. When I moved to Michigan alone I never imagined having such a colorful and joyful life with you all. To my life-long friend Dr. Nicole Olson, who has been an amazing friend since I joined the lab, I loved doing research, participating in field studies, attending conferences, and planning fun activities with you. We have created so many memories in the past several years that are very precious to me. To

Madeline Cooke, for always being such a sweet friend to me, I will surely miss cooking dinner and baking bread with you! To Jia Shi, for making the best fried chicken, bringing me pastries from New York, and all your support with my car maintenance. To Yao, for hosting BBQ parties and allowing me to hang out with Coco whenever I'm stressed. To Jamy, for hosting a Friendsgiving party and being a supportive friend. To Dr Daun Jeong, for always making me laugh and giving me advice to be a stronger woman! To Yilin Han, for bringing me cookies and bubble tea when I was working late in the lab at night, going on a fun trip with me to Pictured Rock, and taking many great photos. To Dr. Becky Craig, Rachel Kirpes, Kim Daley, and Alison Fankhauser, thank you for all your support and help as mentors during my Ph.D. program, I have learned a lot from you! To Dr. Isabel Colon-Bernal, Taeyong Ahn, Jinhee Kim, thank you for teaching me how to use microspectroscopy and helping me deeply understand the instrument. Ted and Jinhee, thanks for showing me around in Melbourne where I had a great time during my visit. To Dr. Yuzhi Chen, I have greatly enjoyed every summer when we worked together in the lab, grabbed coffee across the street, and hung out at conferences. To Dr. Yue Zhang, thank you for being a great friend and supporting me in many ways, I am so excited to continue doing research with you! To Ryan Ward, our friendship started at the first conference I went to, thanks for sharing all the fun moments in your life with me.

To a few very special and important people in my life, Amy, I can never appreciate enough for your kindness and all the joys we shared. Although we are not sisters by birth, I have always felt that we are sisters by heart. Thank you for always being there for me, I will always remember the jokes, adventures, laughs, and tears we experienced. Danni Li, my best friend in China, I cherished the time we spent together when I flew back to China and thank you for everything, I was so happy that I could attend your wedding virtually and give you my best wishes. To my

master advisor Dr. Andrew May. I feel incredibly lucky to have you as my first mentor in the U.S., you inspired me and showed me the ropes to overcome all the challenges I faced. You have taught and encouraged me so much that I could never thank you enough. To Monica and Tom Cooke, for spending Christmas with me and all the gifts, making me cookies, your kindness and love makes me feel at home. To Karen Irion, for all your care packages from New Orleans and all your love. To Luke Gerkman, a special guy who brought me so much happiness and laughter. Thank you for all your love and care, for inspiring me to be a better person with a kind heart, for enjoying the fun of life and many adventures together. I feel so lucky and grateful for having you in my life and cannot wait to start our new life journey!

Lastly but most importantly, I want to thank my family for all their unconditional love, support, and encouragement throughout my entire life. Thank you to my grandparents for always believing in me and being proud of me. To my cousins, for all the fun we had when we reunited during holidays, I feel less lonely being far away from home because of you. To mom, you have made me become a strong, confident, and independent woman. Seeing you on the video call every week and sharing my life with you became an important routine for me since I moved across the Pacific Ocean. I cannot describe in words what and how much you mean to me, you have given me everything I could ever ask for. I want you to know that a long distance will never make our hearts grow apart and I love you, always and forever! To dad, thank you for always spoiling me and helping me chase my dreams. Without your encouragement and generosity, I could not accomplish this much and have a successful career in science. I always remember that you taught me to never give up and hang in there a little longer because I am closer to success than I may think. I appreciate you more than words can ever say and you are the greatest man I have ever known. I am truly blessed to have the most amazing parents and my life is fulfilled with your love

and happiness. I want to give the sincerest thank you from the bottom of my heart to my dear parents!

Table of Contents

List of Figures

List of Tables

List of Equations

List of Appendices

Abstract

Atmospheric aerosol plays a critical role in Earth's climate by scattering or absorbing solar radiation, acting as cloud condensation and ice nuclei, and impacting air quality and public health. The physicochemical properties of aerosols dictate their climate and health impacts yet are challenging to measure accurately and quantitatively due to the complex nature of atmospheric aerosol. Specifically, the chemical composition, size, morphology, acidity, and viscosity have great interparticle variation. Methods enabling detailed quantitative investigation of individual aerosol properties are needed to understand the chemical transformation and climate effects of atmospheric aerosol. In this dissertation, atmospherically-relevant aerosol particles were examined using various state-of-the-art microspectroscopic techniques to measure the acidity, morphology, and viscosity of individual submicron particles, allowing better prediction of the climate and health impacts.

The acidity of aerosol is a critical property that affects the chemistry and composition of the atmosphere. However, there are challenges with quantifying aerosol acidity in individual particles due to the extremely small volumes of fine aerosol particles that have limited pH measurements. A novel single-particle acidity measurement was explored using the degradation of a pH-sensitive polymer. Submicron particles of known pH values (0 or 6) were deposited on a polymer thin film to erode the film. Particles were then rinsed off and the degradation of the polymer was characterized using atomic force microscopy (AFM) and Raman microspectroscopy. Acidic particles (pH=0) caused the polymer to degrade while near neutral particles (pH =6) did not. As particle size decreased, polymer degradation increased, indicating an increase in aerosol acidity at smaller particle diameters.

To further understand the impacts of aerosol acidity on the formation and evolution of secondary organic aerosol (SOA), inorganic sulfate particles with varying acidities (pH 1, 2, 3, and 5) reacted with gaseous isoprene-derived epoxydiols (IEPOX) for a range of times (30, 60, and 120 minutes). The morphology and chemical composition were systematically characterized at a single-particle level using AFM with photothermal infrared spectroscopy (AFM-PTIR) and

Raman microspectroscopy. Core-shell morphology of SOA particles was observed under acidic conditions after the IEPOX uptake and increasing aerosol acidity led to an increase in SOA viscosity and higher yield of organosulfates. These physicochemical properties have the potential to significantly alter the climate properties of the SOA particles.

To examine the effects of physicochemical properties in more complex atmospheric particles, the morphology and viscosity of submicron SOA from four different volatile organic compounds precursors (α-pinene, β-caryophyllene, isoprene, and toluene) were characterized before and after exposure to IEPOX. Dramatic morphological modifications were observed after the reactive uptake of IEPOX. SOA derived from α-pinene and β-caryophyllene were less viscous after IEPOX reactive uptake, while the viscosities did not change for isoprene and toluene-derived SOA. Additionally, a new glass transition temperature measurement was developed to reveal the viscosity of individual particles. The glass transition temperatures of atmospheric particles were measured for the first time under ambient atmospheric conditions using AFM-PTIR with thermal analysis.

The methods developed in this dissertation and their application to the study of atmospheric aerosol yield a wide range of possibilities to connect the physicochemical properties of aerosol particles with their chemical transformation processes and climate effects. Such characterization of individual submicron SOA particles provides new insights into the multiphase atmospheric processes and the ice nucleation/cloud formation of complex particles in the atmosphere.

Chapter 1. Introduction

1.1 Characteristics of Atmospheric Aerosol

Atmospheric aerosol, also known as particulate matter (PM), is any solid or liquid particles suspended in the air that has a wide range of sizes from 1 nm to 100 μm in diameter.[1,2] Atmospheric aerosols with submicron size in dimeter have strong impact on climate by scattering or absorbing solar radiation and can also act as cloud condensation nuclei (CCN) or ice nucleating particles (INP).[2-4] According to estimates of the global radiative forcing (Figure 1.1), there are large uncertainties in predicting the climate effects of atmospheric aerosols due to their complex nature.[5] In addition to climate impacts, exposure to atmospheric aerosol particles is linked to adverse health effects, which lead to over four million global deaths annually, primarily from high concentrations of atmospheric aerosols. [6-9] The World Health Organization identified atmospheric aerosols as targets for mitigation efforts to reduce global health risks.[6] Specifically, atmospheric aerosols can cause oxidative stress, as well as respiratory and cardiovascular diseases due to the complex chemical and physical properties of aerosol.[10-14] Despite significant research advances in characterizing atmospheric aerosols, detailed knowledge of many key atmospheric processes remains incomplete. Improving the understanding of the chemical and physical properties of individual atmospheric aerosols is important to reduce the uncertainties of climate and health effects.

Atmospheric aerosols are formed from a variety of natural and anthropogenic sources, such as biomass burning, volcanic dust, desert dust, or fossil fuel combustion.[14-16] Primary aerosols are directly emitted into the atmosphere, whereas secondary aerosols are formed through oxidation, condensation, and multiphase chemical processes of gaseous precursors.[14,16] One of the most common types of secondary aerosol, secondary organic aerosol (SOA), is primarily formed after oxidation of volatile organic compounds (VOCs), resulting in low volatility products that either condense or undergo reactive uptake to existing inorganic particles (e.g., ammonium sulfate).[17,18]

In addition to secondary aerosol formation, particles can undergo modifications during multiphase processing which leads to changes in their physicochemical properties.[19-21]

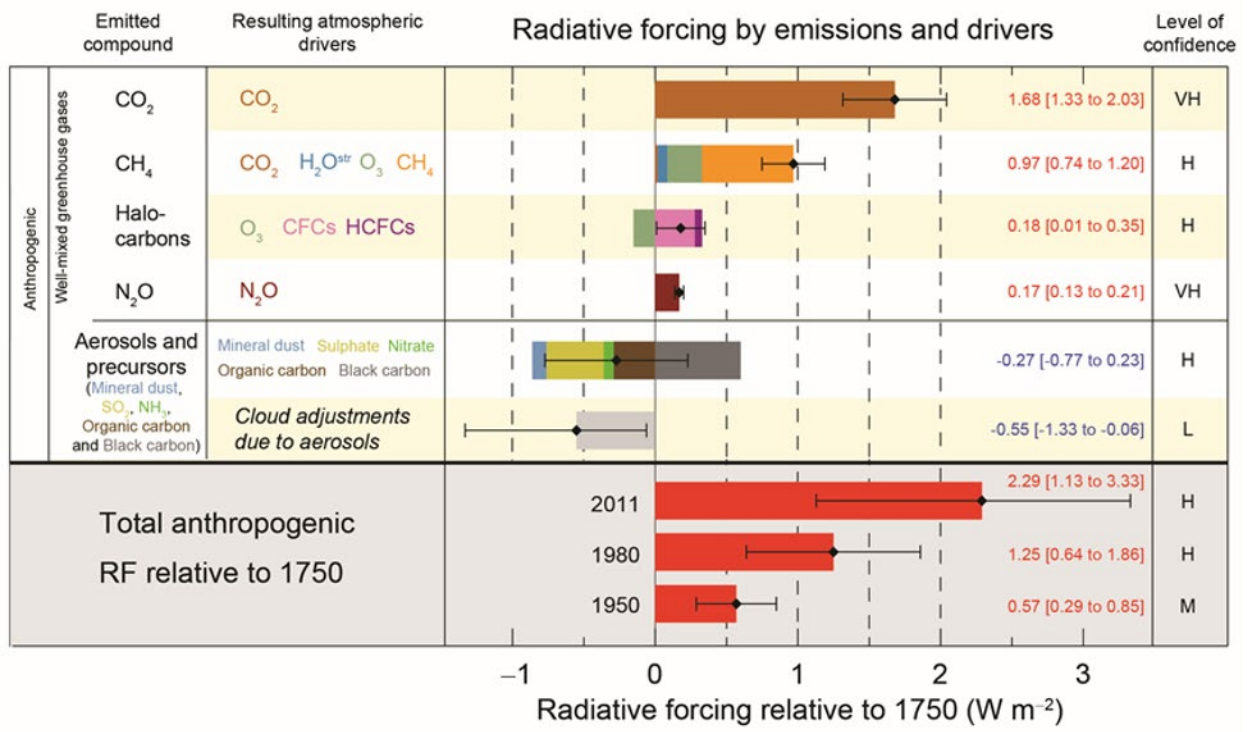

Figure 1.1 Radiative forcing estimates and uncertainties for greenhouse gases and aerosols. Reproduced from Stocker et al.[22]

1.2 Aerosol Physicochemical Properties

1.2.1 Aerosol Acidity

Aerosol acidity (pH) is a critical property that determines the amount of SOA formation, as many of the key reactions are pH-dependent.[23-25] For example, acid-catalyzed ring opening reactions of epoxides that are taken up into particles have lifetimes that are seconds in acidic particles, but days long in neutral particles.[26] The ability to definitively state whether aerosols have a pH < 2 (highly acidic) would be transformative for the field of atmospheric chemistry, as the lifetime of key secondary precursor species range over multiple orders of magnitude. The importance of acidity has been identified primarily from studies in laboratory environmental chambers,[24,27-29] where the acidic inorganic particles enhanced the amount of SOA formation. Prior results show that more acidic "seed" particles lead to greater SOA formation in comparison to neutral seed particles.[30] However, there remains uncertainty regarding the role of acidity as other

aerosol components have also been connected to SOA formation. This key uncertainty limits the prediction of atmospheric particle burden and climate impacts. In addition, studies have shown that aerosol pH can impact health through the dissolution of metals in atmospheric fine particles,[31] leading to formation of reactive oxygen species which lead to negative health effects. Further study of aerosol acidity is needed to understand its impact on climate and health through secondary aerosol formation (Figure 1.2).

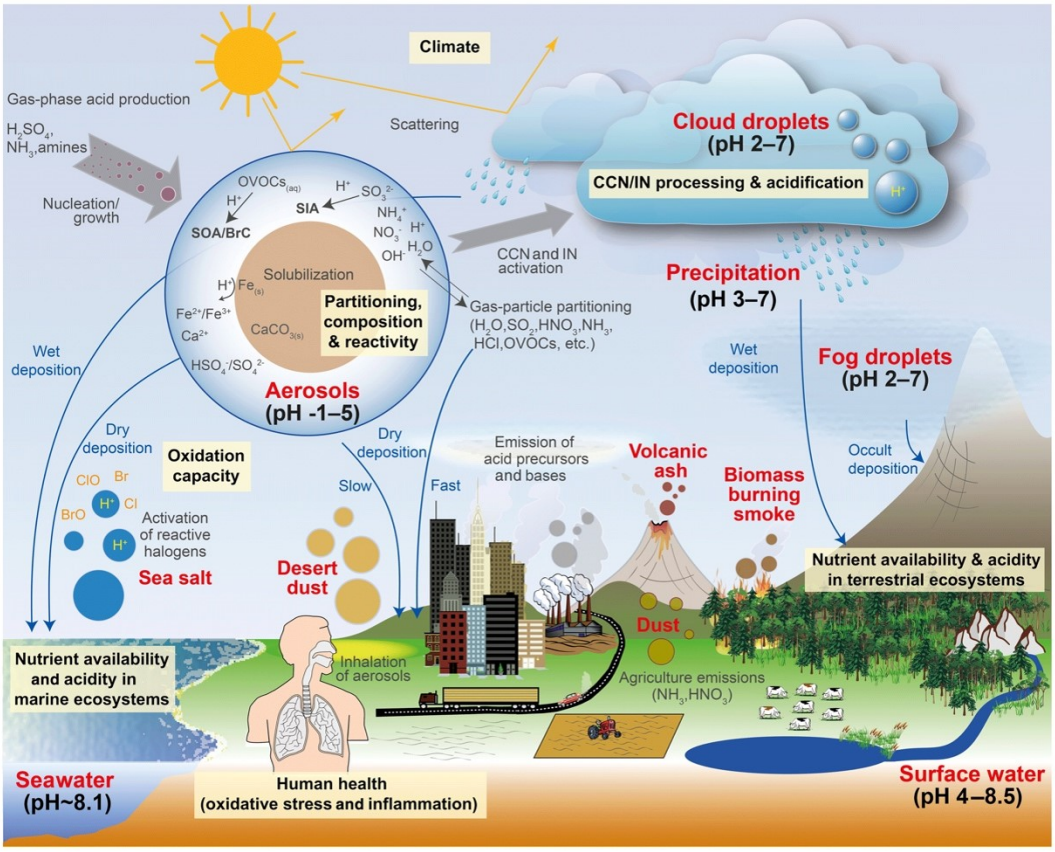

Figure 1.2 Sources and receptors of aerosol and cloud droplet acidity. Major primary sources and occurrence in the atmosphere are identified in bold red text: sea salt, dust, and biomass burning (sources); and aerosols, fog droplets, cloud droplets, and precipitation (occurrence).Key aerosol processes are indicated by arrows and grey text: nucleation/growth, light scattering, cloud condensation nuclei (CCN) and ice nuclei (IN) activation, and gas–particle partitioning. Sinks (wet, dry, and occult deposition) are indicated by blue lines and text. The effects that aerosols have in the atmosphere, and on terrestrial and marine ecosystems and human health, are highlighted in pale yellow boxes. Approximate pH ranges of aqueous aerosols and droplets, seawater, and terrestrial surface waters are also given. Reproduced from Pye et al.[32]

Despite the importance of atmospheric aerosol acidity for climate and health, scientific understanding is limited by the lack of accurate methods for directly measuring aerosol acidity. Recently, a method for the direct pH measurement of individual laboratory-generated aerosols was

developed utilizing an acid-conjugate base approach with Raman microspectroscopy (Figure 1.3).[33,34] However, this method has been limited to particles with diameters > 2.5 μm and simple systems with only a few components, due to the use of optical microscopy methods that are diffraction-limited (e.g. Raman microspectroscopy at 532 nm).[30,31] This is a major limitation of prior studies as most pH-sensitive PM formation occurs in fine particles (<2.5 μm), which have complex chemical compositions that often contain thousands of species in a single particle.[32] Another direct, near real-time aerosol pH measurement has been developed using a colorimetric approach involving a pH indicator and cell phone camera.[33] This method has been applied to measure submicron ambient particles (<0.4 μm), but is a bulk measurement technique. In addition, it requires samples to have a particulate mass of 65 μg for fine particles (<2.5 μm) with sufficient aerosol liquid water content for changes in the pH indicator color. Therefore, a new method was explored to determine acidity of submicron individual aerosol particles using pH sensitive polymer with atomic force microscopy (Chapter 2). Improved analytical techniques are still needed to measure individual submicron aerosol particles, particularly given the range and constantly evolving chemical composition of submicron atmospheric particles.

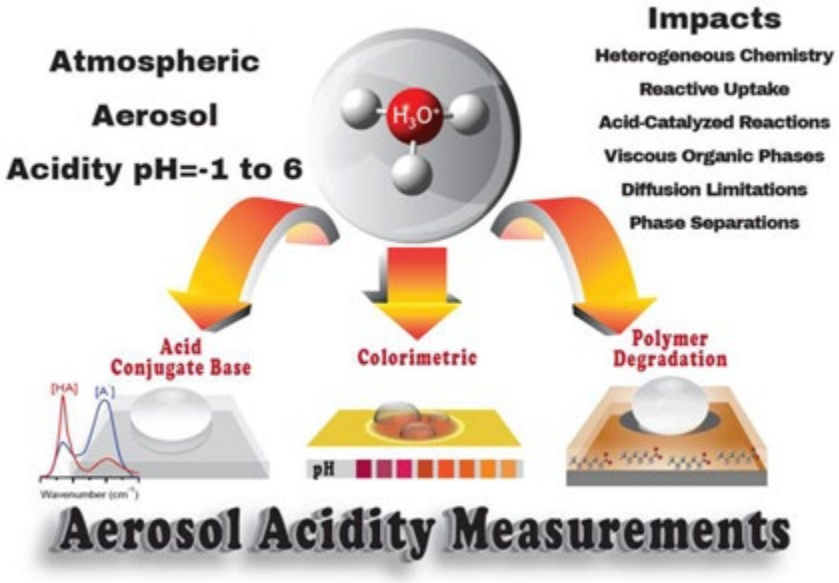

Figure 1.3 Novel pH measurements of aerosol particles including acid conjugate base method using Raman Microspectroscopy; colorimetric method, and polymer degradation method using atomic force microscopy. Reproduced from Ault et al.[35]

1.2.2 Aerosol Morphology

The morphology of aerosol particles has been intensively studied in recent years as it plays a critical role in heterogeneous chemistry that occurs in the atmosphere.[19-21,36-41] It is important to characterize aerosol morphology in order to incorporate it into regional- and global-scale atmospheric chemistry models that are designed to predict the amount of aerosol mass, which have direct implications for determining the effects of aerosol on air quality, climate, and human health. Aerosol particles can have a range of possible morphologies, including spherical shape (e.g., SOA), crystals (e.g., salt), or chain agglomerates (e.g., soot).[42-44] In the atmosphere, particles containing both organic and inorganic components can undergo phase transitions including deliquescence, efflorescence, and liquid-liquid phase separation (LLPS) based on the ambient relative humidity (RH).[36,45-48] Atmospheric phase separated particles usually present core-shell morphology, which occurs when organic components (i.e., shell) coat onto inorganic species (e.g., core).[40,49] Other morphologies such as homogenous, partially engulfed, and triphasic morphology have been observed during heterogenous reactions from laboratory studies,[50,51] demonstrating that aerosol morphology can impact multiphase chemistry leading to SOA formation. Different morphologies of aerosols can also influence the gas/particle partitioning of semi-volatile organic compounds,[19,52] heterogenous chemistry reaction rate,[21,53] and water uptake.[54]

1.2.3 Aerosol Viscosity and Phase State

The viscosity of aerosol particles and their phase state are fundamental properties that affect aerosol lifetime and particle growth.[55-57] Differing viscosities within particles can lead to a variety of phase states, such as liquid, semi-solid, and solid.[58] In the past decades, atmospheric aerosol particles were considered highly viscous semi-solid or even amorphous solid particles, until recent studies showed evidence of liquid atmospheric particles with low viscosity.[59-61] Atmospheric aerosol particles can have a wide range of viscosities (η), spanning over many orders of magnitude from liquid (i.e., liquid water, 10^{-3} Pa s) to solid (i.e., glass marbles, $>10^{12}$ Pa s).[58,62-67] Understanding the viscosity of atmospheric aerosol is critical to predicting their atmospheric impacts. For instance, the rates of particle growth and evaporation are dependent on their viscosity,[68,69] where liquid particles with low viscosity are more responsive to changes in gas phase composition and water uptake,[39,70] which have direct implications for air quality, visibility, and climate.

1.3 Physicochemical Characterization of Individual Aerosol Particles

Physicochemical properties of individual aerosol particles can be characterized by single-particle microscopic and spectroscopic techniques.[71] Microscopy usually provides physical properties of aerosol particles (i.e., morphology, phase state, size), while spectroscopy can provide detailed chemical information based on the different functional groups present in the particle.[72-78] The non-destructive nature of microspectroscopic technique under ambient pressure and temperature allows the same sample to be analyzed by multiple techniques.[34,78] Microscopic and spectroscopic analysis are offline techniques, which require collecting particles onto substrates using a size-resolved aerosol impactor. The single-particle microscopy and spectroscopy techniques used in this dissertation are introduced below.

1.3.1 Raman Microspectroscopy

Raman microspectroscopy has been frequently used to characterize morphology, size and chemical composition of aerosol particles using an optical microscope combined with vibrational spectra that identify different functional groups in individual particles.[34,72,74,79-81] Raman microspectroscopy probes molecular vibrations to provide information on covalently bonded inorganic and organic species. Previous studies show that Raman spectroscopy can differentiate species in slightly different bonding environments (i.e., $NaNO_3$ vs. NO_3^-)[82] and determine the pH of individual particles based on the relative abundances of acids and their conjugate bases.[34,74] The sensitivity and high spatial resolution have allowed for characterizing complex aerosol particles with core-shell morphology and differentiating the chemical compositions in the particle core and shell.[19] Chemical mapping can also be performed to study the distribution of specific molecular species within an individual aerosol particle (Figure 1.4).[83,84] Furthermore, Raman analysis is performed under ambient pressure and temperature that can prevent particle distortion. In addition, a relative humidity (RH) cell can be added to Raman microspectroscoy to study hygroscopic growth of aerosol particles.[34] In order to provide more quantitative analysis, a computer-controlled method (CC-Raman) was developed that can analyze hundreds of particles per sample.[85] Due to the diffraction limit of visible light,Raman microspectroscopy is typically limited to particles larger than 1μm. Thus, surface enhanced Raman spectroscopy (SERS) and tip enhanced Raman spectroscopy (TERS) were developed to allow for analysis of submicron particles.[84,86,87] However, the uneven enhancements add difficulty to perform quantitative measurements, and some mineral

dust or biologic particles are likely to fluoresce,[88,89] which often overwhelms the Raman signal. Thus, other vibrational spectroscopy techniques will be used to complement Raman microspectroscopy, such as infrared spectroscopy.

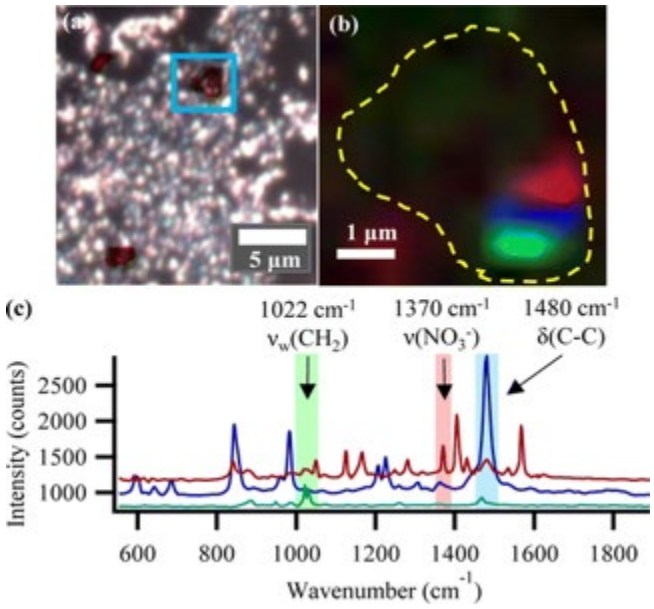

Figure 1.4 Raman microspectroscopy analysis of an aerosol particle with highlighted region showing the location, chemical distribution, and detailed chemical composition characterization. a). Optical image of aerosol particle, (highlighted in red) against SERS substrates, and mapped area (blue box). b) Map of the aerosol particle (outlined in yellow dashes) showing the location of three different enhanced chemical species at 1022 cm^{-1} (green), 1370 cm^{-1} (red), and 1480 cm^{-1} (blue). c) Raman spectra accompanying the mapped intensities. Reproduced from Craig et al.[84]

1.3.2 Atomic Force Microscopy Photothermal Infrared Spectroscopy (AFM-PTIR)

Atomic force microscopy with photothermal infrared spectroscopy (AFM-PTIR) is a powerful tool for single particle analysis, which can not only provide the morphology of individual particles down to 30 nm but also the chemical composition within the particle.[90-92] AFM-PTIR is based on detecting the photothermal expansion of an individual particle by a tunable IR laser with AFM probe (Figure 1.5).[73] This technique has been widely applied to study atmospheric aerosol particles,[73] polymer degradation,[93] particle hygroscopicity,[94,95] and particle phase state.[19,21,96] AFM-PTIR can collect spatial distribution of the measured functional groups within a particle through its high resolution spectral images and maps under ambient conditions.[97] Additionally, different AFM probes can be used to characterize physical properties of individual particles,[73,91,92] including surface tension[98,99] and nano thermal analysis.[72,100-102] The nano thermal analysis was applied to atmospheric aerosol particles for the first time in this work to reveal particle viscosity

(Chapter 5). AFM-PTIR has shown the potential to advance current understanding of atmospheric particles and their impacts on climate and public health.

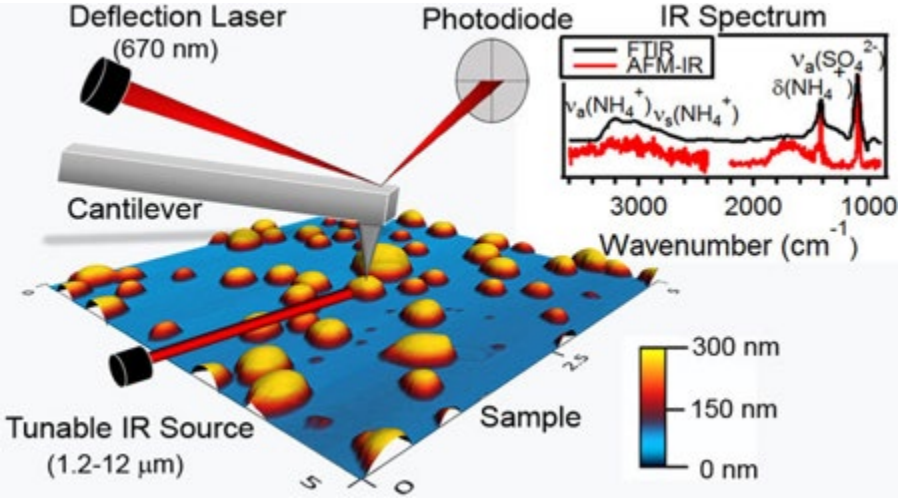

Figure 1.5 Schematic of AFM-IR operation. Local thermal expansion from the IR laser is detected by the cantilever, allowing IR spectra with ~50 nm resolution to be collected. IR spectra were collected from individual $(NH_4)_2SO_4$ particles using AFM-IR (this study) and micro-FTIR. Reproduced from Bondy et al.[73]

1.3.3 Optical Photothermal Infrared Spectroscopy (O-PTIR)

Recently a new breakthrough technique, optical photothermal infrared spectroscopy (O-PTIR), has been developed.[78] This non-contact analytical method uses changes in the scattering intensity of a continuous wave visible laser to detect the photothermal expansion when a tunable IR laser was applied to excite vibrational modes (Figure 1.6).[78,103-105] The modulated photothermal expansion causes the change in the intensity of the elastically (Rayleigh) scattered light, which can be processed to generate an IR spectrum. Meanwhile, inelastically (Stokes) scattered photons are also generated and collected simultaneously to obtain a Raman spectrum at the same location on the sample as the PTIR spectrum. Because the spatial resolution is determined by the visible laser, this technique overcomes the key limitation of traditional IR microscopy and improves spatial resolution to ~ 500 nm.[106] Similar to the techniques mentioned above, O-PTIR also can provide detailed characterization of chemical composition for individual submicron particles and specific vibrational modes within individual particles,[105,107,108] which allow us to further understand particle physicochemical properties. O-PTIR + Raman has been applied to study atmospheric aerosol particles to identify inorganic and organic modes in individual sub- and supermicrometer

particles.[78] This powerful technique will provide insights into complex liquid particles, especially at single particle levels.

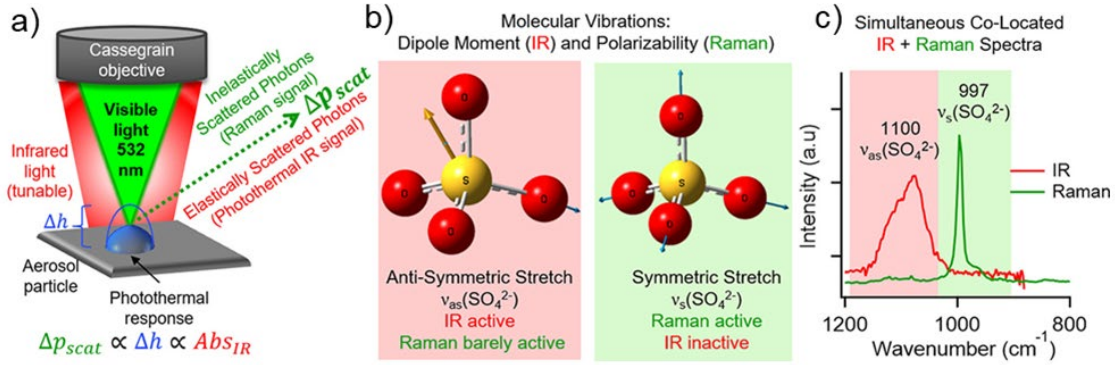

Figure 1.6 a) Schematic of optical photothermal infrared spectroscopy (O-PTIR) and Ramanspectroscopy.Infrared and visible light are focused on the sample through a Cassegrain objective, inducing a photothermal expansion of the particle. Light scattered from the sample (Δp_{scat}) is proportional to the photothermal expansion of the particle (Δh) and absorbance of IR light (Abs_{IR}). Simultaneous IR and Raman spectra are obtained from a single point. b) Molecular vibrations are shown corresponding to antisymmetric (red) and symmetric (green) stretching modes of sulfate. c) IR and Raman spectra obtained from a sulfate-containing particle. Adapted from Olson et al.[78]

1.4 Research Objectives and Scope of Dissertation

In this dissertation, novel acidity and viscosity measurements of individual submicron aerosol particles have been developed, and detailed physicochemical properties of atmospherically relevant aerosol particles have been studied using single-particle microscopy and spectroscopy methods to improve our understanding of atmospheric aerosol formation. Chapter 2 explores a novel single-particle acidity measurement using the degradation of a pH-sensitive polymer. Chapter 3 investigates the morphology and viscosity changes of submicron SOA formed from different VOCs precursors after reactive uptake of isoprene epoxydiols (IEPOX). Chapter 4 investigates morphology, phase state, and chemical composition of individual inorganic sulfate particles with different initial acidities after IEPOX reactive uptake, which highlights that aerosol acidity is critical for multiphase chemical reactions and SOA formation. Chapter 5 describes the application of thermal analysis to measure glass transition temperature of atmospheric particles for the first time. Finally, Chapter 6 discusses the conclusion of all the studies included in this dissertation and future directions for on-going projects. The results herein presented provide insights into physicochemical properties of atmospheric aerosol and their climate-relevant

properties. The novel methods allow us to provide detailed characterization of individual submicron atmospheric aerosols that can lead to improved prediction of SOA on climate and health impacts.

Chapter 2. Aerosol Acidity Sensing via Polymer Degradation

Adapted with permission from Ziying Lei, Samuel E. Bliesner, Claire N. Mattson, Madeline E. Cooke, Nicole E. Olson, Kaseba Chibwe, Julie N. L. Albert, and Andrew P. Ault: Aerosol Acidity Sensing via Polymer Degradation, *Anal. Chem. 2020, 92, 9, 6502–6511*, 2020.
https://doi.org/10.1021/acs.analchem.9b05766

2.1 Introduction

Air pollution episodes with high concentrations of particulate matter (PM) are increasing across many urban areas globally, each with complex emissions and atmospheric chemistry leading to secondary aerosol formation.[109,110] Air pollution leads to an estimated 10% of global deaths annually,[111] primarily from particles that have lifetimes of days-to-weeks in the atmosphere,[73,112,113] particularly submicron particles.[114] Atmospheric particles have complex chemical and physical properties, leading to the formation of reactive oxygen species, oxidative stress, and ultimately respiratory and cardiovascular disease.[115-117] An important factor in the amount of PM formation during pollution events is aerosol acidity, which plays a critical role in determining the different reaction pathways that can dominate secondary aerosol formation.[118,119] During severe air pollution events in Beijing, China, the formation pathways for sulfate and nitrate are pH dependent, as is the multiphase chemistry leading to secondary organic aerosol (SOA) formation in regions where different volatile organic compounds (VOCs) oxidize to form high concentrations of PM.[120] Atmospheric chamber experiments have observed that particles that have lower pH lead to greater SOA formation in comparison to particles at neutral pH.[121,122] As an example, acid-catalyzed ring opening reactions of epoxides that are taken up into particles have lifetimes of less than a minute in acidic particles, but can last for days in particles at neutral pH.[24,121-126] pH-dependent processes also impact particle water uptake,[127,128] liquid-liquid phase separation,[129,130] and gas-particle partitioning.[110] However, there remains considerable uncertainty regarding the actual pH of atmospheric aerosol and its variation as a function of aerosol size,

composition, and time.[110,131] This key uncertainty limits predictions of atmospheric particle concentrations, composition, and, ultimately, health and climate impacts.

Despite the implications of atmospheric particle acidity for health and climate, scientific understanding is still limited due to the lack of methods available to measure individual atmospheric particle pH, with most methods relying on indirect and proxy approaches or thermodynamic modeling assuming equilibrium conditions.[132,133] The challenge of measuring pH is due to the fact that the activity of the H^+ ion ($a_{H^+} = \gamma_{H^+} \times [H^+]$) is not conserved as water content changes (the activity coefficient (γ) typically decreases below 1 when water content decreases). Thus, if particle samples are collected on and extracted from a filter, analyzed under vacuum, or dried during or after collection, the pH of a single particle will no longer be representative of the particle's pH in the atmosphere. Indirect pH measurement methods have used multiple approaches, such as taking the ion balance of common cations and anions and assuming the difference is the H^+ ion,[131,134-136] but indirect and proxy methods have considerable issues and limitations, as explored in detail by Hennigan et al.[132] Other methods for estimating aerosol acidity have used thermodynamic models and phase partitioning approaches that take bulk concentrations of aerosol species combined with gas concentrations (when available) to predict water content and then pH.[137-139] However, low water content, high ionic strengths (> 10 M), incorporation of inorganic ions (*e.g.*, sulfate) into organic species (*e.g.*, organosulfates),[140] and formation of viscous organic phases leading to kinetic limitations can make thermodynamic equilibrium calculations challenging. Additionally, the expense and challenge of making simultaneous measurement of $NH_{3\,(g)}$ and $NH_{4\,(aq)}$, as well as the limitations of assuming thermodynamic equilibrium, inhibits the broad application of phase-partitioning for evaluation and prediction of atmospheric aerosol acidity.[137,141-144] Given that acidity measurement methods for individual ambient particles are lacking, new analytical methods are needed to determine pH.

Recently, a method for the direct pH measurement of individual laboratory-generated aerosols was developed utilizing an acid-conjugate base approach with Raman microspectroscopy.[34] This acid-conjugate base method relates the concentrations from the vibrational modes of an acid and its conjugate base to a calibration curve, which are combined with activity coefficient (γ) calculations and used to determine the activity of the H^+ ion and, thus, pH of individual particles. However, this method has been limited to particles with diameters > 2.5 μm and simple systems with only a few components, due to the use of optical microscopy

methods that are diffraction-limited (e.g. Raman microspectroscopy with a 532 nm laser).[74,145] This is limiting as most pH-sensitive PM formation occurs in fine particles (< 2.5 μm), which have complex chemical compositions, often containing thousands of species in a single particle.[146] Another direct, near real-time aerosol pH measurement has been developed using a colorimetric approach involving a pH indicator and cell phone camera. This method has been applied to measure submicron ambient particles (< 0.4 μm), but is a bulk measurement approach. In addition, it requires samples to have a particulate mass of 65 μg for fine particles (< 2.5 μm) with sufficient aerosol liquid water content for changes in the pH indicator color and a lack of chromophores in the aerosol (e.g. soot) that interfere.[147] Therefore, novel techniques are still needed to measure submicron individual particles, particularly given the range and constantly evolving chemical composition of submicron atmospheric particles, which have important impacts on climate and health.[148-150]

Poly(ε-caprolactone) (PCL) is a hydrolytically degradable, aliphatic polyester that has exhibited utility for applications requiring a degradable material.[151-154] PCL degrades with differing kinetics between pH 1 and pH 3,[155] within the expected pH range of 0-3 for most atmospheric aerosols.[110,156] Herein, we describe how the acid-initiated degradation of PCL films can be harnessed to measure the effective acidity of individual aerosol particles. By irreversibly degrading the polymer, this method provides information related to the pH of individual submicron particles, without requiring challenging coupled gas and particle composition measurements. PCL degradation by highly acidic (pH = 0) aerosol particles was investigated and compared to (lack of) degradation by mildly acidic (pH = 6) aerosol particles using a combination of atomic force microscopy (AFM) to monitor film thickness and Raman microspectroscopy to monitor chemical changes to the polymer. The degradation due to exposure to pH = 0 particles as a function of time and particle size was quantified using model systems containing components of atmospheric aerosols. This novel method provides an approach for studying the pH of individual submicron particles and proof-of-concept for future sensor development.

2.2 Methods

2.2.1 PCL Thin Film Preparation

PCL brush-coated substrates were prepared by coating ultraviolet ozone (UVO) cleaned silicon substrates with a thick (~10^3 nm) PCL film (hydroxyl-terminated, M_n = 45 kDa; Sigma-

Aldrich). After coating with the thick films, substrates were placed on a hotplate at 140 ºC overnight to allow the hydroxyl-terminated PCL polymer to graft to the native oxide layer of the silicon substrate. Thereafter, films were isothermally recrystallized at 25 ºC for 30 minutes. Then, the PCL thick films were rinsed off of the substrate with toluene, leaving behind a residual PCL brush film (~10^0 nm). Applying PCL brushes to silicon substrates inhibits dewetting of films cast onto these substrates.[157-159]

All thin films in this study were cast via flow-coating from a solution of PCL in toluene onto substrates prepared as described above. Following casting, the PCL films were melted at 100 ºC for 10 minutes and then isothermally recrystallized at 25 ºC for 30 minutes. Film thicknesses of approximately 21-25 nm, 50 nm, and 400 nm were measured via spectral reflectance (Filmetrics F20-UV).

2.2.2 Aerosol Generation and Impaction

For aerosol generation, standard solutions were prepared using sulfuric acid (H_2SO_4) (Sigma-Aldrich), ammonium sulfate $(NH_4)_2SO_4$ (Alfa Aesar), and 18.2 MΩ Milli-Q water. All chemicals were > 98.0% purity and used without further purification. A solution of 30 mM $(NH_4)_2SO_4$ with pH = 6 was used as a control in comparison to a 1 M H_2SO_4 solution with pH = 0 that is mostly $HSO_4^-{}_{(aq)}$; the pH value of 0 was chosen based on prevalent pH values for atmospheric particles.[133,137,143,160] All solution pH values were measured by a pH probe (AP110, Accumet Portable). Aerosols were generated from each solution using a Collison nebulizer (*i.e.*, atomizer) operated with HEPA filtered air, and inertially impacted on PCL thin films using a mini-multi orifice uniform deposit impactor (mini-MOUDI) (MOUDI model 135, MSP Corporation). The mini-MOUDI consists of 8 stages with different aerodynamic diameter (d_a) 50% size cuts, and the particles were impacted on stages 6, 7 and 8 with aerodynamic cut points leading to size ranges of < 180 nm, 180-320 nm, and 320-560 nm, respectively. Submicron particles were the focus of this study, as particles < 1 μm corresponds to the size regime where key pH-dependent sulfate, nitrate, and SOA formation reactions occur.[110,114] Aerosol particles were generated under humid conditions, ~90% relative humidity (RH), to ensure they were aqueous and capable of degrading the PCL thin films. Aerosol particle pH was confirmed using the colorimetric pH method detailed by Craig et al.[145] Particle impaction leads to spreading, which is substrate dependent.[73] Prior work has shown on silicon wafers that spreading ratios of ~2.5:1 to 6:1 are common for atmospheric and

lab-generated particles.[19,150,161] The role of phase in spreading and 3-dimensional morphology have also been shown.[19,162] In this study, the focus is on aqueous particles and spreading ratios on the polymer are similar to those of aqueous particles on bare silicon.

Following impaction of aqueous aerosol particles onto the PCL films, samples were promptly placed in a sealed humidity-controlled chamber at 50% RH to maintain the liquid state of aerosol particles. Since the particles are generated as aqueous droplets, to maintain the particles in an aqueous/liquid state they must be kept above the efflorescence RH (40%) to avoid undergoing a phase transition to an amorphous solid or crystal at 23 °C, the temperature of the laboratory.[163-166] To confirm that the particles were stable in their aqueous state and not undergoing reactions, beyond those with the polymer, two peaks were monitored with Raman microspectroscopy (instrumental details below): 1) the sulfate and bisulfate symmetric stretches (for pH = 6 and pH = 0, respectively) and 2) the ν(O-H) stretching region, which is associated with water in the particles.[167] For the sulfate/bisulfate stretch, the continued observation of $\nu_s(SO_4^{2-})$ at 980 cm^{-1} and $\nu_s(HSO_4^-)$ at 1040 cm^{-1} throughout storage combined with a lack of a peak associated with organosulfates $\nu(ROSO_3^-)$ at ~1065 cm^{-1} confirms the stability of the particle composition.[168] For the water vibration, the ν(O-H) mode in the Raman spectra (3350-3600 cm^{-1}) of the sulfuric acid particles was monitored at different RHs to confirm that the particles remain liquid during storage (Figure A.1), as shown for previous single aerosol particle Raman studies.[167] Following degradation, samples with aqueous particles still on the polymer-coated silicon substrate were rinsed with Milli-Q water to remove the soluble particles on the surface leaving only polymer and silicon behind. All PCL samples were dried before further characterization.

2.2.3 Microscopic and Spectroscopic Characterization

The size and depth of the depressions left in the polymer film from PCL degradation were characterized by atomic force microscopy (AFM). AFM imaging was carried out using a PicoPlus 5500 AFM (Agilent) (NanoScience; resonance frequency 300 kHz, force constant 40 N/m). AFM images for PCL samples were collected in tapping mode across regions ranging from 4 μm by 4 μm to 25 μm by 25 μm. A nanoIR2 system (Anasys Instruments, Santa Barbara, CA) was used to chemically characterize the PCL with photothermal infrared spectroscopy (PTIR). AFM height and deflection images and IR spectra of PCL before and after degradation were collected in contact mode (IR power 16.54%, filter in) at a scan rate of 0.75 Hz using a gold-coated contact mode

silicon nitride probe (Anasys Instruments, 13 ± 4 kHz resonant frequency, 0.07-0.4 N/m spring constant). IR spectra were collected over a frequency range of 900-3600 cm^{-1} using a tunable IR source (2.5-12 μm, 1 kHz) with a resolution of 4 cm^{-1}/point.

Raman microspectroscopy was used to characterize PCL chemical composition before and after its degradation at the same location. Raman spectra were collected using a LabRAM HR Evolution Raman microspectrometer (Horiba, Ltd.) consisting of confocal optical microscopy (100 × 0.9 N.A. Olympus objective), a Nd:YAG laser source (50 mW, 532 nm), and CCD detector. All spectra from 500 to 4000 cm^{-1} were acquired for 60 s with three accumulations at a spectral resolution of 1.8 cm^{-1} using a 600 groove/mm grating. Initial calibration for the instrument involved nine different frequencies, including the laser line (0 cm^{-1} Raman shift), the Si wafer at 520 cm^{-1}, a calibration standard with a 1004 cm^{-1} peak, and a diamond band at 1332 cm^{-1}. The instrument was checked in the laboratory for variation from the initial calibration using the laser line and the Si wafer peak at 520 cm^{-1}. Variation in frequencies were < 1% due to thermal drift or other minor effects. The peak at 520 cm^{-1} was checked daily for shifts beyond a pixel on the detector (1.8 cm^{-1} for the 600 groove/mm grating used in this study), which if observed would have required further calibration; however this did not occur over the time period of the study as calibrations of this instrument have been stable for multiple years.[74,84,169]

2.3 Results and Discussion

As illustrated schematically in Figure 1a, for this study, a PCL film is fabricated, has aerosol impacted on it, is allowed to react and degrade, and is imaged with an AFM after the particles and most degradation byproducts are washed off. The pronounced holes in the polymer film in Figure 2.1b (right image) demonstrate the ability of the acidic particles to degrade the polymer. The degradation mechanism for the acid-catalyzed degradation of the PCL film is shown in Figure 2.1c. The H^+ ion from the acid solution protonates the carbonyl group leading to an addition-elimination reaction and breaking of the polymer carbon-carbon backbone. The hydrolysis reaction that occurs leads to the formation of 6-hydroxyhexanoic acid and other degradation byproducts (oligomers).[153,155]

The initial morphology of a non-degraded PCL thin film (21 ± 3 nm) is shown in Figure 2.2a, as well as a height trace from the image in Figure 2.2d. Aerosol particles were generated

from pH = 6 and pH = 0 solutions and the particles with d_a 320-560 nm were impacted onto the PCL thin films. After 15 days, the particles on the PCL were rinsed off and the AFM images were collected that are shown in Figure 2.2b and 2.2c, respectively. Scanning electron microscopy (SEM) images corroborated the morphology observed by the AFM and further information is

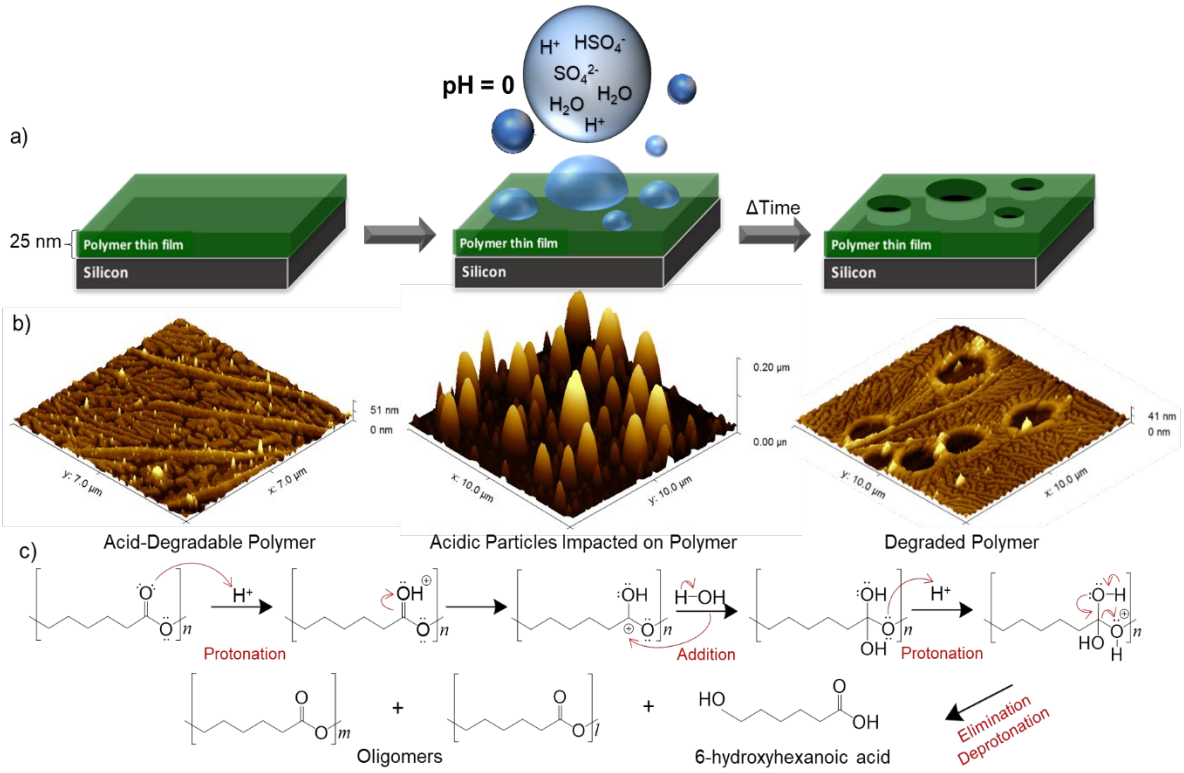

Figure 2.1 a) Schematic depicting the use of PCL thin film degradation for determining aerosol acidity; b) AFM 3D height image of PCL degradation process, the size (length × width × height) of AFM images from left to right are: 7 µm × 7 µm × 51 nm, 10 µm × 10 µm × 0.2 µm, 10 µm × 10 µm × 41 nm; c) and acid-catalyzed degradation mechanism of PCL, based on Woodruff et al, 2010.[55] Note that "*n*" refers to the number of repeat units in the starting PCL material and that $l + m < n$.

provided in the supporting information (Figure A.2)

Based on visual inspection of the height trace, there is consistent variation in the height of the PCL material due to its semi-crystalline structure prior to aerosol impaction. The surface roughness of the initial PCL was characterized and a 2 nm root mean squared (RMS) roughness for the surface was calculated using Gwyddion and Nanoscope software (details in the Supporting Information); the spreading ratios of particles on these surfaces are similar to those reported for particles impacted on silicon wafers,[19,150,161] suggesting that this low level of surface roughness does not affect particle deposition or surface wetting. Near neutral particles impacted on the films

did not appear to degrade the polymer and did not lead to particle-sized holes in the PCL thin films (Figures 2.2b and 2.2e). For the near-neutral particle sample, qualitative comparison of the height traces of the initial film and post-rinse film show similar profiles (Figures 2.2d and 2.2e). This result shows that particles with near neutral pH did not cause PCL degradation. In contrast, the acidic aerosol particles degraded the PCL, generating holes corresponding to individual particles (Figures 2.2c and 2.2f). The larger AFM height images of non-degraded PCL, the PCL after exposed to near-neutral particles, and a degraded PCL from numerous particles are shown in the Supporting Information to show the representativeness of the example regions in Figure 2.2 (Figure A.3). It should be noted that the size of the hole (~2-3 μm) is larger than the d_a of the suspended particles (320-560 nm) due to the aqueous aerosol particles spreading on the PCL film upon impaction and the extent of spreading agrees with prior studies.[19,73,170] Comparing the height trace of the initial PCL and the height trace of the degraded PCL indicates that the acidic aerosol particles degraded the full depth of the PCL thin film and reached the silicon substrate after 15

days. The height trace shows the edge of the hole is taller than the average height of the surface of the film. We believe this is due to accumulation of insoluble degradation byproducts of the PCL material at the edge of the hole, whereas soluble degradation products are removed when the particles are was washed off with water. The results from AFM illustrate the potential for aerosol particle acidity measurement through physical changes to the substrate.

To expand beyond physical characterization, the changes to the PCL films were chemically characterized using Raman microspectroscopy prior to, during, and after the degradation process. Due to the limits of detection for the Raman microspectrometer, a thicker PCL film (50 nm) was used. Again, pH = 0 acidic aerosol particles were deposited for 15 days, but with a greater loading of particles, which coalesced into larger droplets, as seen in in Figure 2.3b. Since the Raman focused on chemical changes, not physical, the coalescence was not an issue and coalesced

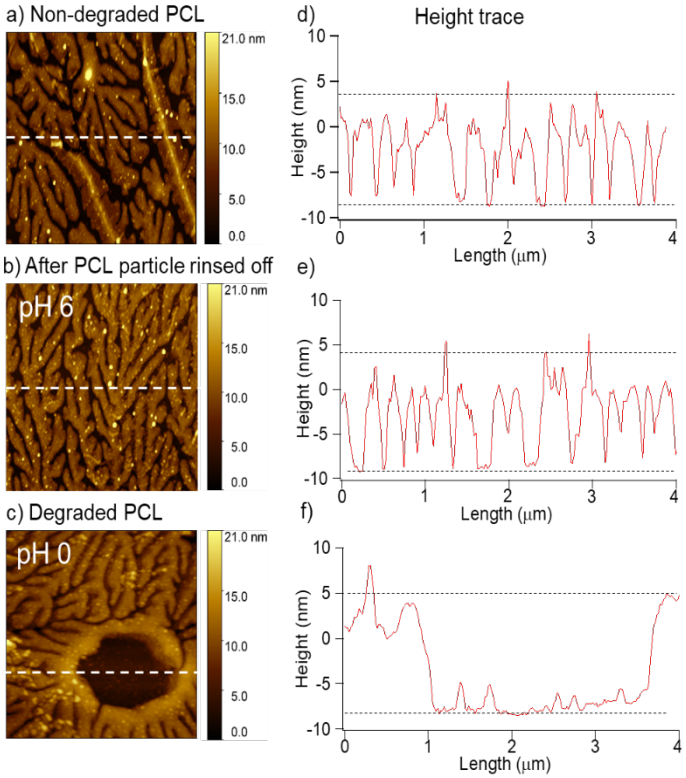

Figure 2.2 4 × 4 μm AFM height images of PCL films: a) non-degraded; b) following exposure to ammonium sulfate pH 6 particles for 15 days; c) following exposure to sulfuric acid pH 0 particles for 15 days. The dark brown color represents the silicon substrate, and the golden color represents the PCL. d), e), and f) height traces corresponding to the white dash lines on the AFM height images. Black dash lines represent approximate PCL film thickness and 0 on the y-axis represents average PCL height. The bright spots on the AFM images are tip artifacts.

particles are only shown in Figure 2.3. The PCL film was analyzed at three different periods: non-degraded PCL, before rinsing off the acidic particles that had merged into droplets, and after rinsing off the merged particles.

The Raman spectrum of the non-degraded PCL shows modes in the ν(C-H) stretching region at 2871 cm^{-1} and 2916 cm^{-1}, which correspond to asymmetric elongation of methylene-oxygen vibrations ν(CH_2-O) and symmetric elongation of methylene groups ν(CH_2-). The carbonyl group ν(C=O) mode was observed at 1723 cm^{-1}, corresponding to the aliphatic ester ν(CO_2-) of the PCL.[168,171] A peak at 1441 cm^{-1} was also observed that corresponds to the asymmetric elongation of the carbon-hydrogen δ(C-H) of the methylene (CH_2) . After the pH 0 acidic aerosol particles were impacted and sat on the PCL for 15 days, the Raman spectra were collected before and after rinsing off the particles. When compared with the non-degraded PCL, three main differences were observed between the spectra collected after 15 days, but before particles were washed off. First, the carbonyl group ν(C=O) mode at 1723 cm^{-1} decreased, suggesting that, as expected, the carbonyl group of the PCL is a participant in the acid-driven reaction and is favorable for nucleophilic attack when exposed to acid during the PCL degradation process. Secondly, a weak peak was observed at 3460 cm^{-1} from either the hydroxyl of the carboxylic acid ν(O-H) that forms during the hydrolysis reaction or water from the sulfate-containing particles that were impacted. Lastly, strong peaks were observed from 2870 cm^{-1} to 3038 cm^{-1}, which corresponds to C-H stretches of the methylene groups. A shoulder corresponding to the symmetric vibration of the carboxylate $\nu_s(COO^-)$ functional group at 1416 cm^{-1} was also observed, which suggests the formation of carboxylic acid functional groups as the ester degrades (e.g. 6-hexanoic acid, as shown in mechanism in Figure 2.1c). These results are consistent with the degradation of polyesters, which have very similar structures to PCL. Raman spectra were also collected after rinsing off the acidic particles and PCL degradation products. A comparison of the degraded, rinsed PCL, and non-degraded PCL Raman spectra supports that the carbonyl group fully reacted with the acid, observed by the characteristic peaks of asymmetric elongation of methylene-oxygen ν(CH_2–O) and symmetric elongation of methylene group δ(CH_2–) at 2871 cm^{-1} and 2916 cm^{-1} respectively.[80,171] A strong sulfate peak ν(SO_4^{2-}) at 978 cm^{-1} was also observed before wash off of the sulfuric acid particles, which confirmed the chemical composition of particle, and the peak is no longer present after washing off the substrate with water, which illustrates that the particles

were rinsed off (Figure A.4). To obtain more detailed Raman and IR spectra for mode assignments, spectra were collected of non-degraded PCL using 400 nm thick PCL (Figure A.5 and A.6).

To investigate the PCL degradation rate, acidic aerosol particles with pH = 0 were generated and impacted on 22 ± 3 nm thick PCL films. Particles were rinsed off at different time intervals ranging from 0 days to 15 days. In Figure 2.4a, the yellow, spherical shapes are acidic particles with d_a 180-320 nm and heights of ~50 nm. The AFM images of non-degraded PCL were collected (Figure 2.4b) as comparison at 0 days. After degradation for 3 days, the acidic aerosol particles were rinsed off from PCL and shallow spherical holes (light brown) were observed (Figure 2.4c), denoting degradation of the polymer film by the acidic aerosol particles. An average of 42 individual particles were examined and used to calculate the PCL degradation thickness (the numbers of particles for each sample are listed in the Figure 2.4 caption and Table A.1). Some

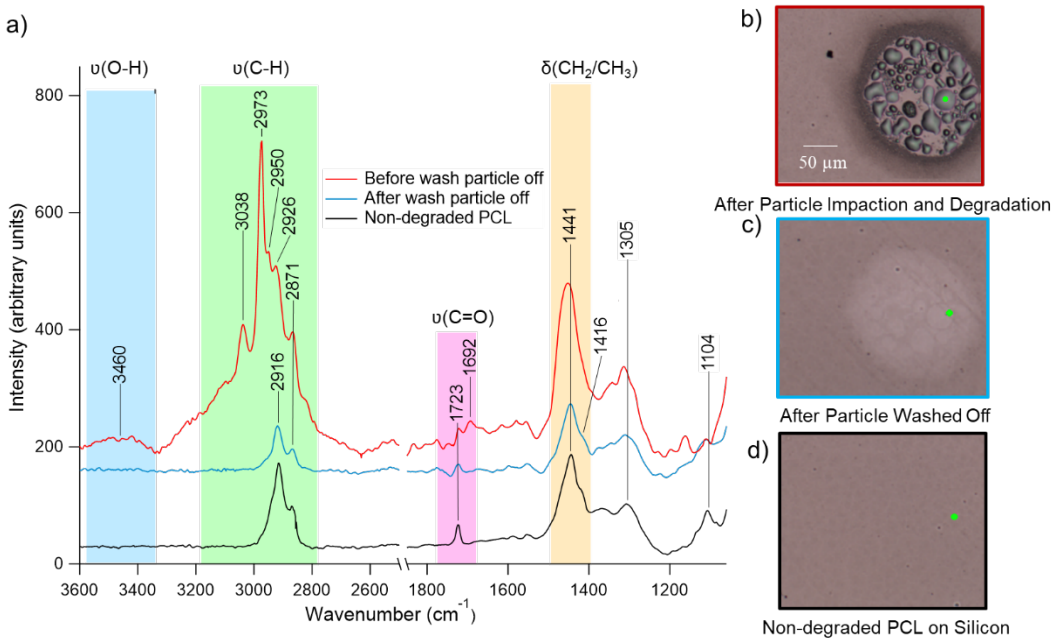

Figure 2.3 a) Raman spectra of nondegraded PCL film background (black), PCL film with pH 0 acidic particles for 15 days (red), and PCL film after all particles were rinsed off (blue); b) a microscopic image after particle impaction and merging into larger droplets; c) microscopic image after particles were washed off; and d) microscopic image of nondegraded PCL. The green dots in the microscopic images correspond to the locations where spectra were collected. Spectra of the $\nu_s(SO_4^{2-})$ at 978 cm^{-1} are shown in the Appendices due to strong interference from the silicon wafer phonon mode in the same spectral window.

irregularly shaped and larger holes were observed after 3 days, likely due to some of the aqueous acidic particles merging for this specific sample. Although the PCL started reacting with H^+ within

3 days, the degradation reaction was only occurring near the PCL surface, and the structure of the initial PCL was still visible underneath the holes (Figure 2.4c). For the films that degraded for 7 days, distinct, clear holes that go through most of the film were observed after the acidic particles were washed off and the characteristic morphology of the initial PCL film became less apparent (Figure 2.4d). After 15 days, the PCL was completely degraded away down to the silicon substrate underneath the area of the acidic aerosol particles (Figure 2.4e). It should be noted that there may be some degradation horizontally, in addition to vertically, leading to holes slightly larger than the projected area of the impacted particle. The thickness of degraded PCL material was measured by subtracting the thickness of the holes from the initial PCL thickness measured by spectral reflectance to show the extent of PCL degradation (Figure 2.4f). The trend of increasing

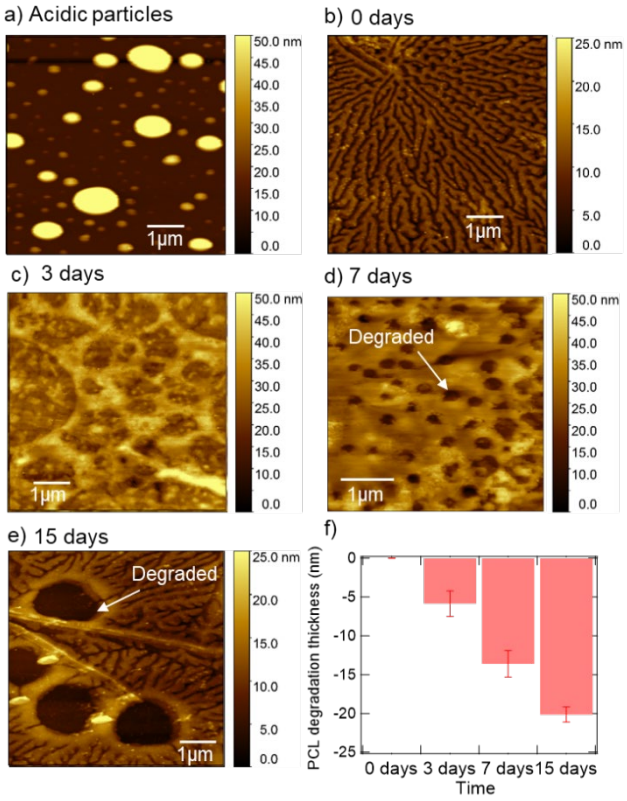

Figure 2.4 pH 0 aerosol particles with da 180–320 nm were impacted on PCL samples, and the particles were rinsed off after different periods of time. a) Shows particles impacted on the polymer. AFM images were collected after b) 0 days (nondegraded PCL); c) 3 days (46 particles); d) 7 days (41 particles); and e) 15 days (40 particles). f) Plot of PCL degradation thickness changes over time. The error bars represent standard deviation of PCL degradation for each time period, and it is measured by 20 height traces across the AFM height image.

degradation with time is attributed to greater reaction of H^+ with PCL to break the polymer chain and removal of degradation products when rinsed.

Recent results have suggested the aerosol acidity may increase at smaller particle sizes, but this is not well understood.[145] To further understand the PCL degradation as a function of particle size, PCL films had acidic particles of varying diameters impacted on them. The acidity of aerosols with different sizes was confirmed using a distinct colorimetric pH method.[145] For pH = 0 particles with d_a of < 180 nm, 180-320 nm, and 320-560 nm bulk pH values of 0.00 ± 0.09, 0.00 ± 0.08, and 0.18 ± 0.04 respectively were observed colorimetrically (Figure A.7). It should be noted that

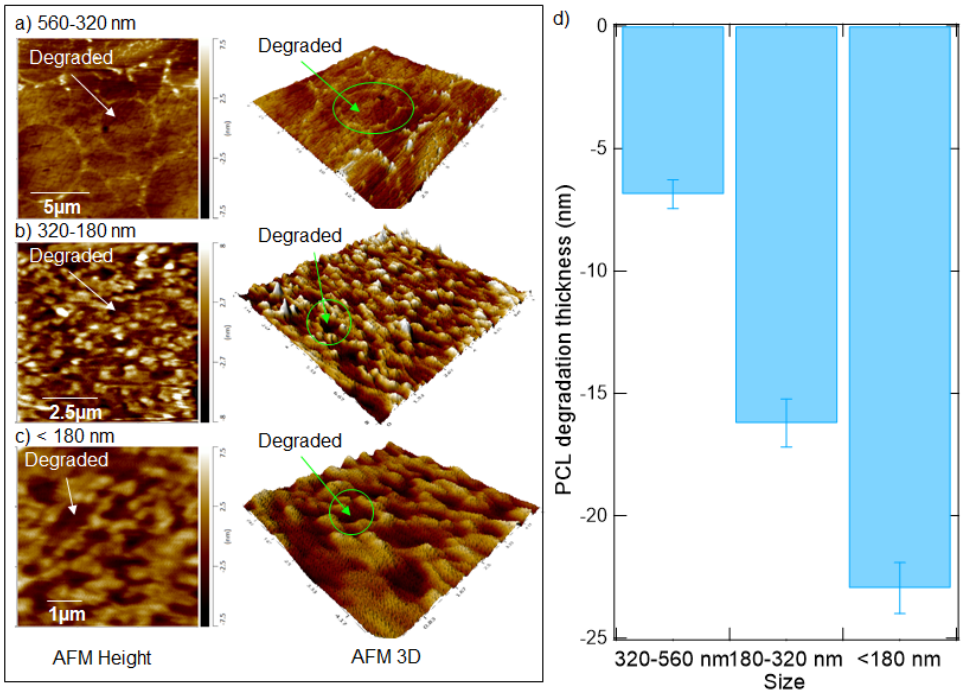

Figure 2.5 Left side: AFM height and 3D images of pH 0 acidic particles with different sizes impacted on PCL and rinsed off after 10 days (the numbers of individual particles were specified). a) d_a 320-560 nm (27 particles); b) d_a 180-320 nm (34 particles); c) d_a < 180 nm (29 particles). d) Plot of PCL degradation thickness as a function of acidic particle sizes. The error bars represent the standard deviation of the degradation, which is measured by 20 height traces per image across the hole in the AFM height image. An average 30 individual particles were examined.

the minimum pH value on the pH indicator paper is 0, and thus the particles < 320 nm are likely to be more acidic than large particles from pH = 0 due to lower water content in the small particles. Due to the range of the pH indicator paper, the aerosol particles with d_a < 180 nm, 180-320 nm, and 320-560 nm came from the same pH = 0 solution were collected simultaneously on PCL, respectively. Both AFM height and 3D height images show the spherical morphology for the PCL

degradation caused by the individual acidic particles (Figure 2.5). An average of 30 particles were examined and used to calculate PCL degradation thickness and the detailed number of particles for each sample were listed in the caption and Table A.1.

Smaller particle size corresponded to greater PCL degradation (Figure 2.5). For the pH 0 acidic solution, particles with d_a of < 180 nm, 180-320 nm, and 320-560 nm had median PCL degradation thickness of 23 ± 1 nm, 16 ± 1 nm, and 6.9 ± 0.6 nm, respectively. The increasing PCL degradation thickness for the smaller particles (< 180 nm) indicates smaller particles were likely more acidic than the larger particles (320-560 nm). With lower water content at smaller sizes, the molar concentration of chemical species and ionic strength increase, particularly $[H^+]$ increases, resulting in increased acidity for the smaller particles. This result is consistent with Craig et al. who identified increased acidity with smaller particle sizes for similar solutions,[44] but could not probe particles as small as probed in Figure 2.5. Overall, the result from this study and previous studies demonstrate that the acidity of particle varies by particle size, a result implying non-thermodynamic equilibrium conditions.

2.4 Conclusions

This study presents a novel method for measuring the acidity of submicron aerosol particles through polymer thin film degradation. Acidic aerosol particles with aerodynamic size cuts of < 180 nm, 180-320 nm, and 320-560 nm were generated and collected on PCL thin films, enabling the observation of different PCL degradation thickness based on particle size. Comparing this method with other established spectroscopic and colorimetric measurements of aerosol pH demonstrates its potential for determining whether individual particles are acidic without some of the limitations of Raman microspectroscopy and bulk colorimetric methods (ensemble average). The results presented herein focused on a difference in pH (ΔpH) that represents the highest and lowest pH values typical of the atmosphere (pH = 0 to pH = 6) as a proof of concept, but as a result, our findings are more qualitative and more work is needed with respect to connecting to discrete pH values and determining the precision with which ΔpH can be determined. Due to the complex nature of aerosol particles with respect to chemical composition and atmospheric conditions, there are many factors that influence aerosol acidity that need to be considered in future work, such as inorganic-organic mixtures. The effect of RH and water content need to be tested and explored to improve current understanding of how and why pH decreases with particle size,

particularly given the interplay between pH and viscosity with respect to multiphase chemistry.[140,172] To establish a complete pH measurement system based on polymer degradation rate and thickness, different polymers and detection methods will need to be investigated to determine figures of merit including range, sensitivity, and precision. We estimate that ΔpH will be roughly 1 pH unit for this system, but further testing and the use of more acid-sensitive polymers or co-polymers will be needed to experimentally determine sensitivity. Future aerosol acidity studies can utilize this single particle size-resolved pH measurement to study acidity of ambient aerosols, especially SOA formation and inorganic aerosol (e.g. sulfate and nitrate in Beijing haze conditions) that are strongly dependent on acidity. Acidity is a fundamental chemical property of aqueous aerosols and the polymer-based sensing approach developed in this study has the potential to advance our understanding of pH-dependent multiphase chemical processes, which in turn can improve the atmospheric models focused on relating aerosol particle properties to health and impacts.

2.5 Acknowledgements

This work was supported by Gulf Research Program of the National Academies of Sciences, Engineering, and Medicine (Grant No. 2000005803 (Tulane University) and Grant No. 2000007270 (University of Michigan)), National Science Foundation (NSF) grants CAREER award CHE-1654149 to Prof. Ault and NSF DMR-1460637 to Tulane University for the Research Experience for Undergrads (REU) program that supported Ms. Kaseba Chibwe's work in Prof. Albert's laboratory. Professor Kerri Pratt is acknowledged for helpful discussions. Dr. Yue Zhang is acknowledged for technical assistance. Atomic force microscopy was performed at the Scanning Probe Microscopy facility in the Department of Chemistry at the University of Michigan. Michigan Center for Materials Characterization is acknowledged for assistance with the SEM instruments.

Chapter 3. Morphology and Viscosity Changes after Reactive Uptake of Isoprene Epoxydiols in Submicrometer Phase Separated Particles with Secondary Organic Aerosol Formed from Different Volatile Organic Compounds

Ziying Lei, Nicole E. Olson, Yue Zhang, Yuzhi Chen, Andrew T. Lambe, Jing Zhang, Natalie J. White, Joanna M. Atkin, Mark M. Banaszak Holl, Zhenfa Zhang, Avram Gold, Jason D. Surratt, Andrew P. Ault: Morphology and Viscosity Changes after Reactive Uptake of Isoprene Epoxydiols in Submicrometer Phase Separated Particles with Secondary Organic Aerosol Formed from Different Volatile Organic, *ACS Earth & Space. 2021 (Under Review)*

3.1 Introduction

Secondary organic aerosol (SOA) constitutes a significant fraction of the global aerosol budget,[55] particularly for fine particulate matter ($PM_{2.5}$, aerosol particles with aerodynamic diameters < 2.5 μm), which is the most important size range with respect to aerosol impacts on human health and climate.[7-9] SOA is primarily formed from oxidation of volatile organic compounds (VOCs), resulting in lower-vapor pressure products that either nucleate, condense or undergo reactive uptake to existing particles (e.g., ammonium-sulfate particles).[173] Since SOA is formed from a variety of biogenical and anthropogenic VOC precursors (α-pinene, β-caryophyllene, isoprene, and toluene), this leads to SOA being composed of a wide range of chemical species with different physicochemical properties (e.g., viscosity and morphology).

Viscous SOA can increase diffusion time scales from microseconds to weeks (i.e., longer than atmospheric particle lifetimes),[59] which decreases the rate of SOA formation. For example, the reactive uptake of isoprene epoxydiols (IEPOX), a key oxidation product of isoprene,[27,174,175] can decrease diffusion by over an order of magnitude for viscous SOA formed on atmospherically-relevant timescales (< 2 days).[21,25,38] Koop et al. established a framework for understanding the viscosity of bulk organic material, which ranges from the dynamic viscosity (η) of liquid ($\eta < 10^2$ Pa s) to semi-solid ($10^2 \leq \eta \leq 10^{12}$ Pa s) or glassy/amorphous solid ($\eta > 10^{12}$ Pa s).[58,60,63,64,96,176,177] Renbaum-Wolff et al. probed viscosity as a function of relative humidity (RH) using a "bead-

mobility" technique and a "poke-flow" technique for SOA derived from α-pinene,[178] isoprene,[65] and toluene,[66] which confirmed in ~100 micron particles that SOA has a wide range of viscosities. Organosulfates,[179-181] which are a key component of atmospheric SOA, have been shown to increase particle viscosity after incorporation of inorganic sulfate ions into organic species.[19,38] Modeling used to study SOA viscosities has continued to improve, leading to better predictions of viscosity for multicomponent mixtures and surrogate SOA mixtures derived from the oxidation of different VOC precursors.[62,182,183] Shiraiwa et al. have related molecular weight to glass transition temperature (T_g) and viscosity according to the number of different C, H, and O atoms and C-H and C-O bonds in a molecular formula or the molecular weight (M), oxygen-to-carbon ratio (O:C), and coefficients (A-E) (Equation 1):[184]

$$T_g = A + BM + CM^2 + D(O{:}C) + EM(O{:}C) \qquad \textbf{Eq. 3.1}$$

Despite significant progress in understanding OA viscosity,[21,36,57,64,185-187] understanding the impacts on viscosity within individual submicron particles from different VOC precursors on reactive uptake is still limited.

Morphology is also critical to understand SOA formation, especially as aqueous and organic components can separate into distinct phases due to the low miscibility of many SOA species within high ionic strength aqueous particles.[36,44,46,53] Example morphologies include homogeneous, core-shell, and partially engulfed, which all undergo reactive uptake differently, particularly when the organic phase is viscous.[36,38,41,188] For example, laboratory studies have shown a ~50% decrease in reactive uptake of IEPOX to particles with a coating of viscous SOA from α-pinene ozonolysis ($\eta = 9.3 \times 10^7$ Pa s)[184,187] around acidic sulfate particles (pH = 1.5) versus aqueous (non-coated) acidic sulfate particles only.

Most characterization of the impacts of morphology and viscosity on reactive uptake has focused on loss of gas-phase semi-volatile organic compounds,[39] but it is also critical to understand how viscosity and morphology evolve within particles as they undergo reactive uptake. Recently, Olson et al. showed that the aqueous, sulfate-rich core of accumulation mode particles coated with α-pinene and toluene SOA was largely converted to viscous organosulfates after uptake of IEPOX in a flow tube.[19] Atmospheric chambers enable studies over longer timescales (1 minute vs. hours) and there have been few chamber studies probing the impact of coating viscosity and morphology

on individual particles at atmospherically-relevant sizes (~100 nm).[189] Additionally, few studies have analyzed uptake to mixed organic-inorganic particles, particularly submicron particles with complex morphologies, such as core-shell types. As atmospheric chemistry models continue to improve parameterizations for accurate predictions of SOA formation rates and concentrations,[17,190,191] a detailed understanding of SOA formation at the single particle level is needed to provide improved modeling capabilities.

SOA from α-pinene oxidation has been the most studied coating for core-shell (inorganic-organic) particles with respect to reactive uptake,[19,21,40,42,63] but it is important to understand how SOA coatings formed from oxidation of other VOC precursors impact morphology and viscosity. Herein, we probed the viscosity and morphology of size-selected, submicron, acidic particles coated with SOA formed from oxidation of four different VOC precursors (*α*-pinene, *β*-caryophyllene, isoprene, and toluene), which were subsequently injected into an atmospheric chamber and exposed to IEPOX over the course of two hours. Individual particles were characterized using atomic force microscopy (AFM), AFM with photothermal infrared spectroscopy (AFM-PTIR), Raman microspectroscopy, and scanning electron microscopy with energy dispersive X-ray spectroscopy (SEM-EDX). Significant modification of viscosity and morphology was observed after the reactive uptake of IEPOX, which was highly dependent on the physicochemical properties of the SOA formed from the different VOC precursors examined in this study. The viscosities of *α*-pinene and *β*-caryophyllene SOA decreased significantly after IEPOX uptake, while the viscosities of isoprene and toluene SOA did not appreciably change. Phase separation occurred frequently for larger particles, and complex morphology was present for all four types of SOA particles. Overall, the changes in physicochemical properties and chemical composition of different SOA particle types after IEPOX reactive uptake increase our understanding of the impacts of multiphase chemical reactions on physicochemical properties and can lead to improved predictions of SOA formation.

3.2 Methods

3.2.1 Aerosol Particle Generation and Collection

Aqueous seed particles, prior to coating with SOA, were generated from a solution of 0.06 M ammonium sulfate (Sigma Aldrich, ≥ 99% purity) and 0.06 M sulfuric acid (Sigma Aldrich, ≥ 98% purity) using a constant output atomizer (TSI Inc., Model 3076). This solution has a bulk pH

of 1.5,[33] which was chosen based on a common pH value for submicron atmospheric particles.[32,192] Aerosol-laden air passed through one diffusion drier to remove excess water, but not to a low enough RH (i.e., RH > 40%) that they would effloresce and form solid particles. Particles with an electronic mobility diameter of 100 nm were size selected by a differential mobility analyzer (DMA, TSI Inc., Model 3080) with flow rates resulting in a semi-monodisperse size distribution.[21] They were then coated with SOA formed from OH-initiated oxidation of either toluene or isoprene, or by ozonolysis of either α-pinene or β-caryophyllene using a Potential Aerosol Mass (PAM) reactor (Aerodyne Research, Inc.).[19,21,193] Aerosol size distributions from a scanning electrical mobility spectrometer (SEMS, BMI Inc., Model 2100) were measured to ensure acidified ammonium sulfate seed particles were evenly coated with SOA and that no nucleation mode SOA particles were observed before particles were injected into the University of North Carolina at Chapel Hill (UNC) 10-m^3 indoor chamber facility.[30,194] The PAM outflow and chamber were both equilibrated to 50% RH to represent the daytime RH in the southeastern United States.[133] After SOA-coated inorganic sulfate particles were injected, the chamber was left static for at least 30 minutes to ensure that the aerosol particles were stable and that the chamber was uniformly mixed. Then, *trans*-β-IEPOX, which was synthesized at UNC following a published procedure,[195] was dissolved in ethyl acetate and gaseous IEPOX was generated by using a high-purity nitrogen flow of 2 L min^{-1} for 10 min and then 4 L min^{-1} for 50 min through a heated manifold (60 °C). This approach to introducing gaseous IEPOX into the indoor chamber has been used in previous UNC chamber studies.[19,21,30,38,196] Aerosol size distributions and number concentrations were continuously measured from the chamber to monitor particle growth using a SEMS. Before sampling for microscopy analysis, an additional DMA was used to select 150 nm particles formed from α-pinene, β-caryophyllene, isoprene, and toluene SOA, respectively, prior to IEPOX uptake. Additionally, 150, 200, and 250 nm SOA particles were size selected after IEPOX uptake for each VOC precursor. These sizes were chosen based on the size distributions of these four types of SOA in the chamber (Figure B.1). SOA particles were inertially impacted on silicon wafers (16013, Ted Pella Inc.) and quartz (26016, Ted Pella Inc.) substrates using a microanalysis particle sampler (MPS-3, California Measurements Inc.) at 50% RH, specifically the smallest stage with an aerodynamic diameter (d_a) < 400 nm size cut. A schematic figure showing aerosolization, coating, and UNC chamber experimental setup, along with relevant instrumentation is shown in Figure B.2.

3.2.2 Microscopy and Spectroscopy Analysis

Individual inorganic-SOA mixed particles were analyzed to determine their size, morphology, and chemical composition using AFM, AFM-PTIR, Raman microspectroscopy, and SEM-EDX both before and after IEPOX uptake. Both AFM and Raman were conducted at room temperature (25°C), ambient pressure, and 50% RH, while SEM images and spectra were collected under vacuum (10^{-5} – 10^{-6} Torr).

A PicoPlus 5500 AFM (Agilent, Santa Clara, CA) was used to characterize the morphology of individual inorganic-SOA mixed particles. Imaging was performed in tapping mode using Aspire CT300R probes (NanoScience; resonance frequency 300 kHz, force constant 40 N/m), to obtain height, amplitude, and phase images. The samples were scanned in 10 μm x 10 μm areas with line scans of 0.75 Hz and 512 × 512 pixels resolution. Raw data collected by AFM was processed by SPIP 6.2.6 software (Image Metrology, Hørsholm, Denmark) to measure height, projected area diameter, and volume, which is used to calculate volume equivalent diameter for individual particles. The spreading ratios of individual particles were calculated by using individual particle radius divided by particle height, as described in detail previously.[19,96] T-tests were performed by comparing the spreading ratio of each SOA type before and after IEPOX uptake, and the spreading ratios were considered to be statistically different for p values < 0.05.

A nanoIR2 system (Anasys Instruments, Santa Barbara, CA) was used to characterize the chemical composition of individual submicron SOA particles via photothermal infrared (PTIR) spectroscopy. AFM height, deflection images, and PTIR spectra of particles with SOA formed from toluene, α-pinene, isoprene, and β-caryophyllene after IEPOX uptake were collected in contact mode (IR power 16.54%) at a scan rate of 0.75 Hz using a gold-coated contact mode silicon nitride probe (Anasys Instruments, 13 ± 4 kHz resonant frequency, 0.07-0.4 N/m spring constant). The IR spectra were collected over a frequency range of 900-3600 cm^{-1} using a tunable IR source (2.5-12 μm, 1 kHz repetition rate, optical parametric oscillator, OPO) with a resolution of 4 cm^{-1}/point. A nanoIR3 system (Bruker, Santa Barbara, CA) with a tunable IR source (880-1950 cm^{-1} frequency range, 100 kHz repetition rate, quantum cascade laser, QCL) was used to collect PTIR spectral maps of SOA particles. Tapping-IR mode was used and the amplitude of cantilever oscillation was mapped using 128 co-averages, 400 pixels resolution. The IR ratio map was

generated in Analysis Studio (Anasys Instruments software V3.15) to show differences in the spatial distribution of chemical components based on different vibrational modes.

Raman microspectroscopy was conducted using a Horiba LabRAM HR Evolution Raman Spectrometer (Horiba Scientific) equipped with a 50 mW 532 nm Nd:YAG laser source and CCD detector coupled to a confocal optical microscope (Olympus, 100x objective NA:1.25). A diffraction grating with 600 groove/mm was used to obtain a spectral resolution of 1.7 cm^{-1}. Raman spectra were collected in the range 500-4000 cm^{-1} for 3 accumulations × 15 seconds acquisitions for each particle.

SEM analysis was conducted on a FEI Helios 650 Nanolab Dualbeam electron microscope that operated at an accelerating voltage of 10.0 kV and a current of 0.40 nA. An Everhart-Thornley secondary electron detector was used for imaging. EDX spectra were acquired for 20 seconds using an EDAX Silicon Drift Detector and GENESIS EDX software version 5.10 (EDAX Inc., Mahwah, NJ), as in prior work.[19]

3.3 Results and Discussion

Phase separated particles (organic coating around an aqueous/inorganic core) with SOA coatings from different VOC precursors (α-pinene, β-caryophyllene, isoprene, and toluene) were investigated before and after reactive uptake of IEPOX to understand the changes of individual particle morphology and viscosity (Figure 3.1). Models have predicted the viscosity of SOA formed from the different VOC precursors and suggest the following viscosities of α-pinene SOA (9.3×10^7 Pa s),[178,186] β-caryophyllene SOA at (3.7×10^8 Pa s),[67,197] isoprene SOA (3×10^1 - 2×10^5 Pa s),[65] and toluene SOA (7.8×10^4 Pa s) at 50% RH.[66,184] Importantly, the viscosities of α-pinene and β-caryophyllene ozonolysis SOA are orders of magnitude higher than isoprene and toluene SOA from OH oxidation.[65-67,178,184,186,197] After the phase-separated SOA particles were exposed to IEPOX, particle-phase chemical reactions of IEPOX in the aqueous sulfate core formed viscous species, which can change the phase state of the core from liquid to semi-solid or solid.[25,38] Different types of SOA coatings on acidic inorganic sulfate particles can change the amount of IEPOX uptake.[21] Specifically, high-viscosity SOA coatings can limit the ability of gaseous species, such as IEPOX, to diffuse into the aqueous acidic core of the particle, which will kinetically-limit heterogeneous/multiphase processes and reaction rates, as well as overall particle

morphology and viscosity.[21,25] The average height profile can be used as a proxy for aerosol viscosity, with taller particles representing more viscous SOA coatings.[162] The results show that α-pinene and β-caryophyllene SOA have a clear decrease in height, and thus viscosity. After IEPOX reactive uptake compared to minimal changes in height for toluene and isoprene SOA-coated particles of the same size.

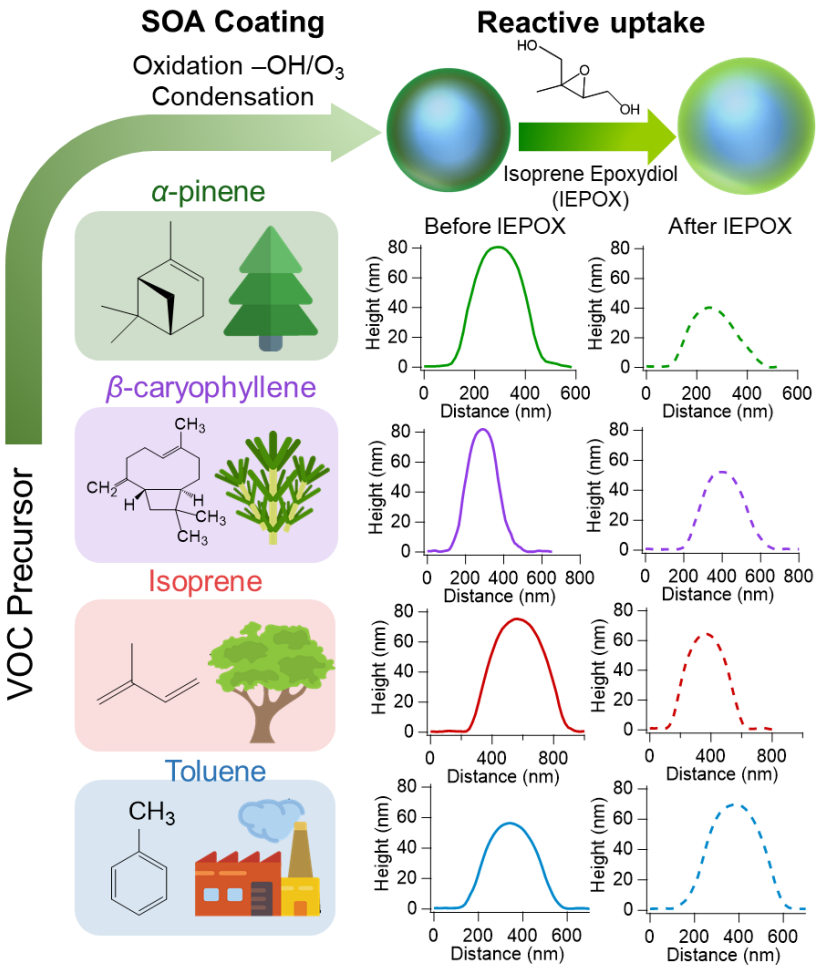

Figure 3.1. Experimental design showing toluene, isoprene, α-pinene, and β-caryophyllene SOA formation on acidic sulfate aerosol particles, and an average height profile of 10 particles changes before (solid lines) and after IEPOX uptake (dash lines). Images of four VOC precursor sources are from Flaticon.com.

Modifications to aerosol morphology and viscosity were quantitatively characterized before and after IEPOX uptake using spreading ratios calculated for size-selected 150 nm particles with α-pinene, β-caryophyllene, isoprene, and toluene SOA coatings. For α-pinene SOA, particles exhibited core-shell (inorganic-organic) morphology after coating with α-pinene ozonolysis

products shown in the AFM phase images (Figure 3.2a), similar to previous observations.[21,198] A thicker coating was observed for 150 nm α-pinene SOA after IEPOX uptake as shown by the larger dark outer portion in the AFM phase image. The morphology of the core indicates that after IEPOX reactive uptake, the aqueous core has been converted to a semi-solid or solid phase. Changes in SOA particle viscosity were quantified by calculating the average spreading ratios of ~100 individual particles. Large spreading ratios represent liquid-like particles of lower viscosity, whereas a smaller spreading ratio suggests solid-like particles of higher viscosity.[19,96] Before IEPOX uptake, both α-pinene and β-caryophyllene SOA are more viscous than isoprene and toluene SOA with lower spreading ratios, consistent with previous studies.[65-67,178] The spreading ratio of α-pinene SOA-coated sulfate particles increased significantly after IEPOX uptake from 3.4 ± 0.1 to 7.3 ± 0.4 at 50% RH. This surprising viscosity decrease is attributed to the formation of lower molecular weight (MW) organic species from IEPOX that have lower average MWs than α-pinene SOA,[28,96,199-201] some of which formed in or diffused into the shell.

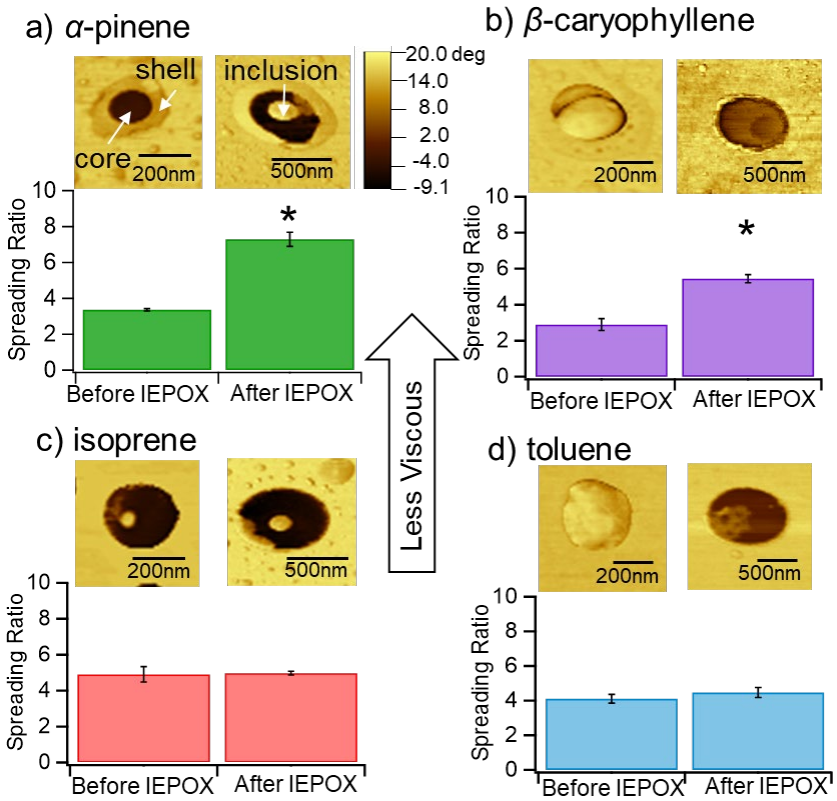

Figure 3.2. AFM phase images and spreading ratios of 150 nm SOA before and after IEPOX uptake (numbers of individual particles were calculated). a) α-pinene SOA (101 and 55); b) β-caryophyllene SOA (132 and 49 individual particles); c) isoprene SOA (99 and 61); d) toluene SOA (131 and 248); Single asterisks denote spreading ratios that are statistically different than SOA particles before IEPOX uptake ($p < 0.05$) and error bars represent 2σ from gaussian fit.

As indicated by AFM phase images (Figure 3.2b), 150 nm β-caryophyllene SOA-coated sulfate particles had partially engulfed morphology before IEPOX uptake After IEPOX uptake, the 150 nm β-caryophyllene SOA-coated sulfate particles retained their partially engulfed morphologies, and the spreading ratio significantly increased from 2.9 ± 0.3 to 5.4 ± 0.2. β-caryophyllene has higher MW oxidation products[202-204] compared to IEPOX SOA, as with α-pinene SOA, and similarly increased spreading ratios and a lower viscosity were observed after IEPOX reactive uptake. Future work will focus on using specific species and functional groups to further characterize these changes, as opposed to MW.[205]

Isoprene SOA-coated sulfate particles (150 nm) exhibited core-shell morphologies with a thick shell both before and after IEPOX reactive uptake (Figure 3.2c). Spreading ratios for 150 nm isoprene SOA-coated sulfate particles are similar before and after IEPOX uptake (4.9 ± 0.4 and 4.9 ± 0.1) as the overall MW and oxidation of the SOA from IEPOX multiphase chemistry is not substantially changing the chemical composition of the shell,[26,206] resulting in similar viscosities for the same size particles.

For toluene SOA particles, a homogeneous morphology was most prevalent (Figure 3.2d).[19] The spreading ratios of toluene SOA-coated particles are similar before and after IEPOX uptake (4.1 ± 0.2 and 4.5 ± 0.3) at ~50% RH, likely due to the lower MW of toluene SOA being closer to isoprene SOA than SOA from α-pinene or β-caryophyllene.[58,184,207] Larger area AFM phase images for the four types of SOA before and after IEPOX uptake with numerous particles are shown in the Supporting Information (Figure B.3) to demonstrate that the individual particles shown in detail in Figure 3.2 are representative.

After IEPOX reactive uptake, the detailed morphology and viscosity for SOA-coated sulfate particles with different sizes were investigated. For α-pinene SOA-coated sulfate particles (Figure 3.3), a core-shell morphology was observed after IEPOX uptake (Figure 3.3b and 3.3c). Inclusions were observed for 150 nm particles and these inclusions could be viscous organosulfates or organosulfate oligomers that salt out when sufficient amounts form.[19,30,38,175] However, the inclusions were too small for chemical analysis by the AFM-PTIR available at the time. As the particle size increased from 150 to 250 nm, the spreading ratio significantly decreased from 7.3 ± 0.4 to 4.7 ± 0.2 (Figure 3.3a and 3.3d) at ~50% RH, indicating a more viscous particle likely due to an increase in the amount of sulfate available in the core for IEPOX to react with and form

viscous species, such as organosulfates and their oligomers.[168,175,208-210] This result is consistent with a previous study suggesting the viscosity of large (~1 μm) α-pinene SOA-coated sulfate particles increased after uptake of gaseous IEPOX.[19] β-caryophyllene SOA-coated particles exhibited the same size-dependent spreading ratio behavior as α-pinene SOA-coated sulfate particles, with larger particles spreading less (Figure B.4).

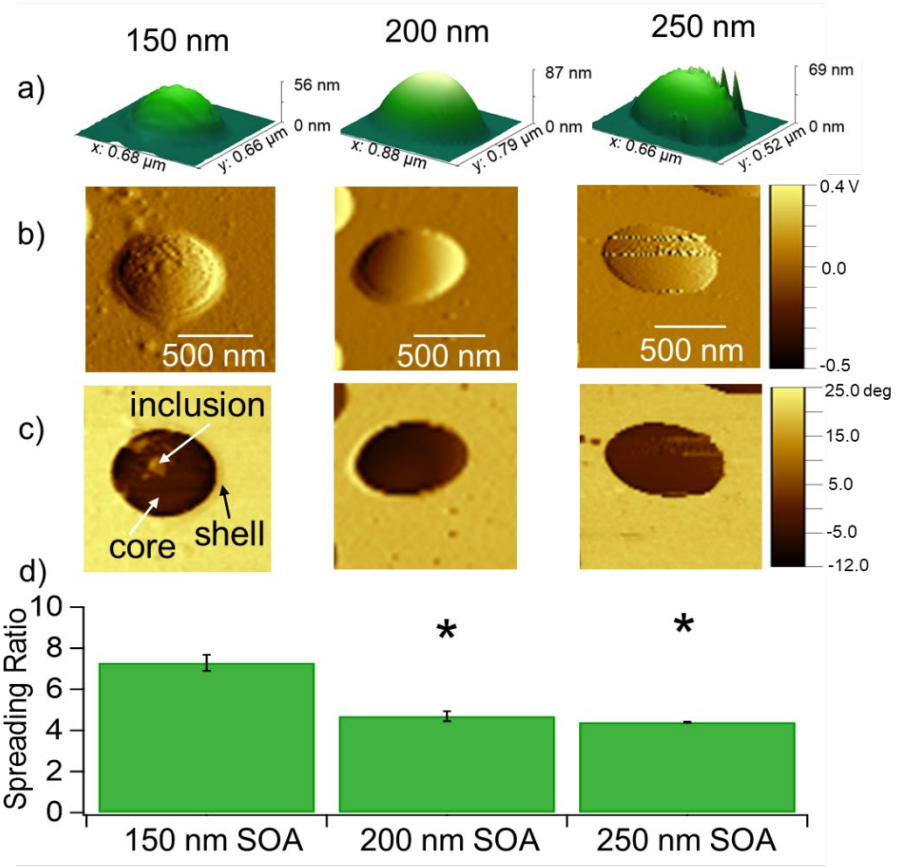

Figure 3.3. Morphology and the spreading ratio of size-selected α-pinene SOA after IEPOX uptake. a) Representative 3D AFM images; b) AFM amplitude images; c) AFM phase images; d) Bar charts show the average spreading ratio of individual particles for α-pinene SOA with 150 nm (55 particles), 200 nm (155 particles), and 250 nm (43 particles) diameters; single asterisks denote spreading ratios of larger particles that are statistically different than 150 nm particles ($p < 0.05$) and error bars represent 2σ from gaussian fit.

For size-selected isoprene SOA, morphology was more complex than traditional core-shell morphology and this complex morphology was observed for both larger sizes of particles (200 nm and 250 nm) (Figure 3.4b and 3.4c). This suggests that the products of IEPOX reactions were distributed heterogeneously within the particles,[19,21] leading to irregular shapes. The average spreading ratio for all sizes of isoprene SOA particles ranges from 3.7 ± 0.2 to 4.9 ± 0.1 (Figure 3.4a and 3.4d) at ~50% RH. As isoprene SOA size increased from 150 nm to 250 nm, the spreading ratio decreased from 4.9 ± 0.1 to 4.1 ± 0.1 at ~50% RH, suggesting higher viscosity with increasing particle size. While increased viscosity was observed for α-pinene, β-caryophyllene, and isoprene SOA particles with increasing size, toluene SOA particles did not follow this trend, potentially due to toluene SOA having homogeneous morphology versus the morphologies (core-shell, partially engulfed, and complex) for the other SOA (Figure B.5).

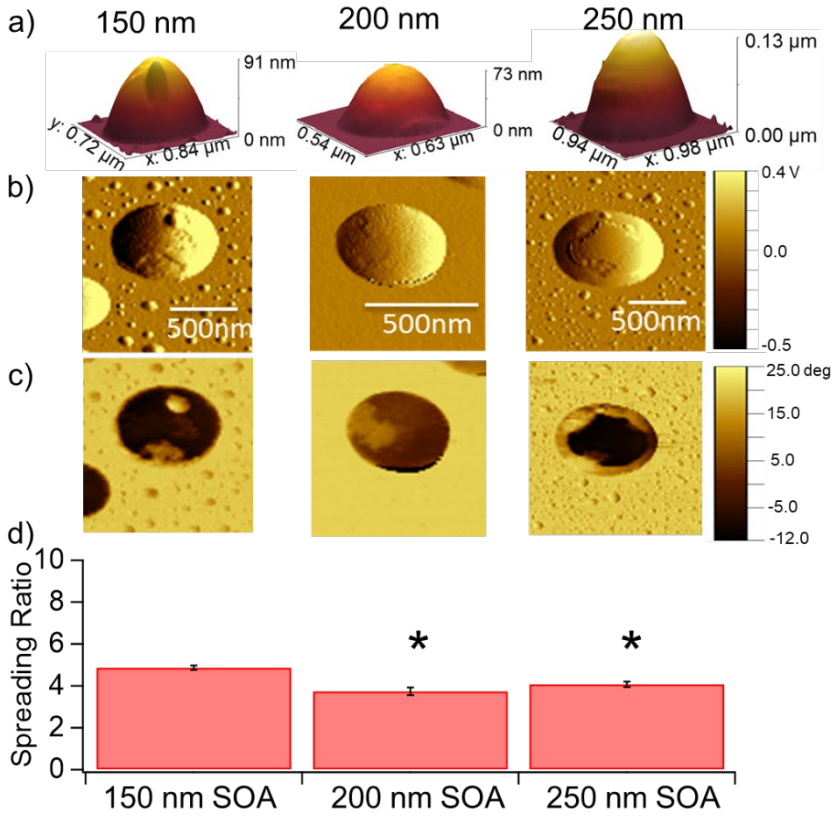

Figure 3.4. Morphology and the spreading ratio of size-selected isoprene SOA after IEPOX uptake. a) Representative 3D AFM images; b) AFM amplitude images; c) AFM phase images; d) Bar charts show the average spreading ratio individual particles for isoprene SOA with 150 nm (61 particles), 200 nm (87 particles), and 250 nm (128 particles) diameters; single asterisks denote spreading ratios of larger particles that are statistically different than 150 nm particles ($p < 0.05$) and error bars represent 2σ from gaussian fit.

The chemical composition of individual submicron SOA particles is key to further understand the modification of SOA morphology and viscosity before and after IEPOX uptake and was analyzed using Raman microspectroscopy, AFM-PTIR, and SEM-. Raman spectra were taken of the particle core and shell of *α*-pinene SOA-coated particles before and after IEPOX uptake (Figure 3.5). Before IEPOX uptake, Raman spectra showed peaks representing $\nu_s(SO_4^{2-})$ at 973, $\nu_s(HSO_4^-)$ at 1049 cm^{-1}, $\nu_s(R\text{-}OSO_3^-)$ 1074 cm^{-1}, and the broad ν(N-H) region around 3160 cm^{-1} indicating sulfate, bisulfate, *α*-pinene organosulfates, and ammonium located primarily in the particle core.[85,211-216] A carbonyl group ν(C=O) mode was observed at 1708 cm^{-1},[217] corresponding to *α*-pinene oxidation compounds, such as pinic acid or pinonic acid.[218-220] A peak at 1448 cm^{-1} is assigned to the methyl/methylene group bend $\delta(CH_3/CH_2)$, whereas peaks at 2882 cm^{-1} and 2931 cm^{-1} are assigned to symmetric stretches of ν_s(C-H) of methyl groups and asymmetric stretches ν_{as}(C-H) in methylene groups, respectively.[211] The different chemical composition of the particle core and shell confirm the phase separations observed by microscopy, with acidic ammonium sulfate and some organosulfates in the particle core and organic material (*α*-pinene oxidation

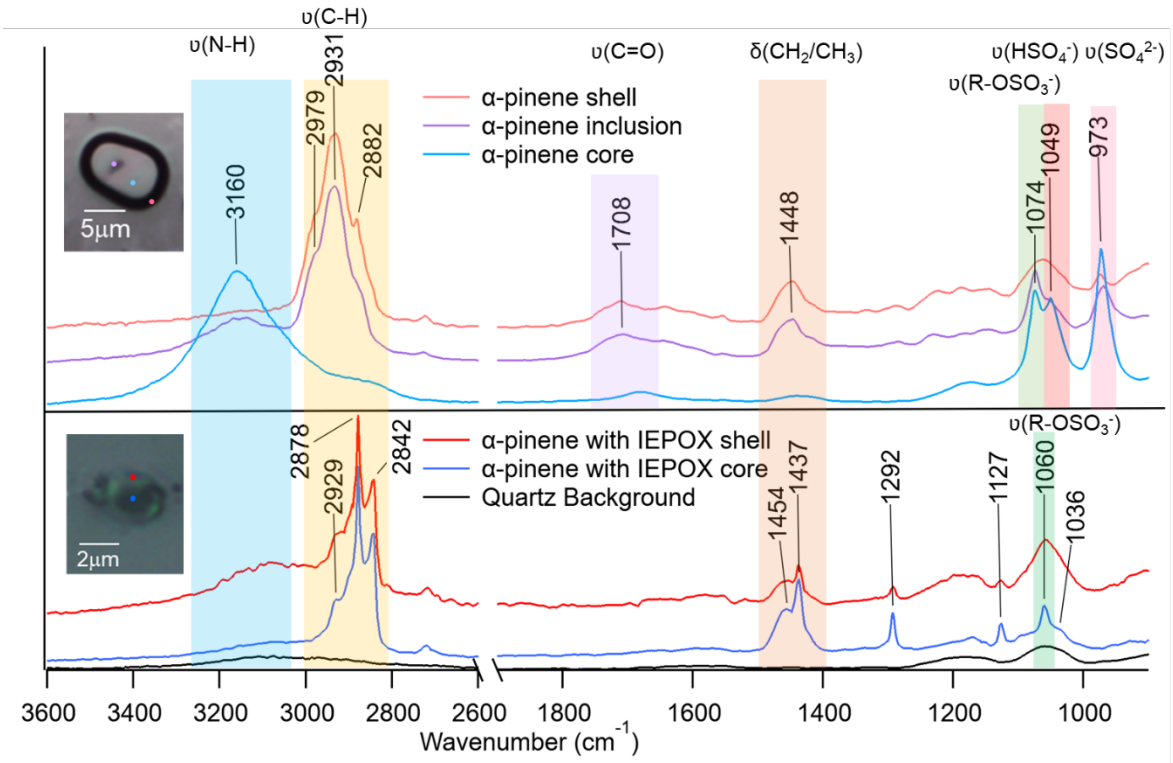

Figure 3.5. Raman spectra of representative α-pinene SOA core and shell before IEPOX uptake (top); Representative α-pinene SOA core and shell after IEPOX uptake (bottom). The color dots in the optical images represent the different locations of Raman spectra were collected.

products) in the shell. An inclusion was observed for α-pinene SOA and the Raman spectrum suggests α-pinene organosulfates can be produced during the formation of the shell which could explain the inclusions were observed in AFM images (Figure 3.3b and 3.3c). After IEPOX uptake, IEPOX-derived organosulfate formation is observed by $\nu_s(R\text{-}OSO_3^-)$ at 1060 cm^{-1}, which has been characterized previously,[19,168] and peaks between 2800 to 3000 cm^{-1} indicative of the C-H stretching region. The shape of the C-H stretching region also shifts, from modes at 2931 and 2972 before IEPOX to modes at 2880 and 2842 being most prominent afterwards, indicative of changes to the organic material in the shell (more symmetric methyl and methylene stretches). Raman spectra for toluene, isoprene, and β-caryophyllene SOA-coated sulfate particles before and after IEPOX show similar results as for α-pinene SOA, and are discussed in the Supporting Information (Figure B.6, B.7, B.8). EDX spectra were consistent with Raman spectra after IEPOX reactive uptake and showed sulfate and oxygen present in the particle cores (indicative of inorganic sulfate and/or organosulfate species), with carbon and oxygen primarily present in the shell (Figure B.9).

IR spectra were collected for 250 nm toluene and β-caryophyllene SOA-coated sulfate particles after IEPOX uptake using AFM-PTIR (Figure 3.6a). A strong peak at 1104 cm^{-1} was observed, which corresponds to the highly IR-active anti-symmetric stretch of inorganic sulfate ions, $\nu_{as}(SO_4^{2-})$, in the particle core.[73] The peaks at 1420 cm^{-1} for a β-caryophyllene SOA-coated particle and 1436 cm^{-1} for a toluene SOA-coated particle are assigned to ammonium $\delta(NH_4^+)$.[73] A less intense N-H stretch of ammonium at 3136 cm^{-1} was also observed.[73] The peaks detected at 1072 cm^{-1} and 1068 cm^{-1} suggest the formation of organosulfates, $\nu_s(R\text{-}OSO_3^-)$.[168,221] A symmetric methyl stretch $\nu_s(CH_3)$ was observed at 2880 cm^{-1} for the β-caryophyllene SOA-coated particle, and an organic peak at 3060 cm^{-1} is assigned to unsaturated C-H moieties (i.e., less sp^3 hybridized) within the organic species of the C-H stretching region.[211] Peaks > 3150 cm^{-1} correspond to O-H stretching.[167,217] As shown in Figure 3.6b, IR spectra of 250 nm isoprene SOA particle core and shell after IEPOX uptake display two strong modes, 1100 cm^{-1} and 1424 cm^{-1} suggestive of $\nu_{as}(SO_4^{2-})$ and $\delta(NH_4^+)$, respectively,[73] in the particle core. A weak mode, ν(C=O) at 1690 cm^{-1} was observed in both core and shell. The complex core of isoprene SOA (Figure 3.6c**)** suggests that some IEPOX diffused into the particle and reacted with inorganic sulfate. To directly visualize relative differences in the spatial distribution of sulfate and organic species between the core and shell of isoprene SOA-coated sulfate particles, a ratio map (Figure 3.6d) was generated using 1100 cm^{-1}/1690 cm^{-1}. The areas enriched in sulfate (1100 cm^{-1}) appear red (this may include some

organosulfates due to the peak widths and the proximity of the 1100 and 1074 cm^{-1} peak), while those with enhanced carbonyl concentrations (1690 cm^{-1}) appear green. The ratio map confirms that most sulfate is in the particle core and isoprene-derived organic materials are in the shell, which is consistent with Raman and EDX spectra.

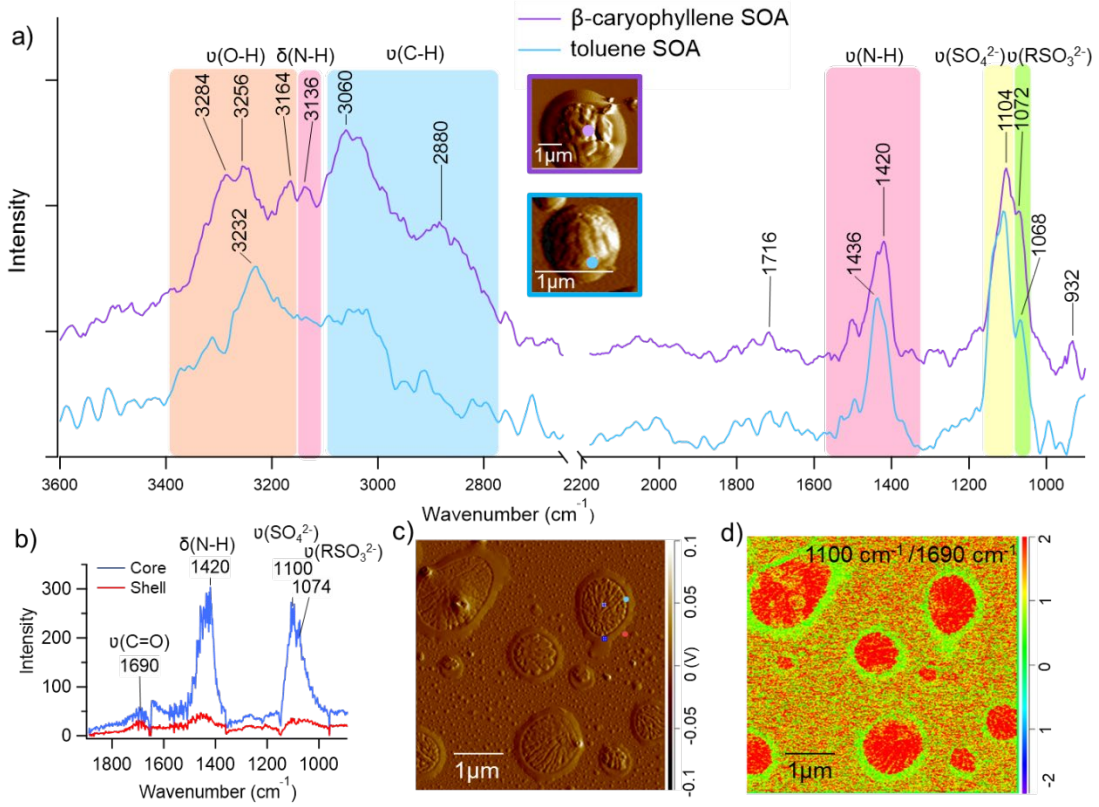

Figure 3.6. a) AFM-PTIR spectra of β-caryophyllene SOA-coated and toluene SOA-coated particles after IEPOX uptake with AFM amplitude images; b) IR spectra of isoprene SOA core and shell; c) AFM amplitude image of isoprene SOA; d) IR ratio map of 1100 cm-1/1690 cm-1 for isoprene SOA.

3.4 Conclusions

To understand the atmospheric impact of IEPOX uptake onto SOA-coated acidic sulfate particles, SOA coatings from different VOC precursors need to be understood. The viscosity and morphology of size-selected SOA formed from four different VOC precursors (*α*-pinene, *β*-caryophyllene, isoprene, and toluene) before and after IEPOX uptake have been investigated in this study. The results demonstrate that changes in viscosity and morphology of initial inorganic core-SOA shell particles after IEPOX reactive uptake are strongly dependent on VOC precursor. *α*-Pinene and *β*-caryophyllene SOA-coated sulfate particles became less viscous after IEPOX uptake, while the viscosity of isoprene and toluene SOA-coated sulfate particles did not change

appreciably after IEPOX uptake. The changes in particle viscosity can affect IEPOX diffusion and mixing time scales, which may alter SOA lifetime and the production of further SOA in these mixed organic-inorganic particles (i.e., self-limiting further atmospheric aging[38,96]). Additionally, different SOA particle sizes after IEPOX uptake (150, 200, and 250 nm from initially 150 nm particles) have been investigated, with phase separation and more particles with complex morphology being observed at larger particle sizes.[19,222] After IEPOX uptake, the larger particles were more viscous for α-pinene, β-caryophyllene, and isoprene SOA-coated sulfate particles, indicating particle size could play an important role in morphology, affecting subsequent heterogeneous reactions. The VOC- and size-dependent morphology and viscosity changes are important to consider since inorganic-SOA mixed particles play an important role in overall aerosol mixing state,[79,148-150] as well as cloud condensation nuclei (CCN) [223] and ice nucleating particle (INP) activity,[177,224,225] which are important in cloud formation.[226-228]

3.5 Acknowledgements

This work was supported by the National Science Foundation (NSF) Grant No. AGS-1506768 (Ault) and No. AGS-1703535 (Surratt). A.G., Z.Z., and J.D.S. also acknowledge support from NSF Grant No. AGS-2001027 (Gold). Y.Z acknowledges the support from NSF-AGS Postdoctoral Fellowship (Grant No. 1524731). The authors would like to thank the Michigan Center for Materials Characterization (MC2) for access to and assistance with the SEM-EDX, which is supported by the University of Michigan College of Engineering. The authors acknowledge the Scanning Probe Microscopy facility in Department of Chemistry at the University of Michigan.

Chapter 4. Initial pH Governs Secondary Organic Aerosol Viscosity and Morphology after Uptake of Isoprene Epoxydiols (IEPOX)

Ziying Lei, Yuzhi Chen, Yue Zhang, Madeline E. Cooke, Isabel Ledsky, N. Cazimir Armstrong, Nicole E. Olson, Zhenfa Zhang, Avram Gold, Jason D. Surratt, Andrew P. Ault. *Environmental Science &Technology, 2021* (Under Review)

4.1 Introduction

Atmospheric aerosols significantly affect air quality, human health, and climate; particularly submicron particles, which have long atmospheric lifetimes, determine cloud nucleating properties, and penetrate deeply into the lungs after inhalation.[229] Secondary organic aerosol (SOA) is ubiquitous, accounting for a large mass fraction of submicron aerosol particles[146,230-232] and more than 50% of the total organic aerosol mass globally.[17,233] Recent studies have shown that SOA is possibly linked to adverse human health outcomes upon inhalation exposure, including early biological changes within lung cells that are associated with inflammation and oxidative stress.[10,234-237]

SOA is largely formed by the oxidation of volatile organic compounds (VOCs) followed by nucleation, condensation, or multiphase chemical reactions of the resulting lower volatility oxidation products, which all lead to increased SOA mass.[20,210] Isoprene has the highest emissions of any non-methane VOC with global emission rates of ~600 Tg/y,[238,239] and undergoes oxidation to form lower volatility gaseous species, such as isoprene epoxydiols (IEPOX).[240,241] When the oxidation of isoprene to IEPOX occurs, the increasing molecular functionality and decreasing vapor pressure (3×10^{-6} atm)[177] facilitate reactive uptake to existing aerosol particles,[17,20,26,173,196] particularly under low pH conditions when the epoxide can be opened via acid-catalyzed reaction pathways.[242,243] Previous studies have shown that high IEPOX reactive uptake to inorganic sulfate particles leads to the formation of substantial amounts of aerosol mass (i.e., particulate matter < 2.5 μm, $PM_{2.5}$), especially in the Southeastern United States.[244-247] Due to the large mass loadings of IEPOX-derived SOA, which can contribute up to 40% of the submicron organic aerosol mass

in isoprene-rich environments,[244,248] the physicochemical properties (i.e., phase state and morphology) of these aerosol particle types can affect further SOA formation and the evolution of existing SOA.[21,38,96]

The phase state (liquid, semi-solid, or solid) of atmospheric particles plays a critical role in determining their ability for further chemical reactions in the aerosol phase.[21,47,249] In the past decade, studies have shown that SOA particles can exist in an amorphous semi-solid or solid state under different ambient conditions (e.g. relative humidity (RH) and temperature),[45,58] and the viscosity of SOA particles can have a wide range of viscosities from 3 x 10^1 Pa s (similar to honey) to 3.7 x 10^8 Pa s (similar to tar pitch).[58,66,67,178,250] Multiphase chemistry of IEPOX leads to the formation of organosulfates,[168,174,175,208] polyols,[17,27,30,251,252] and oligomers[20,28,253] in the condensed phase, whose high molecular weights result in more viscous aerosol (i.e., 10^6 Pa s).[25] Increases in viscosity decrease molecular diffusion and lead to longer mixing timescales for molecules within particles, which have been shown to decrease subsequent gaseous IEPOX uptake and SOA formation.[19,21,25,57] Due to decreased miscibility of organic components in high ionic strength aqueous phases, the viscous organic components of a particle salt out to form an outer layer (i.e. shell) at the edge of the inorganic components (i.e. core), commonly referred to as core-shell morphology.[37,46,254] For the resulting core-shell morphology, if the shell is highly viscous, it can kinetically inhibit further uptake of gaseous species,[178,255] reactivity,[25,38,256,257] and ultimately SOA growth and evolution in the atmosphere.[178] Thus, understanding the phase state, viscosity, and morphology of SOA particles is central to predicting heterogeneous uptake of IEPOX leading to SOA formation.

Aerosol pH also has substantial impacts on SOA formation by modifying the reaction rates of organic species within the condensed phase.[258,259] Many atmospheric multiphase chemical processes are pH-dependent, including the reactive uptake of IEPOX to form SOA and many subsequent reactions in the condensed phase.[24,26,196] Atmospheric chamber experiments have observed that greater SOA formation occurs under acidic conditions (pH 1.5) compared to neutral conditions (pH 5).[30,242] As an example, the acid-catalyzed ring-opening reaction of IEPOX leads to lifetimes of less than one minute after uptake to particles with pH < 1, but IEPOX can have lifetimes of days or longer in particles at pH 5 under typical atmospheric conditions.[26,210] However, there remains considerable uncertainty regarding how aerosol pH impacts the resulting morphology and viscosity after IEPOX uptake.

Further experimental data is needed in order to improve our current understanding of how exactly acid-catalyzed multiphase chemical reactions of gaseous IEPOX with particles of varying acidity subsequently affect particle morphology and viscosity. In this study, we investigated changes in particle phase state and morphology after gaseous IEPOX uptake onto particles with varying initial acidities (i.e., pH = 1, 3, and 5) and amounts of ammonium sulfate and sulfuric acid. We also characterized the time-resolved modification of particle morphology and chemical composition after different reaction times (i.e., 30, 60, and 120 minutes after gaseous IEPOX injection). Individual particles were characterized by using multiple microspectroscopy methods (atomic force microscopy coupled with photothermal infrared (AFM-PTIR), scanning electron microscopy (SEM), and Raman microspectroscopy) in order to provide detailed information on individual particle morphology, phase state, and chemical composition during and after IEPOX reactive uptake. These single particle data were compared with changes in aerosol size distributions and organosulfate concentrations of the total aerosol generated during our chamber studies. Establishing the physicochemical properties of SOA formed under varying initial pH conditions is crucial for resolving the impacts of atmospheric aerosol on human health and climate (e.g., cloud droplet or ice crystal nucleation).[4,224,260]

4.2 Methods

4.2.1 Chamber Experiments

Aerosol particles were generated from solutions with different pH values where the concentration of the inorganic sulfate ions (sulfate ($[SO_4^{2-}]$) + bisulfate ($[HSO_4^-]$)) was kept at 0.12 M for each solution. Solutions that were prepared using ammonium sulfate (Sigma Aldrich, ≥ 99% purity), sulfuric acid (Sigma Aldrich, ≥ 98% purity), and 18.2 MΩ Milli-Q water (**Table 1**), without further purification. The pH, chemical composition, and submicron size of the seed aerosol were chosen to represent conditions under which SOA formation reactions occur in the atmosphere.[29,261,262]

Table 4.1 Solutions used for seed aerosol, labels used in text, measured solution pH with uncertainty prior to aerosolization, and concentrations of sulfuric acid and ammonium sulfate. N/A = not applicable

Seed Acidic Aerosol Solution	Label	Measured pH	$[H_2SO_4]$	$[(NH_4)_2(SO_4)]$
pH = 1 without ammonium	pH 1 w/o NH_4^+	1.05 ± 0.01	0.12 M	N/A
pH = 1 with ammonium	pH 1 w/NH_4^+	1.32 ± 0.01	0.06 M	0.06 M
pH = 3	pH 3	2.99 ± 0.01	0.0025 M	0.1175 M
pH = 5	pH 5	5.19 ± 0.01	N/A	0.12 M

The pH of the bulk solutions was measured by a pH probe (PHS-3C, Yantai Stark Instrument Co.). Aerosols were generated from a constant output atomizer (TSI Inc., Model 3076) and then passed through diffusion driers to reach 50% RH, which is above the efflorescence RH of ammonium sulfate and sulfuric acid to maintain the aerosol in an aqueous form. The number size distribution of the different seed aerosols (mode diameters: 83-103 nm) and SOA aerosols after reacted with IEPOX for 120 min (101-133 nm) are shown in Figure C.1. Acidic seed particles were injected into the 10-m^3 indoor chamber at the University of North Carolina at Chapel Hill (UNC) chamber facility that was pre-humidified to 50% RH,[30,38] and the concentration was allowed to stabilize for 30 min. Synthesized *trans-β*-IEPOX,[195] which is the predominant IEPOX isomer in the atmosphere,[241] was dissolved in ethyl acetate and gaseous IEPOX was injected into the chamber by using a high-purity nitrogen flow of 2 L min^{-1} for 10 min, and then 4 L min^{-1} for 50 min through a heated manifold (60 °C).[19,21,30,38,196] The seed particles with different initial pH values reacted with gaseous IEPOX to form IEPOX-derived SOA. A scanning electrical mobility spectrometer (SEMS, BMI Inc., Model 2100) was used to monitor the particle growth by measuring aerosol size distributions, number concentrations (#/cm^3), and volume concentrations ($\mu m^3/cm^3$) in the chamber. After the seed particles were exposed to the injected IEPOX for 30, 60, and 120 minutes, aerosol particles were inertially impacted onto substrates for microscopy using an eight-stage mini-multi orifice uniform deposit impactor (mini-MOUDI, Model 135, TSI Corp.). Particles were analyzed from stage 7, which has a 50% aerodynamic cut-point of 320 nm (d_{50}) leading to particles with diameters of 180-320 nm on the substrates. Microscopy substrates included silicon wafers (16014, Ted Pella, Inc.), carbon-type-b Formvar-coated copper

transmission electron microscopy (TEM) grids (1GC50, Ted Pella, Inc.), and quartz pieces (26016, Ted Pella, Inc.).

4.2.2 Microscopy Imaging and Spectroscopy

The morphology and phase of individual submicron particles were analyzed using an AFM-PTIR (nanoIR2, Anasys Instruments, Santa Barbara, CA). Particles on silicon substrates were imaged in 5 × 5 μm^2 and 10 × 10 μm^2 regions with 0.7 Hz scan rates that operated at a 0.07-0.4 N/m spring constant and 13 ± 4 kHz resonant frequency. Tapping IR mode was conducted with a gold-coated microfabricated silicon probe (AU.1000.SWTSG, Platypus Technologies). Raw data were processed using SPIP 6.2.6 software (Image Metrology, Hørsholm, Denmark) to measure single particle height, radius, and volume. The spreading ratios of individual particles were calculated by using particle radius divided by particle height (SR = r/h), as described in previous publications.[19,73,96] Spreading ratio uncertainties are reported as 2σ of a Gaussian fit to the histogram of spreading ratios. T-tests were used to compare the spreading ratio of seed particles with mixed seed-SOA particles at discrete time points during the experiment (i.e., 30, 60, and 90 minutes) and were considered to be statistically different for p values < 0.05. SEM images were also obtained for particles impacted onto TEM grids using a FEI Helios 650 Nanolab-Dualbeam electron microscope equipped with a high angle annular dark field (HAADF) detector operated at an accelerating voltage of 10.0 kV, a current of 0.80 nA, and pressures ranging from 10^{-5} to 10^{-6} Pa.[263]

AFM-PTIR (nanoIR2 system, Anasys Instruments, Santa Barbara, CA) was used to characterize the chemical composition of individual particles. IR spectra were collected using an optical parametric oscillator (OPO) source with a tuning range of 800 to 3600 cm^{-1} and an average spectral resolution of 2 cm^{-1}. For each sample, the IR spectra were collected at a scan rate of 100 cm^{-1}/s for 5 minute acquisitions, and averaged after 3 accumulations.[73]

Raman microspectroscopy was used to characterize the chemical composition of phase-separated particles, as in prior studies.[85] Spectra for both the particle core and shell were collected using a LabRAM HR Evolution Raman microspectrometer (Horiba, Ltd.) equipped with a 50 mW 532 nm Nd:YAG laser source, a confocal optical microscope (Olympus, 100 × 0.9 N.A. objective), and a CCD detector. Each Raman spectrum was collected in the range of 500 to 4000 cm^{-1} with three accumulations at 60 s acquisition times. A diffraction grating with 1800 groove/mm was

used to yield a spectral resolution of 0.7 cm^{-1}. Both PTIR and Raman spectra were collected at room temperature, RH, and ambient pressure.

4.2.3 Characterization of Organosulfate Formation

For each chamber experiment, particles were collected using a particle-into-liquid sampler (PILS, BMI model 4001). PILS samples were collected every 6 minutes with an air sampling rate ~6.5 L min^{-1}, resulting in a liquid sample volume of ~ 1.2 mL, which was used for offline chemical analysis by ion chromatography (IC).[38] IC conditions have been previously summarized by Riva et al.[38,264] PILS samples were stored in the dark at 2 ℃ immediately after collection and were analyzed within 24 hours, as validated in prior work.[38] In this study, the sulfate concentration in the initial atomizer solution was kept constant at 0.12 M (Table 1) and the total particulate organosulfate concentrations with specific reaction time can be calculated by subtracting inorganic sulfate concentrations from the initial sulfate concentration measured by IC (which is initially all inorganic sulfate).[25,38] The initial sulfate concentration of a seed aerosol only experiment was also analyzed (Figure C.2) to compare with IEPOX-derived SOA experiments.

$$[Sulfate_{Organic}]_t = [Sulfate_{Total}]_0 - [Sulfate_{IC}]_t$$

Additionally, a hydrophilic interaction liquid chromatography (HILIC)/ESI-HR-quadrupole time-of-flight mass spectrometry (QTOFMS) was used to characterize 2-methyltetrols (2-MT) and its OS derivative (2-methyltetrol sulfate, IEPOX-OS).[38,265]

4.3 Results and Discussion

The relative fraction of the HSO_4^- and SO_4^{2-} ions varies as a function of pH (Figure C.3), highlighting that bisulfate dominates (> 90 %) at pH 1 and sulfate dominates at pH 3 (> 90%) and pH 5 (> 99%) for the initial seed aerosol particles. After gaseous IEPOX was injected into the chamber, the volume concentration ($\mu m^3/cm^3$) of the aerosol increased, with the greatest volume growth observed with pH 1 seed aerosol particles either with or without ammonium (NH_4^+). The total aerosol particle volume reached its maximum value 30-60 minutes after the IEPOX injection finished (**Figure 4.1**). For less acidic seed particles, such as pH 3 and pH 5 particles, a slight increase in total volume occurred through both experiments and the slight decrease later on during the experiment is due to wall loss after IEPOX is no longer being injected. These results expand

on prior studies,[24,210] which only examined acidic versus non-acidic seed particles and show here that high [H^+] is needed for growth, with or without ammonium in the seed.

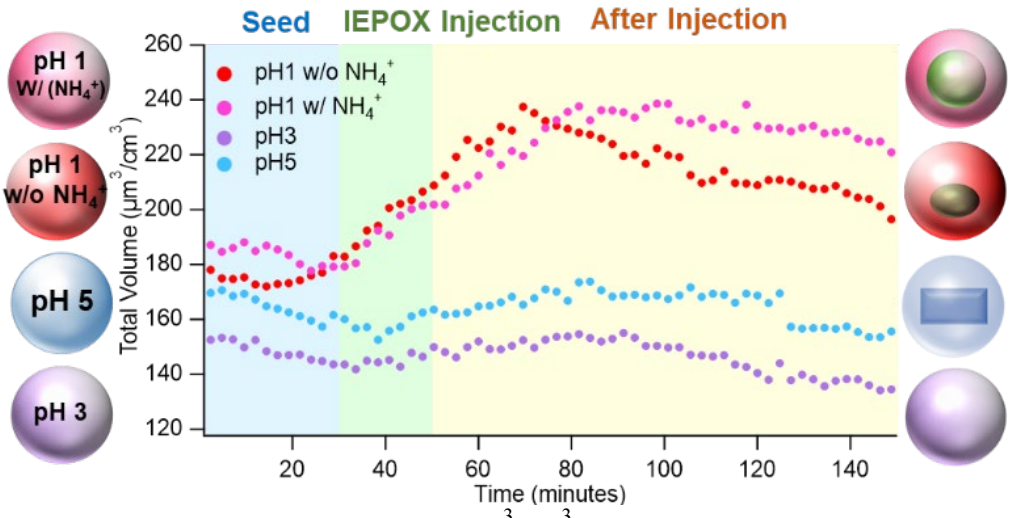

Figure 4.1. Particle volume concentration ($\mu m^3/cm^3$) after IEPOX uptake for different acidic inorganic sulfate particles: pH 1 (NH_4^+, HSO_4^- >> SO_4^-, H^+, H_2O) (pink solid circle), pH 1 (HSO_4^-, H^+, H_2O) (red solid circle), pH 3 (NH_4^+, H^+, SO_4^{2-} >> HSO_4^-, H_2O) (purple solid circle), and pH 5 (NH_4^+, H^+, SO_4^{2-}, H_2O) (blue solid circle). The volume concentration is calculated from integrated size distributions and has not been corrected for particle wall loss.

To determine how quickly core-shell morphology formed, AFM phase images were collected after pH 1 seed particles (without NH_4^+ counter ion) were exposed to gaseous IEPOX (Figure 4.2a). Particles exhibited phase separation after exposure to IEPOX for 30-, 60-, and 120-minutes reaction times. AFM phase images show that a coating (black color) formed quickly after the initially homogenous seed aerosol particle is exposed to IEPOX for 30 minutes, and the circular morphology indicates that the particles were liquid and had not effloresced prior to injection into the chamber.[166,266,267] With increasing IEPOX : SO_4^{2-} ratios throughout the reaction time (as SO_4^{2-} is incorporated into organosulfates, Figure C.4),[38] a thicker coating formed, consistent with the previous studies.[21,25,38]After 60 minutes of IEPOX uptake, the particle core became smaller, and a thicker coating was observed (Figure 4.2b). After 120 minutes of IEPOX uptake, the morphology of the core had inclusions, which may suggest the continuous reactive uptake of gaseous IEPOX continued to modify the core, even with a thicker coating, leading to less spherical, aqueous morphology. To further understand the viscosity change during IEPOX uptake, particle spreading ratios were calculated for individual particles.

Particle spreading ratios have been used as an indirect measurement of particle viscosity,[19,96] as more viscous particles spread less on the substrate leading to a smaller spreading ratio. The spreading ratios of pH 1 seed particles (without NH_4^+) and reacted pH 1 seed particles exposed to IEPOX for 30, 60, and 120 min were calculated, and are shown in Figure 4.2c. The pH 1 seed particles (without NH_4^+) before reaction with IEPOX had an average spreading ratio of 2.8 ± 0.2. Following IEPOX uptake, the average spreading ratios significantly decreased to 1.8 ± 0.1 after 30 min, 2.4 ± 0.1 after 60 min, and 2.1 ± 0.1 after 120 min of reaction time. Reactive uptake of IEPOX for 30 minutes led to increased particle viscosity, which has been shown by both measurements by Olson et al.[19] using an entrained-aerosol flow tube reactors with < 1 min residence times and modeling results from Zhang et al.[62] The formation of organosulfates and other oligomers has been shown to increase particle viscosity and phase separations.[19,38] After reacting for 60 and 120 min, a thicker coating formed and a smaller core was observed, which suggests that IEPOX was continuously reacting with seed particles, though the spreading ratios did not change significantly. This suggests most viscosity increases are likely facilitated by organosulfate

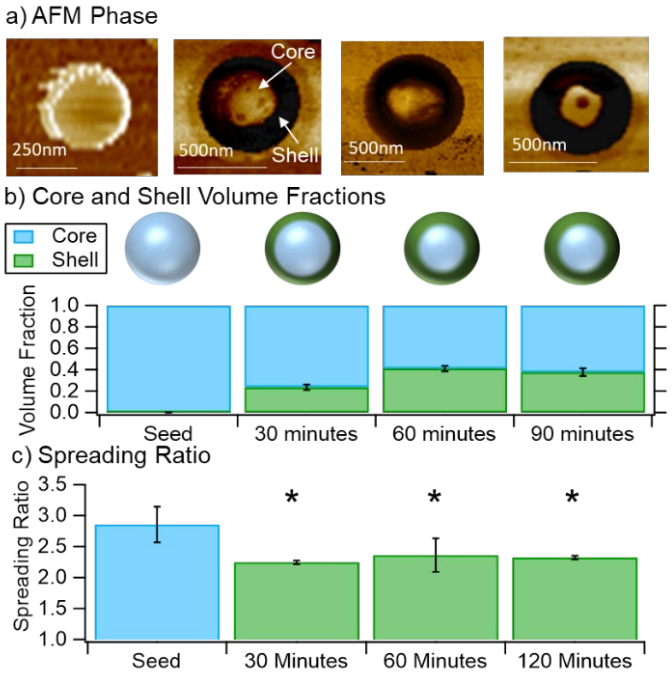

Figure 4.2. a) AFM phase image of representative pH 1 w/o NH_4^+ seed particles, particles after reaction with IEPOX for 30, 60, and 120 minutes; b) core volume fraction (blue) and shell volume fraction (green), the error bars represent standard error; c) Averaged spreading ratios of 249, 68, 78, 74 particles, respectively, single asterisks denote spreading ratios that are statistically different than seed particles before IEPOX uptake ($p < 0.05$), error bars represent 2σ from gaussian fit.

formation that occurs within 60 minutes, and that the particles were stable for at least the next hour, possibly due to a potential self-limiting effect.[25] These results demonstrate rapid modification of submicron particle phase states and viscosity during reactive uptake of gaseous IEPOX to pH 1 seed particles (without NH_4^+).

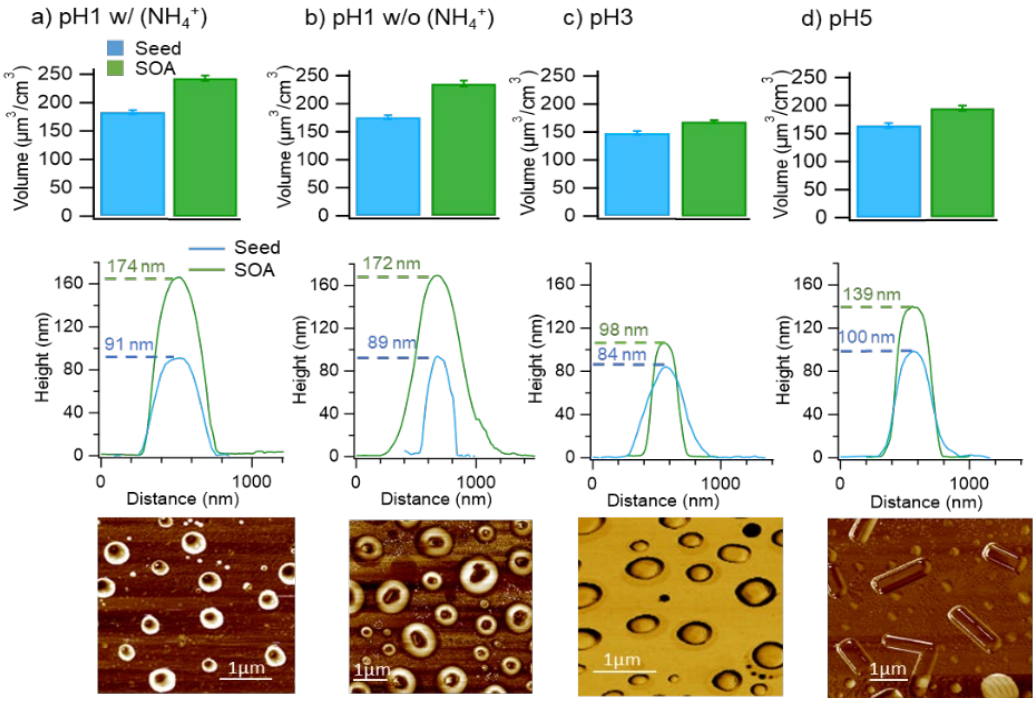

Figure 4.3 Particle volume concentration, average height trace of 10 individual particles, and AFM phase images for a). pH 1 seed particles with ammonium after IEPOX uptake; b). pH 1 seed particles without ammonium after IEPOX; c) pH 3 ammonium sulfate particles after IEPOX uptake; d) pH 5 ammonium sulfate particles after IEPOX uptake. Blue color represents the seed particles, and the green color represents the IEPOX derived SOA particles.

Particle volume concentrations of seed particles and particles after IEPOX uptake for 60 min are shown in Figure 4.3 (top row). A significant increase in IEPOX-derived SOA formation was observed for pH 1 seed particles with and without NH_4^+, with volume concentrations increasing 34.0 ± 0.4% and 31.9 ± 0.1 %, respectively. Similarly, the less acidic seed particles led to less volume growth (12.8 ± 0.9 % for pH 3 ammonium sulfate and 17.3 ± 0.3 % for pH 5 ammonium sulfate). These results are consistent with previous studies that show IEPOX-derived SOA formation is facilitated by acid-catalyzed particle-phase reactions.[25,30] In addition, average height traces of 10 individual particles are included in Figure 4.3 (middle row), which shows the average aerosol growth after SOA formation. A taller particle with the same width indicates a more viscous particle while a shorter particle is less viscous and has spread more.[19] As seed particles

became less acidic, the height and, by proxy, the viscosity of particles after IEPOX uptake was lower. This is because IEPOX-derived organosulfates (and oligomers) that increase particle viscosity are more likely to be formed under acidic conditions.[19,21,38,268] To connect greater SOA formation and higher viscosity to core-shell morphology, phase imaging was used to characterize particles after gaseous IEPOX uptake onto particles with different initial pH values. AFM phase images in Figure 4.3 (bottom row) demonstrate that phase separation only occurs for the pH 1 particles (with or without NH_4^+) after exposure to gaseous IEPOX. AFM phase images suggest that the SOA particles generated under acidic conditions formed a thick SOA coating and the circular core-shell morphology illustrates that those particles are phase separated. For less acidic seed particles, the shell was thinner (pH 3) or even formed an ammonium sulfate crystal in the core observed for near neutral (pH 5) seed particles. The crystallized morphology further indicates that minimal organic material has formed (consistent with aerosol volume concentration data), as organic material interferes with crystallization leading to round amorphous solids.[269,270] SEM images were also collected to confirm the phase transition, and the result is consistent with AFM (Figure C.5). To understand the chemical composition in the individual core-shell IEPOX-derived SOA particles, PTIR and Raman spectra were collected.

Chemical composition plays an important role in understanding phase-separated inorganic-SOA mixed particles. Raman microspectroscopy and PTIR were used to identify functional group composition for the core and shell of these particles. Detailed spectra of pH 1 seed particles with NH_4^+ after IEPOX uptake for 60 min were collected (Figure 4.4), and the specific vibrational modes and full Raman spectra are listed in the Supporting Information (Table C.1). A strong sulfate peak $\nu_s(SO_4^{2-})$ at 976 cm^{-1} in the Raman spectra is clearly discernible and located in both core and shell of particles and the bisulfate $\nu_s(HSO_4^-)$ peak at 1041 cm^{-1} was also observed.[80,85,212,271] Both the particle core and shell also showed signs of organosulfate formation with peaks around 1060 cm^{-1} in the Raman spectra and 1200 in the PTIR, indicative of $\nu_s(RO{-}SO_3)$.[168] Other organic peaks were observed for both core and shell; specifically, the asymmetric carbon-hydrogen δ(C-H) of the methylene at 1460 cm^{-1},[168,272] symmetric and antisymmetric of methyl and methylene stretches were observed in the ν(C-H) region between 2800 to 3000 cm^{-1},[19,80] and carbonyl ν(C=O) at 1662 cm^{-1}. The hydroxyl ν(O-H) peak was observed at 3419 cm^{-1} from either the IEPOX uptake reaction or water from the liquid particle.[80,93] The Raman spectra of particle core and shell show that more organic compounds were formed in the

particle shell with a small amount of organics in the particle core, indicating that the gaseous IEPOX diffused through the entire inorganic particle to react and modify its physiochemical properties. Additionally, a PTIR spectrum was collected to provide complementary chemical composition information of an individual submicron particle. A strong asymmetric sulfate $\nu_{as}(SO_4^{2-})$ peak at 1108 cm^{-1} was observed,[73] and another sulfate mode at 1076 cm^{-1} was observed. The peak at 1206 cm^{-1} is assigned to bisulfate $\nu(HSO_4^-)$ group and the peak at 1422 cm^{-1} is assigned to ammonium band δ (NH_4^+).[73] The peak at 880, 914, and 1034 cm^{-1} have been identified as organosulfate group $\nu_s(RO\text{-}SO_3^-)$.

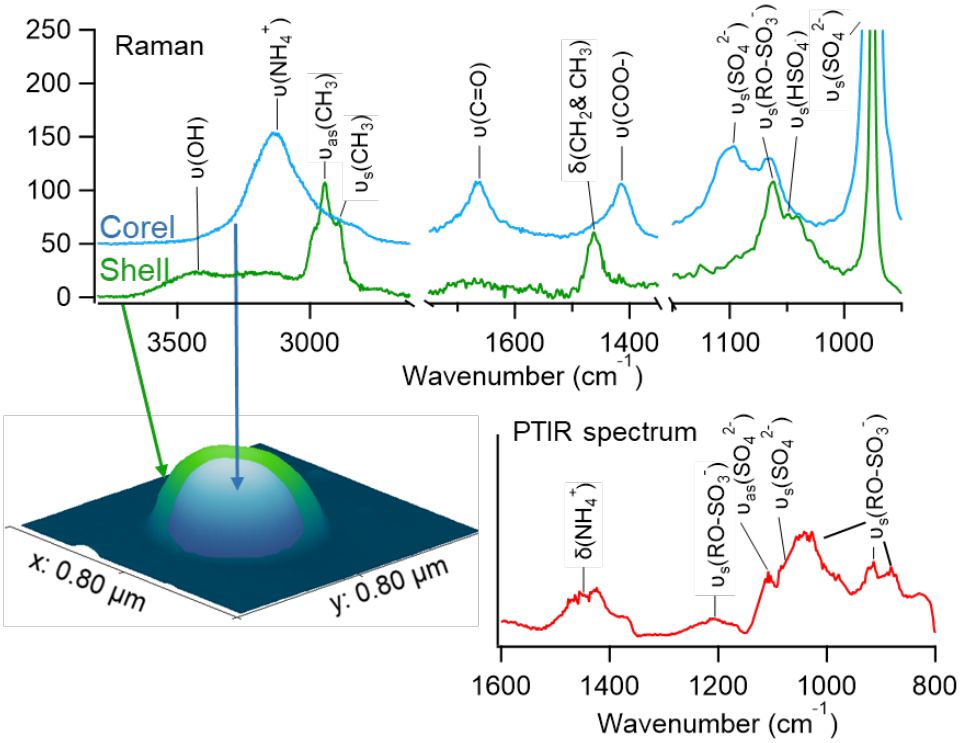

Figure 4.4 Raman spectra of pH 1 seed particles with NH_4^+ after IEPOX reactive uptake for 60 min, showing the differences between core (blue) and shell (green) composition (top), AFM 3D image of individual submicron particles after impacted on the Si substrate (bottom left); representative PTIR spectra of the whole particle for a different core-shell SOA-inorganic particle formed from IEPOX uptake.

To further understand how the pH of seed particles affects gaseous IEPOX uptake, single-particle chemical compositions were characterized using PTIR and Raman microspectroscopy. Due to particle-to-particle variance, an average of 20 PTIR spectra and 15 Raman spectra were collected for each sample, with representative spectra shown in Figure 4.5. Organosulfate formations were observed in both the PTIR and Raman spectra after different acidic seed particles

were exposed to gaseous IEPOX for 60 min. Organosulfates were identified by vibrational modes at 914, 1034, and 1206 cm^{-1}.[168] Those different organosulfate vibration modes can be either different organosulfates or different extents of their corresponding dimer, trimer, and oligomer formations, which will be probed in a future study. The reacted pH 1 seed particles with NH_4^+ formed the most organosulfates, followed by the pH 1 seed particles without NH_4^+ (Figure 4.5a and 4.5b). When the pH of the seed particles increased to 3 and 5, the formation of organosulfates decreased and more sulfate remained (Figure 4.5c and 4.5d). This result is consistent with previous studies that showed SOA formation is significantly higher under acidic conditions.[30,242] Peaks in the PTIR spectra at ~1100 cm^{-1} and 1418 cm^{-1} are assigned to asymmetric sulfate $\nu_{as}(SO_4^{2-})$ and ammonium $\delta(NH_4^+)$, respectively, with primarily $\nu_{as}(SO_4^{2-})$ present with few organosulfates at pH 3 and 5.[73]

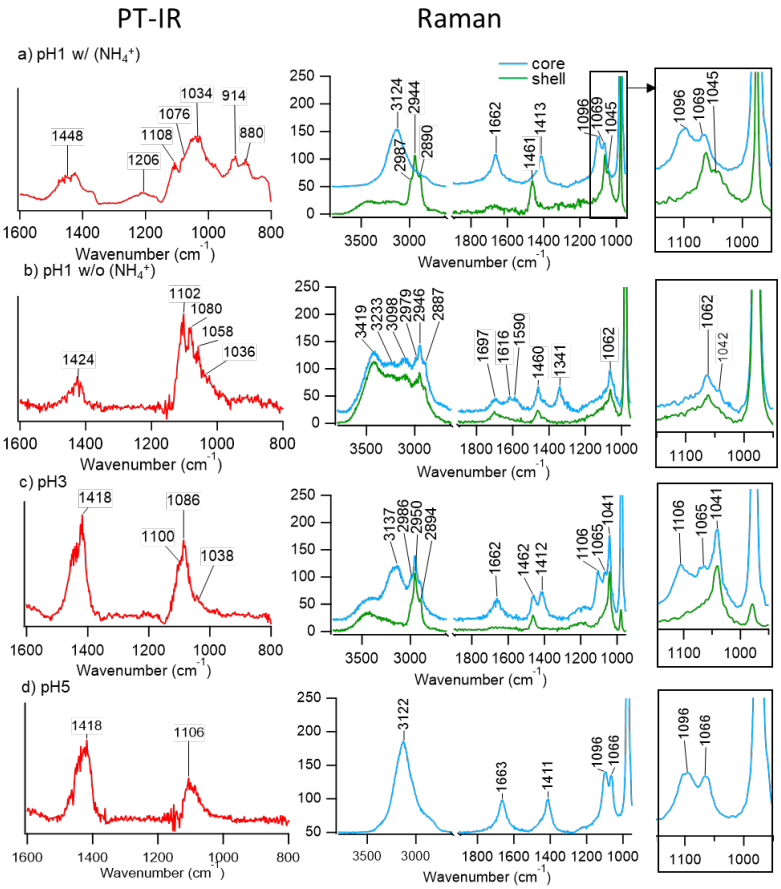

Figure 4.5 Representative PTIR spectra of individual particles after IEPOX reactive uptake for 60 minutes: a). pH 1 (NH_4^+, HSO_4^- >> SO_4^-, H^+, H_2O), b). pH 1 (HSO_4^- >> SO_4^-, H^+, H_2O) (red solid circle), c). pH 3 (NH_4^+, H^+, SO_4^{2-} >> HSO_4^-, H_2O), d). pH 5 (NH_4^+, H^+, SO_4^{2-}, H_2O) (left column). Raman spectra of four different types of SOA particles after IEPOX uptake for 60 minutes showing composition differences between core and shell (right column).

Raman spectra were collected in the particle core and shell to obtain complementary chemical information. All SOA particles formed from seed particles with different pHs showed modes indicative of organosulfate formation with peaks around 1065 cm^{-1}.[168] The distinctly different Raman spectra for particle cores and shells demonstrate chemically that phase separation occurred under acidic conditions (Figure 4.5a, 4.5b, and 4.5c). The bisulfate $\nu(HSO_4^-)$ mode was observed at 1041 cm^{-1} for all acidic seed particles with pH 1 and pH 3 after IEPOX uptake, which suggests the remaining aqueous component within particles remain acidic after exposure to IEPOX.[34,85,93] Though much smaller than the symmetric stretch in Raman, the asymmetric sulfate $\nu_{as}(SO_4^{2-})$ mode at 1096 cm^{-1} was observed for the seed particles containing ammonium sulfate.[269] Last, for pH 1 and pH 3 seed particles with NH_4^+, the $\delta(NH_4^+)$ peak around 3124 cm^{-1} was observed only in the particle core[214,215] and peaks in the ν(C-H) region between 2800 and 3000 cm^{-1} indicate organic materials were present in the particle shell. Both PTIR and Raman spectra provide complementary information regarding morphology and chemical composition after IEPOX multiphase chemical reactions.

As organosulfate formation is consistently observed in IEPOX-derived SOA particles,[175] it is important to quantify the amount of organosulfates produced for each different seed pH. Figure 4.6 shows that organosulfate formation was observed under all pH conditions, with a strong pH-dependence leading to rapid conversion of inorganic sulfate to organosulfates under the most acidic conditions (pH 1). Organosulfate formation is higher with NH_4^+ at pH 1, as the NH_4^+ may help stabilize the particle pH, preventing pH from decreasing after generation. Since pH does not decrease, less sulfate is protonated to bisulfate (below the pk_a), which is a weaker nucleophile,[273] that may slow organosulfate formation. The Raman spectra in Figure 4.5 also show more sulfate ($\nu(SO_4^{2-})$ = 1096 cm^{-1}) in pH 1 seed particles with NH_4^+ than pH 1 seed particles without NH_4^+, supporting this hypothesis. For less acidic aerosol conditions (pH 3 and 5), organosulfate production was much slower due to lower $[H^+]$ to facilitate the epoxide ring-opening reactions. This and prior experimental studies are buttressed by computational chemistry modeling that predicts IEPOX rapidly produces organosulfates in acidic aerosols.[274] The results from this study show that the most amount of inorganic sulfate was converted to organosulfates within 60 min under acidic conditions, and may indicate a self-limiting towards further IEPOX uptake at reaction times longer than 60 min.[25] For the less acidic inorganic seed particles, the maximum formation of organosulfates was observed within 80-100 min before stabilization. To further understand the

particle morphology and phase impacts on organosulfates formations, AFM phase images were collected after 30-, 60-, and 120-min reactions. Core-shell morphology was observed for each experiment across the different reaction times, with thicker shells at lower pH where greater organosulfates are seen to form in the top of Figure 6. After the formation of a thicker shell (likely more viscous) and more solid core, the amount of organosulfate formation decreased.[19,21] It should be noted that by 120 min, the SOA coating on the particles formed with the pH 1 seed particles (with NH_4^+) was so thick the core-shell morphology became difficult to resolve via phase imaging.

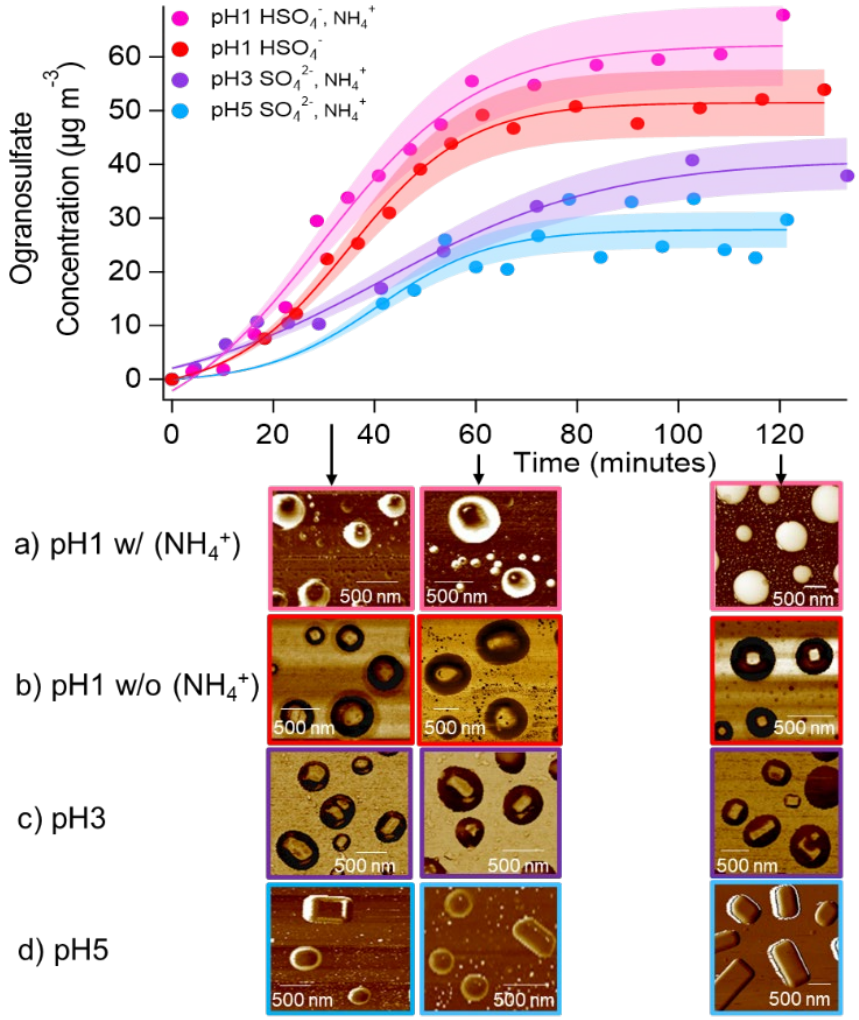

Figure 4.6 . Organosulfates concentrations by conversion of inorganic sulfate during the reactive uptake of IEPOX (top), the different color lines and shades represent sigmoid fit with uncertainties under different acidic conditions, data was corrected for wall loss; AFM phase images of seed particles with varying pH reacted with gaseous IEPOX for 30, 60, and 120 minutes. Different colors corresponding to different seed particles.

4.4 Conclusions

This study demonstrates that the initial acidity and composition of inorganic seed particles impacts their ultimate physicochemical properties (i.e., morphology and phase state) after exposure to gaseous IEPOX, which influences the continued formation, evolution, and reactivity of IEPOX-derived SOA. Phase separation was more pronounced under more acidic conditions, showing a clear core-shell morphology for individual submicron SOA particles. We further demonstrate that after reactive uptake of IEPOX on seed particles, the phase state of SOA particles shifts from a liquid phase to a semi-solid or solid phase, even at 50% RH. To further understand how acidity impacts the mechanism of organosulfates formation, future studies are needed that probe additional variables (e.g., RH and size). This study clearly demonstrates a significant modification of morphology and phase evolution during IEPOX uptake onto seed particles with varying aerosol acidities. As aerosols from a range of sources with different initial pH values can form SOA leading to complex aerosol mixing states,[32,33,149,150,275] the strong effect of acidity on IEPOX-derived SOA physical and chemical properties may have substantial implications on SOA in isoprene-rich regions.[150,276-278]

4.5 Acknowledgements

This work was supported by the National Science Foundation under Grants CHE-1654149 and AGS-1703019 (Ault), as well as AGS-1703535 (Surratt). Y.Z acknowledges support from an NSF Postdoctoral Fellowship (AGS-1524731) and the National Institutes of Health (NIH) postdoctoral training grant no. T32ES007018. A.G., Z.Z., and J.D.S. also acknowledge support from NSF Grant No. AGS-2001027 (Gold, Zhang). M.E.C. was supported by an NSF Graduate Research Fellowship (NSF-GRFP). Electron microscopy was conducted at the Michigan Center for Materials Characterization (MC^2). Atomic force microscopy was performed at the Scanning Probe Microscopy facility at the University of Michigan. The authors acknowledge initial testing on samples with Prof. Mark Banaszak Holl and Dr. Jing Zhang at Monash University.

Chapter 5. Direct Measurement of Glass Transition Temperature for Individual Submicron Atmospheric Aerosol

Ziying Lei, Jing Zhang, Emily Muller, Anne McNeil, Mark M. Banaszak Holl, Andrew P. Ault.

Analytical Chemistry Letter, 2021 (Under Review)

5.1 Introduction

Atmospheric aerosol particles play a crucial role in climate, air quality, and public health.[14] Organic matter (OM) is one of the dominant components of atmospheric aerosol particles which account for over 50% of total fine particulate matter ($PM_{2.5}$) mass.[231] Many studies have found that organic aerosol particles have effects on the atmosphere and climate through undergoing reactions with atmospheric gases,[19,25,242] interaction with water vapor and radiation, modification of their cloud condensation nuclei activities, and optical properties.[225,255] Because of the complex formation mechanism of OM in atmospheric particles and incomplete understanding of their physical and chemical properties, the extent of atmospheric particles' climate effects is highly uncertain. Additionally, submicrometer particles have great impacts on human health by depositing deeply in the alveoli and contribute to 8% of global deaths annually from air pollution.[6] A detailed characterization of particle size, chemical composition, and phase state (liquid, semi-solid, or solid) is crucial for estimating their impacts on climate and health.[162]

Traditionally, atmospheric particles were assumed to be liquid, but recent studies and evidence show that they can be semi-solid or glassy solid.[60,96] Both ambient and laboratory-generated aerosol particles have been observed to bounce off the smooth hard surface of an inertial impactor implying a non-liquid state.[59,96] Particles can have a wide range of viscosities (η) and have over many orders of magnitude difference from liquid to solid substance, such as liquid water (10^{-3} Pa s) and glass marbles ($>10^{12}$ Pa s).[58,64] Many studies have measured the bulk diffusivity in organic particles to predict the viscosity based on the Stokes-Einstein equation.[279,280] The challenge of this method is that the equation has been shown to work well for organic molecules diffusion in materials with $\eta < 10^3$ Pa s, which may underestimate the diffusivity of organic molecules in a highly viscous material by a few orders of magnitudes.[281] Some viscosity methods have been

developed in recent years; for example, Renbaum-Wolff et al. introduced a poke-and-flow technique that uses a needle to poke the particle on a substrate and monitor the time required for the material to relax back to the equilibrium state, and then viscosity can be determined by comparison with simulated flow times.[282] Furthermore, a bead-mobility technique uses melamine beads incorporated in large particles (30-50 μm) formed from an organic aerosol particle and the viscosity of the particle can be determined from the velocity of the beads.[178] Other techniques infer viscosity by including resistance to an applied force, X-ray diffraction and differential scanning calorimetry (DSC), particles coalescence in optical tweezers, and particle rebound.[283-285] These techniques provide important insights in estimating the viscosity of atmospheric aerosol particles. However, most of these methods are limited to supermicron particles, and a novel method that can measure the viscosity of individual submicron atmospheric aerosol is needed.

Glass transition temperature (T_g) has been frequently used to determine particle phase state.[58] T_g represents a non-equilibrium phase transition from a glassy solid state to a semi-solid state when the temperature increases. Different models have been improved to estimate the T_g of organic compounds, and a global chemistry-climate model can successfully predict T_g and the phase state of atmospheric aerosol particles.[39,55] The results indicate that particles are mostly liquid or semi-solid in the planetary boundary layer. To improve model predictions, a novel analytical measurement of T_g has been developed that transfers the liquid aerosol into a glassy state by low temperature evaporation of solvent.[283] This method can prevent nucleation of crystalline phases in the liquid aerosol droplets while avoiding chemical changes at room temperature, however, this is a bulk measurement that requires 2 – 5 mg of sample materials. Despite the current understanding of the viscosity and phase state of atmospheric and laboratory-generated aerosol being improved significantly, a new analytical measurement is needed to further understand submicrometer ambient particles at the single-particle level. This will have great implications in predicting the gas uptake,[19] chemical transformation of organic compounds,[57] new particle formation,[17] and particles lifetime.[281]

Atomic force microscopy coupled to photothermal infrared spectroscopy (AFM-PTIR) has recently been used to characterize the morphology and chemical compositions of individual particles down to 100 nm in diameter.[73] The addition of a thermal probe with an end radius of 20 nm adds a new capability of spatially resolved thermal analysis to the AFM, which enables the AFM to probe thermal properties at a sub – 100 nm size scale.[101] This study develops a novel T_g

measurement for individual aerosol particles using AFM thermal analysis at the nanoscale. The melting temperature (T_m) of laboratory-generated standard aerosol particles was directly measured and the T_g was determined based on the Boyer-Beaman rule. The results were compared to traditional DSC bulk measurements and the T_g model to evaluate the accuracy of this method. Particle morphology, PTIR spectra, chemical mapping, and T_m were collected to provide a detailed characterization of phase-separated particles and ambient particles for the first time. These results highlight the capability of AFM thermal analysis to analyze individual submicron particles down to 76 nm under ambient atmospheric conditions and show the power of combined AFM thermal analysis with PTIR spectroscopy to further understand physicochemical properties of atmospheric aerosol particles.

5.2 Method

5.2.1 Aerosol Generation and Impaction

Standard solutions were prepared using 18.2 MΩ Milli-Q water and the following chemicals: sucrose ($C_{12}H_{22}O_{11}$, Fisher Scientific), poly(ε-caprolactone) ($CH_3(C_6H_{10}O_2)_nCH_3$, Sigma-Aldrich), ouabain ($C_{29}H_{44}O_{12}$, Sigma-Aldrich), maltoheptaose ($C_{30}H_{52}O_{26}$, Sigma-Aldrich), raffinose ($C_{18}H_{32}O_{16}$, Grainger). All chemicals were > 95.0% purity and used without further purification. Aerosols were generated from 50 mL solutions using a Collison nebulizer operated with HEPA filtered air then passed through the diffusion driers to remove excess water and form solid particles. Particles were inertially impacted onto silicon substrate (Ted Pella Inc., product number 16013) using a microanalysis particle sampler (MPS, California Measurements Inc.), which consists of 3 stages with different aerodynamic diameter (d_a) 50% size cuts, and the particles were impacted on stage 3 (aerodynamic cut points leading to size < 0.4 μm). Submicron particles were the focus of this study as particles < 1 μm correspond to the size regime where SOA formation reactions occur. All samples were sealed before characterization.

5.2.2 Ambient Particles Sampling

Atmospheric particles were collected onto both silicon and gold substrates in Ann Arbor, MI on February 3rd, 2021 from 11:19- 13:36 EST using an MPS on stage 2 and 3 (aerodynamic diameter of 0.4 – 2.8 μm, and < 0.4 μm, respectively).

5.2.3 Differential Scanning Calorimetry Bulk Measurement

The glass transition temperature of bulk particles was measured using a modulated differential scanning calorimetry (MDSC, model Q2000, TA Instruments). Aerosol particles were atomized from 1M dilute standard solutions for sucrose, ammonium bisulfate, and raffinose. After being through two diffusion driers the dried particles were collected in an aluminum MDSC sample pan via MPS until enough mass was accumulated for a MDSC measurement (about 3-5 mg). Maltoheptaose and ouabain were directly measured from pure standards. The samples were collected at room temperature and immediately sealed before analysis.

5.2.4 Single Particle Nano Thermal Analysis Characterization

AFM with thermal analysis (Bruker, Santa Barbara, CA) was used to analyze single-component standards in contact mode. A special thermal probe that can be controllably heated was used (VITA-HE-NANOTA-200, Bruker). After the AFM image was collected, the probe was placed on the particle and the temperature of the probe increased. The deflection change of the probe was monitored during the thermal ramp. The thermal probes were calibrated each time before analyzing the sample using three polymeric calibration materials with sharp melting points, which are polycaprolactone (PCL, T_m=55 °C), high-density polyethylene (HDPE, T_m=116 °C), and polyethylene terephthalate (PET, T_m=235 °C) (Figure D.1). The calibration figure is available in Supporting Information (SI) Figure S1. The thermal probe was cleaned for each sample by raising voltage/temperature of the probe through the software control. The slower heating rate 1°C/s and the temperature range of 30–250°C was used for all the samples. At minimum, 30 particles per sample were analyzed to ensure representative and reproducible thermal analysis data.

5.2.5 Single Particle Chemical Characterization

This study used AFM with photothermal infrared spectroscopy (AFM-PTIR, nanoIR3, Bruker, Santa Barbara, CA) to characterize chemical composition of ambient particles. Particles on silicon substrates were imaged in 5 × 5 μm^2 and 10 × 10 μm^2 regions with 0.7 Hz scan rates that operated at a 0.07-0.4 N/m spring constant and 13 ± 4 kHz resonant frequency. Tapping IR mode was conducted with a gold-coated microfabricated silicon probe (AU.1000.SWTSG, Platypus Technologies). A tunable IR source (880-1950 cm^{-1} frequency range, 100 kHz repetition rate, quantum cascade laser, QCL) was used to collect PTIR spectral maps of SOA particles.

Tapping-IR mode was used, and the amplitude of cantilever oscillation was mapped using 128 co-averages, 400 pixels resolution. The IR ratio map was generated in Analysis Studio (Anasys Instruments software V3.15) to show differences in the spatial distribution of chemical components based on different vibrational modes.

5.2.6 Glass Transition Temperature Prediction

This study also included an improved parameterization for T_g prediction based on the number of carbon, hydrogen, and oxygen for organic standards. The model is based on the recent study by Shiraiwa et al.[184] using the equation shown below:

$$T_g = (n_C^0 + \ln(n_C))b_C + \ln(n_H)\, b_H + \ln(n_C)\ln(n_H)\, b_{CH} + \ln(n_O)\, b_O + \ln(n_C)\ln(n_O)\, b_{CO} \quad \textbf{Eq. 5.1}$$

where n_C^0 = 12.13 (± 2.66), b_C = 10.95 (± 13.60), b_H =-41.82 (± 14.78), and b_O = 118.96 (± 9.72), which represent the contribution of each atom to T_g, b_{CH} = 21.61(± 5.30) and b_{CO} = -24.38 (± 4.21), which are coefficients that contribute from carbon-hydrogen and carbon-oxygen bonds, respectively.

We also calculated T_g from direct T_m measurements by using the Boyer-Beaman rule that relates T_g to T_m for the sample substance.

$$T_g = g \times T_m \quad \textbf{Eq. 5.2}$$

where the glass transition temperature T_g is proportional to the melting point temperature T_m and the g = 0.7009 (± 0.004).

5.3 Results and Discussion

A schematic graph in Figure 5.1a is used to illustrate the AFM thermal analysis process of individual submicron sucrose particles. When the temperature increases, the thermal expansion of the particle causes the deflection of the probe to continuously increase until the particle starts to melt which leads to a decrease in probe deflection (Figure 5.1a). The 3D AFM images of individual sucrose particles were collected before and after the AFM thermal analysis (Figure 5.1b). After the measurement, the hole generated by the heating probe was observed and the value for T_m was obtained (92 °C). Additionally, PTIR spectra of sucrose particles were collected to provide chemical composition characterization (Figure 5.1c). IR vibrational modes observed include ν(C-

C) at 929 cm^{-1}, ν(C-O) at 997 cm^{-1}, 1055 cm^{-1} and 1111 cm^{-1}, and σ(CH_2) at 1437 cm^{-1}.[73,78,286] AFM thermal analysis combined with PTIR spectroscopy technique provides a detailed physical and chemical characterization of individual submicron particles.

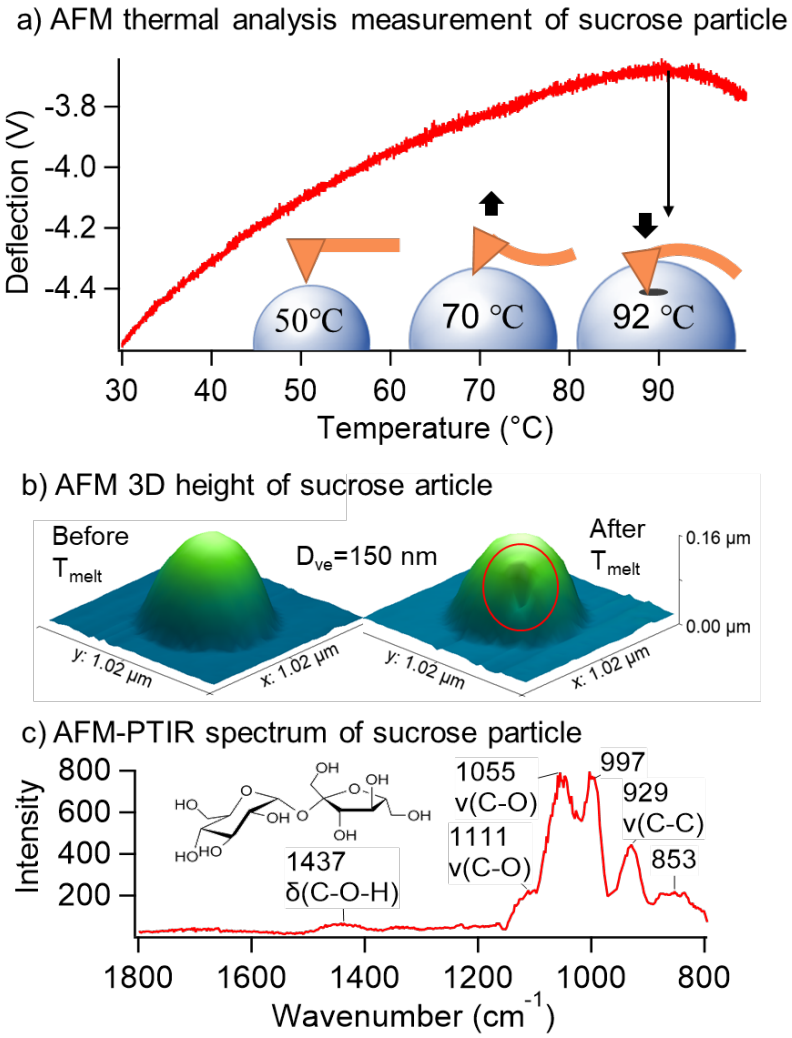

Figure 5.1 a). Schematic graph of AFM heating probe measuring individual sucrose particle melting temperature process; b). AFM 3D height image of representative submicron sucrose particle, the red circle represents the location where heating probe melted the particle; c). averaged PTIR spectrum of submicron individual sucrose particles and the sucrose molecule was made in chemdraw.

To further evaluate AFM thermal analysis, aerosol particles from single-component solutions were generated and analyzed by multiple techniques for comparison. Particles with volume equivalent diameter (D_{ve}, diameter of a sphere with volume equivalent to the impacted particle) ~ 76 – 611 nm were analyzed (Figure 5.2a), which are representative of the size range of atmospheric particles.[280] The average melting temperatures of laboratory-generated particles

(sucrose, ouabain, raffinose, and maltoheptaose) are shown in Figure 5.2b, which suggests that sucrose particles have the lowest melting temperature while maltoheptaose particles have the highest melting temperature, this result is consistent with previous studies.[58,60,287] The similar melting temperatures of ouabain and raffinose particles were observed (142 and 149 °C, respectively), which can be correlated to both compounds having a similar molecular weight (ouabain: 584 g/mol and raffinose: 594.5 g/mol). A previous study has related molecular weight to glass transition temperature (T_g) and viscosity according to the number of different C, H, and O atoms and C-H and C-O bonds in a molecular formula or the molecular weight (M).[184] Individual temperature ramps for single particles are shown in Figure D.2.

To compare AFM thermal analysis results to more traditional T_g techniques, DSC was used to collect melting temperature for those standards as well. The T_g of ouabain and raffinose particles

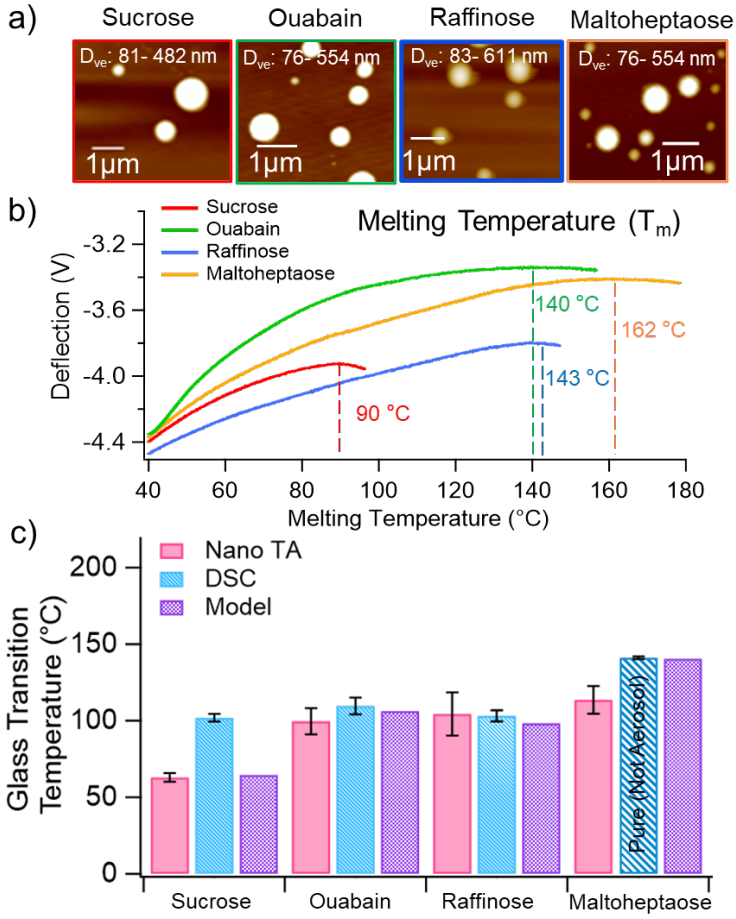

Figure 5.2. a). AFM height images of submicron sucrose, ouabain, raffinose, and maltoheptaose particles; b). Average T_m of 20 induvial particles from AFM thermal analysis measurement; c) T_g of sucrose, ouabain, raffinose, and maltoheptaose measured by AFM thermal analysis, DSC, and model calculation. The maltoheptaose from pure standard was directly measured.

measured by AFM thermal analysis is consistent with DSC measurement. The higher T_g of sucrose particles measured by DSC was observed, which may be due to the different morphologies presented in different methods (crystal vs. sphere).[288] Additionally, the minimum mass of sample for DSC measurement is 3 mg, the particles that were accumulated in the DSC pan could cause the water molecule to be trapped before the sucrose recrystallized, which can modify the sample composition and subsequently affect the T_g result.[289] For maltoheptaose, the pure standard was used directly for DSC measurement to ensure the sample has enough mass without further dilution, which can lead to the slight difference in T_g results from AFM thermal analysis that measured individual submicron particles generated from solution. The agreement of different measurements and the T_g model provide robust evidence for the ability of AFM thermal analysis to study T_g of individual submicron particles.

In the atmosphere, particles are frequently not homogeneous and have more complex morphologies (i.e., core-shell). In order to examine capabilities for multi-component particles with core-shell morphology, particles with an ammonium sulfate core and polyethylene glycol (PEG) shell were analyzed. The AFM height image showed the individual particles with D_{ve} 80 – 300 nm (Figure 5.3a). To confirm the chemical compositions are different for the particle core and shell, the PTIR spectra were collected in the middle and the edge of the particle to represent the particle core and shell shown in Figure D.3. The peak at 1400 cm^{-1} was only observed in the particle core,

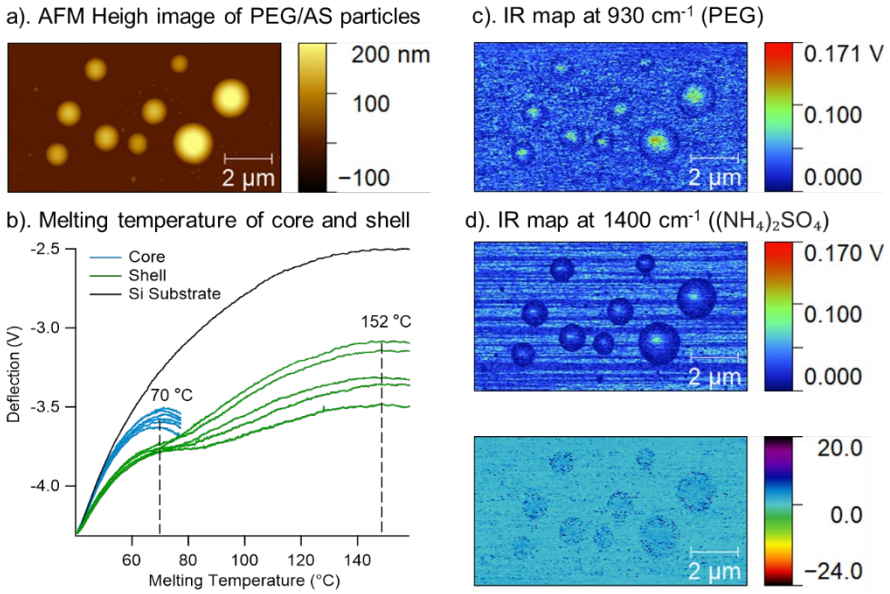

Figure 5.3 a). AFM height images of PEG/AS phase-separated particles; b). Melting temperature ramps of particle core and shell; c) IR spectral map at 930 cm^{-1}; d) IR spectral map at 1400 cm^{-1}; e) the ratio of 930/1400 cm^{-1}

which is assigned to $\delta(NH_4^+)$ from ammonium sulfate.[73] The temperature ramps were collected from the particle core and shell to show different melting points based on the two distinct compositions (Figure 5.3b). The thermal probe couldn't penetrate the organic shell in the middle of the particle to reach the core and the T_m of PEG at 70°C was observed. At the edge of the particle, the thermal probe melted the shell and reached the silicon substrate. The single wavenumber PTIR mappings were collected for the mode at 930 cm^{-1} from PEG and the mode at 1400 cm^{-1} from ammonium sulfate, which show different spatial distributions (Figure 5.3c-e). The ratio map (Figure 5.3e) most clearly highlights differences in spatial distribution, which illustrates that the small ammonium sulfate core was coated by a thick PEG shell.

To provide more detailed AFM Nano TA analysis within an individual particle, a line scan was performed and temperature ramps every 0.3 µm across a phase-separated particle were collected (**Figure 4a**). The holes caused by the AFM heating probe after the line scan are shown in **Figure 4c**. The T_m at each point in the line scan demonstrates that the thermal probe can measure T_g of minimum PEG on the edge of the particle with 146 nm thickness (**Figure 4c**). These results

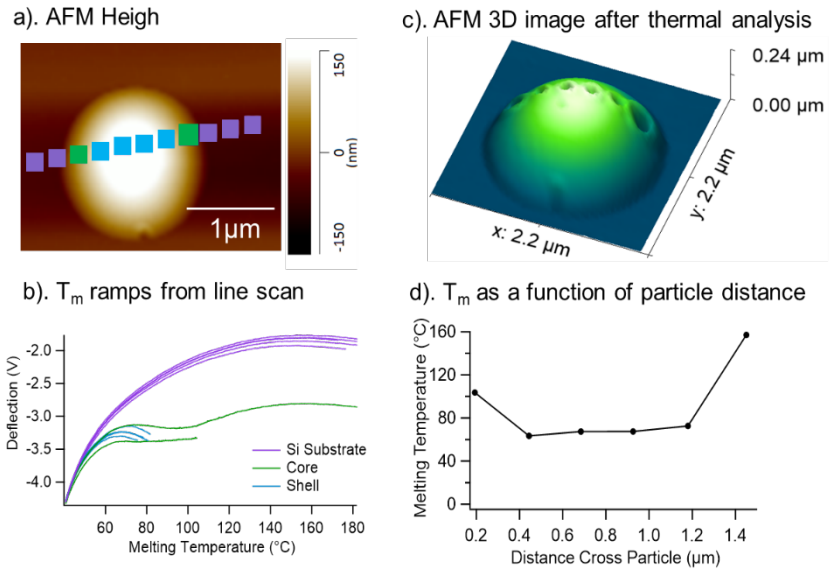

Figure 5.4 a). AFM height images of PEG/AS particles with line scan, each markers represent the location of T_m ramp were collected, the different colors represent the particle core (blue), shell (green), and substrate (purple); b). Individual T_m ramps of line scan correspond to a); c) AFM 3D image after thermal analysis; d) T_m as a function of particle distance.

provide evidence that AFM thermal analysis can measure T_g within individual particles related to particle morphology, which can be used to reveal aerosol viscosity and study the mixing state.

To further explore the AFM thermal analysis technique, ambient particles were collected and analyzed for the first time. Core-shell morphology of ambient particles was observed (Figure 5.5a), both temperature ramps and PTIR spectra were collected to determine T_g of particles and understand their chemical compositions (Figure 5.5b and c). Two distinct T_m for particle core and shell were observed for ambient particles where the shell has a relatively lower T_m at 80 °C and the T_m for particle core is 120 °C (Figure 5.5c). This result illustrates that the organic shell is more likely to be in the liquid or semi-solid phase and the core is more likely to be in a solid phase. The modes at 1104 and 1412 cm^{-1} in the particle core represent ν_s (SO_4^{2-}) and $\delta(NH_4^+)$,[73] respectively, indicative of ammonium sulfate. Other modes at 1336, and 1732 cm^{-1} identified as δ(C-H) and ν(C=O), respectively,[78] which suggest that the particles also contained organics in the shell. The combined T_g measurement and chemical information on the submicron particles show that the detailed physicochemical characterization can be obtained from individual ambient particles and

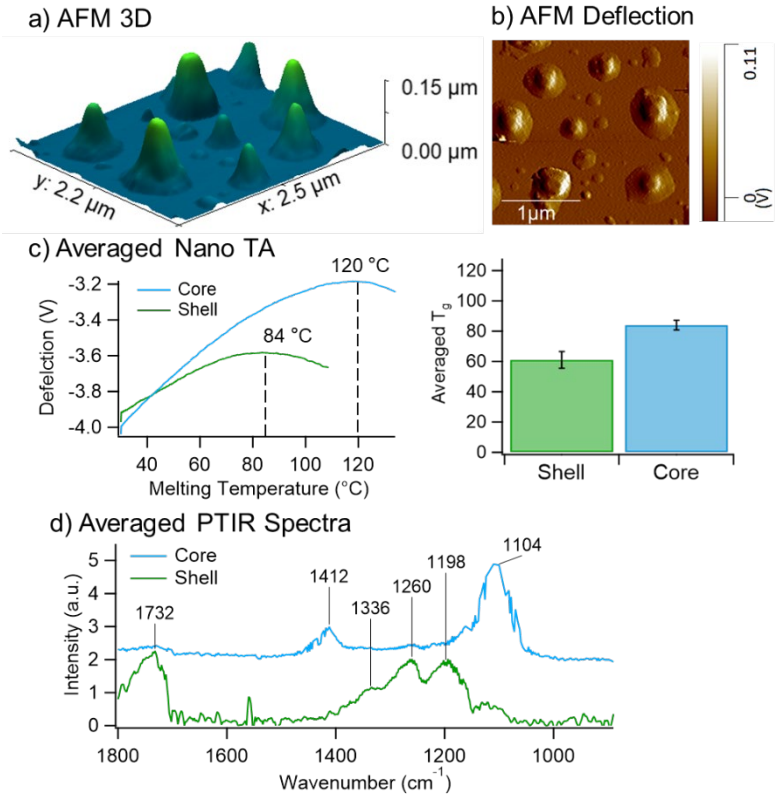

Figure 5.5 a). AFM 3D image of ambient particles; b). AFM deflection image, c). Averaged T_m ramp for particle core (blue) and shell (green); d). Averaged AFM-PTIR spectra of particle core (blue) and shell (green).

that this method can be applied to study the phase state of atmospheric particles containing complex mixtures of chemical species.

5.4 Conclusion

This study has demonstrated the new application of AFM thermal analysis on nanoscale particles and was applied to study single-component model systems, phase-separated particles, and ambient aerosol particles for the first time. The particle size, morphology, phase, chemical composition, and melting temperature can all be obtained. The novel application of this analytical method to atmospheric particles enabled the determination of T_g for the submicron individual particles, as well as identified the chemical compositions of phase-separated components within a particle size range that has not been studied previously. The high spatial scale analysis of T_m and chemical mapping within particles demonstrate the ability of this analytical technique to determine the intraparticle T_m difference caused by the distribution of chemical species, which impact the aerosol physicochemical properties in the atmosphere. Future work will be focused on understanding T_m of individual submicron particles changes as a function of RH and temperature. Different types of SOA particles with varying O: C ratios can be probed to further understand the particle viscosity and phase state, which will provide key insights regarding physicochemical properties of atmospheric particles in a critical size range for climate and human health.

5.5 Acknowledgments

The authors acknowledge funding by the National Science Foundation through CAREER award CHE-1654149, Atomic force microscopy was performed at the Scanning Probe Microscopy facility in the Department of Chemistry at the University of Michigan.

Chapter 6. Conclusion and Future Directions

6.1 Conclusion

Atmospheric aerosol has significant impacts on climate and human health, therefore understanding the chemical and physical properties of individual submicron particles is critical to reducing uncertainties in climate change and improving air quality. Although recent progress has been made, due to the complex nature of atmospheric aerosol, novel techniques and measurements are needed to provide more detailed physicochemical characterization. This dissertation focuses on the development and use of state-of-the-art instruments to characterize the physicochemical properties (i.e., acidity, morphology, size, viscosity) of laboratory-generated and ambient particles. The novel methods developed in this dissertation address some challenges of measuring the physicochemical properties of atmospheric aerosols. The application of these methods to study atmospheric aerosol provides insight into the complex chemical composition and reaction mechanisms of multiphase processes in the atmosphere. The findings from this dissertation improve the current understanding of aerosol impacts on climate and health, which further motivates future studies.

Chapter 2 developed a novel acidity measurement method for individual submicron aerosol particles using a pH-sensitive polymer, poly(ε-caprolactone). Acidic aerosol particles with pH 0 were deposited on a polymer thin film (21-25 nm), which was then incubated in a sealed humidity chamber at 50% RH for up to 15 days. Acidic aerosol particles were rinsed from the polymer film, so that the degradation thickness could be characterized by AFM and Raman microspectroscopy. The results suggest that the polymer degradation thickness is a function of time; the longer the particles stayed on the polymer, the larger the polymer degradation. As particle size decreased, polymer degradation thickness increased, indicating an increase in aerosol acidity at smaller particle diameters. This method presents the potential of studying submicron individual aerosol particles without constraints on complex chemical compositions and relative humidity.

Chapter 3 studied the morphology and viscosity of size-selected submicron SOA particles formed from oxidation of four different VOC precursors (α-pinene, β-caryophyllene, isoprene, and toluene) before and after exposure to IEPOX for two hours. The physicochemical properties and chemical composition of individual particles were characterized using AFM-PTIR, Raman microspectroscopy, and SEM-EDX. The changes in viscosity and morphology were observed after IEPOX reactive uptake, and the results demonstrate that the modification of SOA physicochemical properties is highly dependent on their VOC precursors. Specifically, the viscosities of α-pinene and β-caryophyllene SOA decreased significantly after IEPOX uptake, while the viscosities of isoprene and toluene SOA did not appreciably change. Additionally, the phase separation and more particles with complex structure were observed at larger particle size after IEPOX uptake, suggesting that particle size could play an important role in morphology and heterogeneous reactions. The findings from this study increase our understanding of the impacts of multiphase chemical reactions and can improve predictions of SOA formation.

Chapter 4 investigated morphology, phase state, and chemical composition of individual organic-inorganic particles with different initial acidities (pH = 1, 3, and 5) after IEPOX uptake using AFM-PTIR and Raman microspectroscopy. Enhanced IEPOX reactive uptake to the most acidic seed particles (pH = 1) resulted in 23% more formation of organosulfates compared to less acidic seed particles (pH 3 and 5). Distinct phase separations (i.e., core-shell morphologies) primarily occurred for initial pH values < 3. Increased aerosol acidity (lower pH) also led to more viscous organic components of SOA particles and more irregularly shaped morphologies as the organic phase transitioned to semi-solid or solid. Conversion of inorganic sulfate to organosulfates corresponded with the transition to the higher viscosity of the organic phase and more complex structures. This study highlights that aerosol acidity controls key multiphase chemical reactions and the subsequent modification of aerosol physicochemical properties, such as viscosity and morphology, which can be used to improve predictions of SOA formation, as well as subsequent climate and health impacts.

Chapter 5 applied a new microspectroscopic technique, AFM thermal analysis, to measure the glass transition temperature of individual submicron atmospheric aerosol particles for the first time. An AFM heating tip sits on the top of the particle and the melting temperature will be detected when the particle melts. This method was validated by analyzing different standard laboratory-generated aerosol particles and comparing the result to DSC measurement and model

predictions. Ambient particles were collected in Ann Arbor that are complex mixtures of organic and inorganic materials, and the melting temperature was measured for the core and shell of phase-separated particles. This unique measurement provides new fundamental molecular insight into the viscosity of atmospheric aerosol that has important implications for the climate and health.

6.2 Future Directions

The research described in this dissertation provides insight into detailed physicochemical characterizations of atmospherically relevant aerosol particles using advanced microspectroscopic methods. The novel methods developed in the research chapters address the challenge of measuring the acidity and viscosity of individual submicron aerosol particles. However, further work can be performed to improve those methods and apply them to understand more about the physicochemical properties of ambient aerosol particles and optimize current model systems.

In Chapter 2, a novel pH measurement was developed to understand the acidity of individual submicron aerosol particles using a thin degradable polymer. This study demonstrates its potential for determining whether individual submicron particles are acidic without some of the limitations of bulk pH measurements. However, different atmospherically relevant pH values between 0 and 6 need to be investigated to better understand the acidity of atmospheric aerosol particles for future sensor development. Additionally, due to the complex nature of aerosol particles under atmospheric conditions, other factors (i.e., RH and temperature) that can influence aerosol acidity need to be considered in future studies. The effect of RH and a systematic range of particle size (100 – 800 nm) need to be examined to understand why the smaller particles are more acidic. In this study, the thinnest polymer with 25 nm thickness was used that was completely degraded by pH 0 acidic particles for up to 15 days. To establish a pH measurement system using polymer degradation rate and thickness, a more sensitive and precise polymer will need to be tested to measure ambient particles in regions with different VOC precursors.

In Chapter 3, the impacts of multiphase chemical reactions on physicochemical properties of different types of SOA particles were studied using multiple microscopic and spectroscopic techniques. Although different oxidized organic coatings were investigated, many different factors can affect heterogeneous reactions, such as different acidity of ammonium bisulfate seed particles, RH conditions, and types of seed particles (e.g., sodium sulfate). This study shows that the significant decrease in viscosities of α-pinene and β-caryophyllene SOA particle after IEPOX

uptake is attributed to the formation of lower molecular weight, but future work needs to identify specific species and functional groups to further characterize this change. The additional mechanism study using online mass spectrometry will help to explain the chemical composition change in those multiphase reactions. The SOA particles with 150, 200, 250, and 300 nm diameters were examined, and the results suggest that the changes in morphology and viscosity of different SOA particles are dependent on particle sizes, however, a wider range of particles size (i.e., 100 – 800 nm) needs to be studied in the future. A more quantitative analysis of particle viscosity is needed for future studies to further assess the extent to which viscosity impacts multiphase reactions and aerosol climate properties.

In Chapter 4, the impacts of inorganic seed particle acidity (pH 1, 3, and 5) on reactive uptake of gaseous species and on aerosol physicochemical properties were studied. The ammonium bisulfate seed particles and different pH values were chosen are based on the abundance of ammonium bisulfate particles in the atmosphere and atmospherically-relevant pH values; however, the other pH values (i.e., pH 0, 2, 4, and 6) and types of inorganic seed particles (i.e., sodium sulfate) need to be considered in the future studies. Recently, a new technique, O-PTIR, was applied to study atmospheric aerosol particles and it can collect both Raman and PTIR spectra at the same location on individual particles, and PTIR mapping can be used to visualize the spatial distribution of chemical species[78]. This novel technique can be used for future studies to provide more detailed chemical characterization for complex SOA particles. Though this study demonstrates that acidic seed particles lead to a significant increase in organosulfate formation, to further understand how acidity impacts the mechanism of organosulfate and SOA formation, future studies are needed that probe other variables (e.g., RH and size).

In Chapter 5, AFM-PTIR with thermal analysis were applied for the first time on atmospheric aerosol particles to directly measure the melting temperature of submicron individual particles. This study shows that this novel method can improve the current understanding of individual particle viscosity under atmospheric conditions. Further work is needed to systematically study the viscosity as a function of RH and particle size at a single-particle level, and the particles with complex chemical compositions and morphologies (e.g., core-shell SOA particles) can be investigated. Furthermore, thermal mapping combined with chemical mapping of individual particles can be collected in future studies to further understand the functional group distribution that leads to the viscosity change. The characterization of ambient particles is needed

to examine aerosol particles from different sources and different regions, which can provide insight for atmospheric models.

This dissertation sought to address the current challenge of measuring aerosol physical properties, as well as to improve our understanding of the physicochemical properties of submicron individual SOA particles. Although work remains to fully characterize the physicochemical properties of atmospheric aerosols, many advancements have been made throughout this dissertation. The novel acidity and glass transition temperature measurements provide insight into physicochemical properties of submicron aerosol particles at single-particle level. The detailed physical and chemical characterization of SOA help to further understand the key atmospheric reactions and physical processes. The future directions listed above will improve the accuracy of the current model system to predict the aerosol formation and climate impacts on a global scale.

Appendices

Appendix A. Aerosol Acidity Sensing via Polymer Degradation Supplemental Information[1]

A.1 Raman spectra of pH 0 acidic particles under different RH conditions

To ensure the pH 0 particles were aqueous while interacting with the polymer, Raman microspectroscopy was used to investigate particle composition under different RH conditions varying from 10% - 90%. pH 0 acidic particles were generated under wet condition with 90% RH and impacted on silicon substrate. The sample was placed in a sealed chamber to maintain the high relative humidity when the Raman spectra were collected. The intensity of the O-H stretching region, ν(O-H) at 3435 cm^{-1}, correlated with increasing the RH.

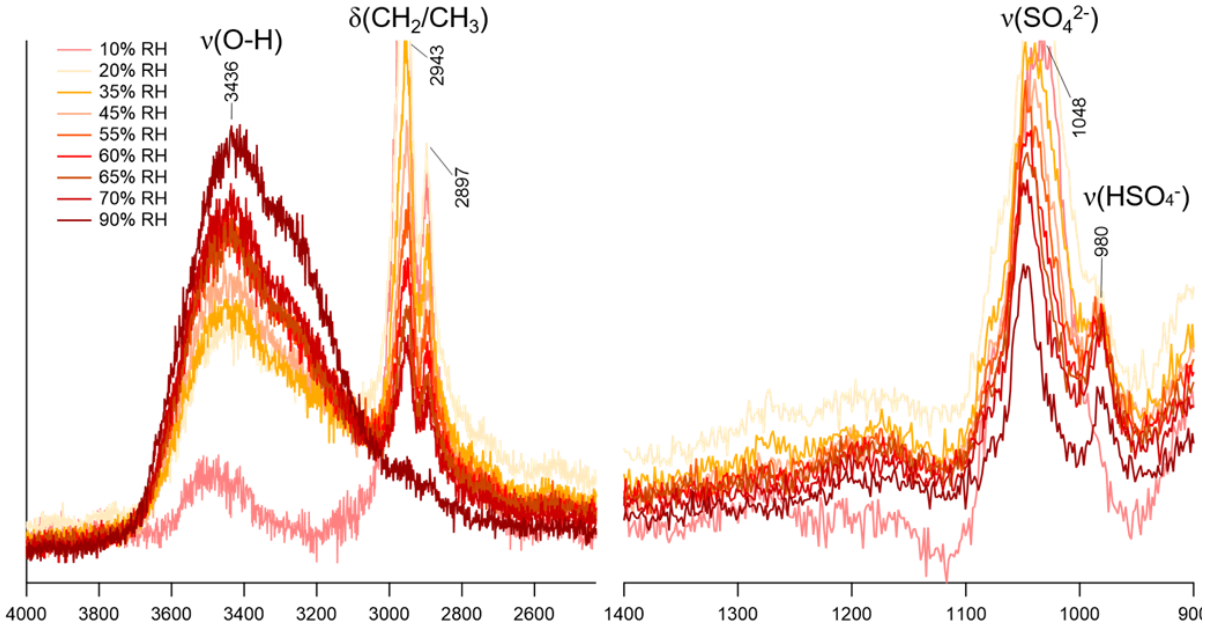

Figure A.1 Raman spectra of sulfuric acid particles with pH 0 under different RH. Each color corresponds to a Raman spectrum of sulfuric acid particles under different RH condition.

[1] Appendix A details supplemental information corresponding to Chapter 2

A.2 SEM images of PCL after rinsing off neutral particles and acidic particle

SEM analysis of PCL was performed by a FEI Helios 650 Nanolab-Dualbeam electron microscope equipped with using an Everhart-Thornley secondary electron detector that operated at an accelerating voltage of 10.0 kV and a current of 0.80 nA under vacuum conditions (10^{-3} to 10^{-5} Pa). SEM images of PCL were obtained orthogonal to the beam and at a 45-degree angle (tilted).

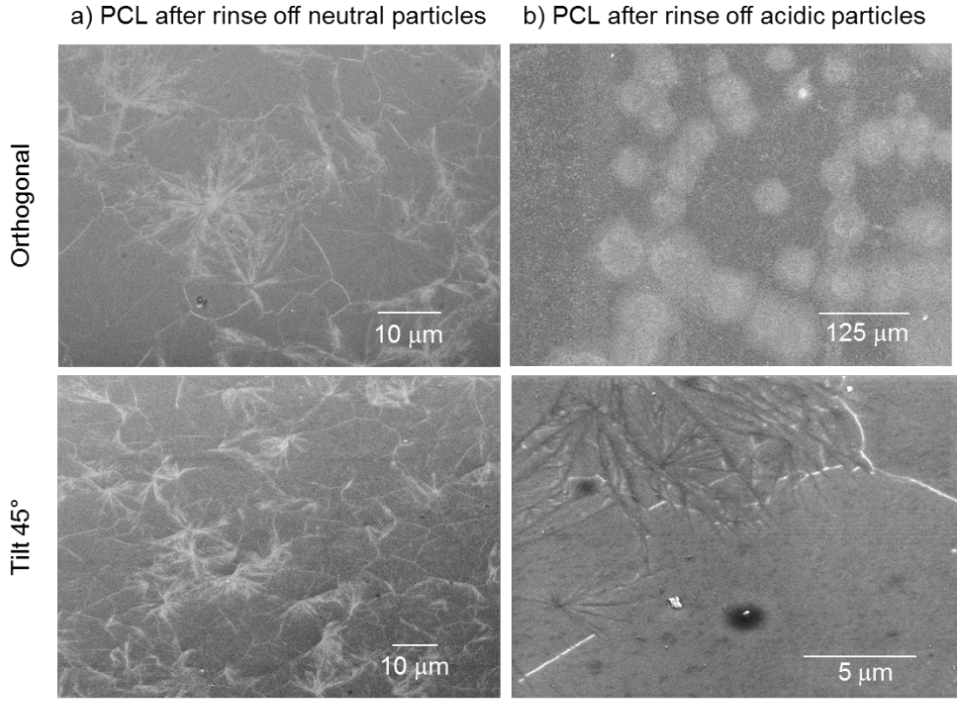

Figure A.2 SEM images of PCL a) after ammonium sulfate pH 6 particles that had been impacted on PCL were rinsed off after 15 days; b) after sulfuric acid pH 0 particles that had been impacted on the PCL were rinsed off after 15 days. Top images are orthogonal to the beam, while the bottom images are at 45 degree tilt.

A.3 AFM height image showing the degradation of PCL thin film

After acidic particles were rinsed off after impaction on the PCL thin film for 15 days, distinct, clear holes were observed, which demonstrate the degradation of PCL caused by acidic particles.

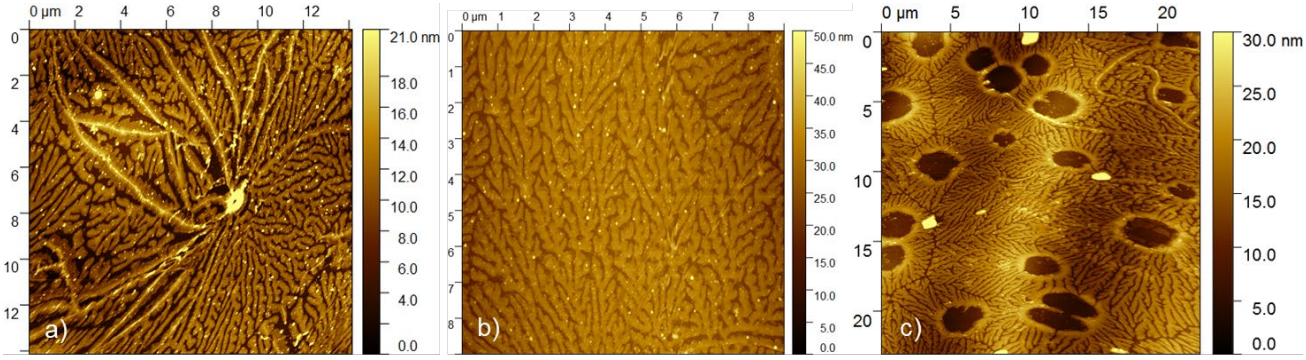

Figure A.3 a). 14 µm × 14 µm AFM height image of non-degraded PCL; b) 9 µm × 9 µm AFM height image of PCL film following exposure to ammonium bisulfate pH = 6 particles for 15 days; c) 25 µm × 25 µm AFM height image of PCL film following impaction and rinse off (15 days) of acidic pH = 0 particles. The bright spots are AFM tip artifacts

A.4 Root mean squared (RMS) roughness equation

The root mean squared (RMS) roughness of the initial PCL was 2 nm. This was calculated from 10 μm^2 AFM height images using Gwyddion according to the definition of RMS roughness:

$$R_q = \sqrt{\frac{1}{n}\sum_{i=1}^{n} {y_i}^2} \quad \textbf{Eq. A.1}$$

Where n is spaced points along the trace, and y_i is the vertical distance from the mean line to the i^{th} data point.[290] This was independently confirmed with the Nanoscope software.

The spreading ratios of particles on these surfaces are similar to those reported for particles impacted on silicon wafers,[19,73,168] suggesting that this low level of surface roughness does not affect particle deposition or surface wetting.

A.4 Raman spectra of PCL degradation process

Raman spectra were collected at three points during degradation process: non-degraded PCL film; PCL film before wash particle off; and PCL film after wash particle off. A clear sulfate peak at 978 cm^{-1} was observed before sulfuric acid particle wash off, confirming the particle chemical composition. The mode is at the same frequencies as a mode intrinsic to the silicon, making the intensity in this region much greater that of other peaks in Figure 3 of the manuscript, though the sulfate peak is clearly visible on top.

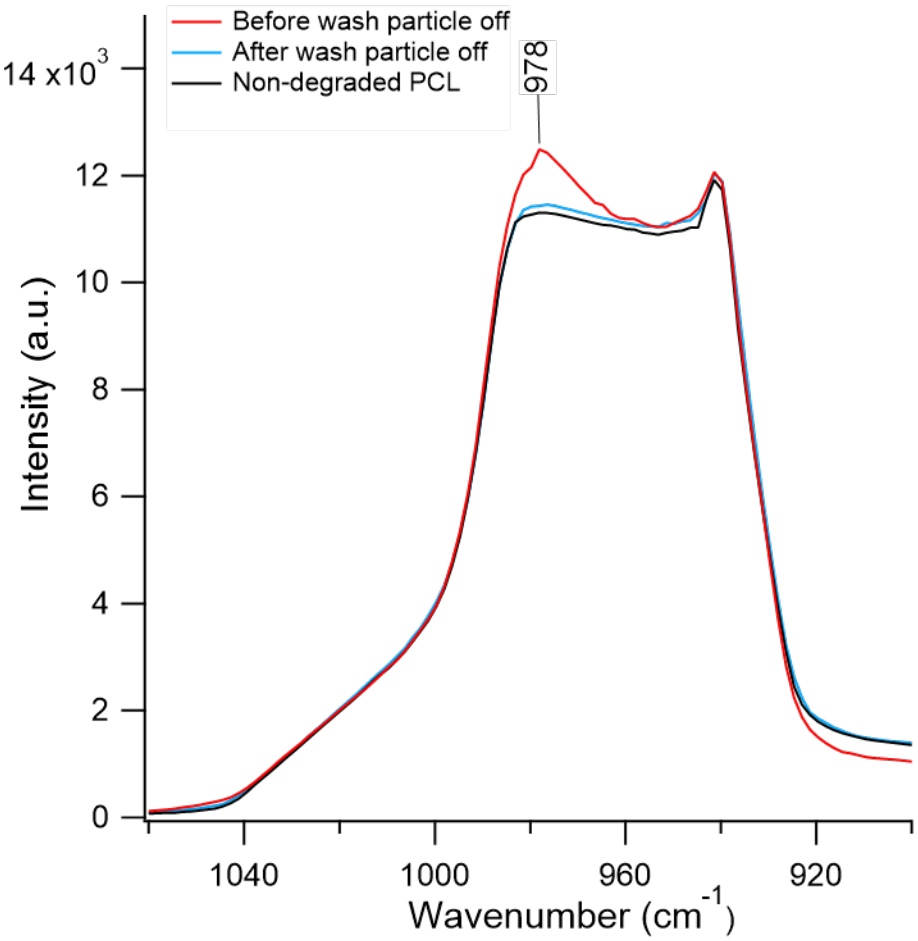

Figure A.4 Raman spectra of non-degraded PCL film background (black), PCL film with pH 0 acidic particles for 15 days (red), PCL film after all particles were rinsed off (blue).

A.5 Raman spectra of non-degraded PCL

To charactrize and confirm the chemical composition of the PCL film, Raman spectra of a non-degraded PCL film were collected at different locations on the PCL film. The spectra are consistent with the main peaks observed corresponding to modes in the C-H stretching region (symmetric elongation of methylene groups $\delta(CH_2\text{-})$ at 2865 cm^{-1} and 2914 cm^{-1}, respectively), the $\delta(CH_2)$ mode at 1440 cm^{-1}, and the carbonyl group $\nu(C{=}O)$ at 1723 cm^{-1}, and multiple modes in the C-H stretching region ($\nu(C\text{-}H)$).[73,80,171]

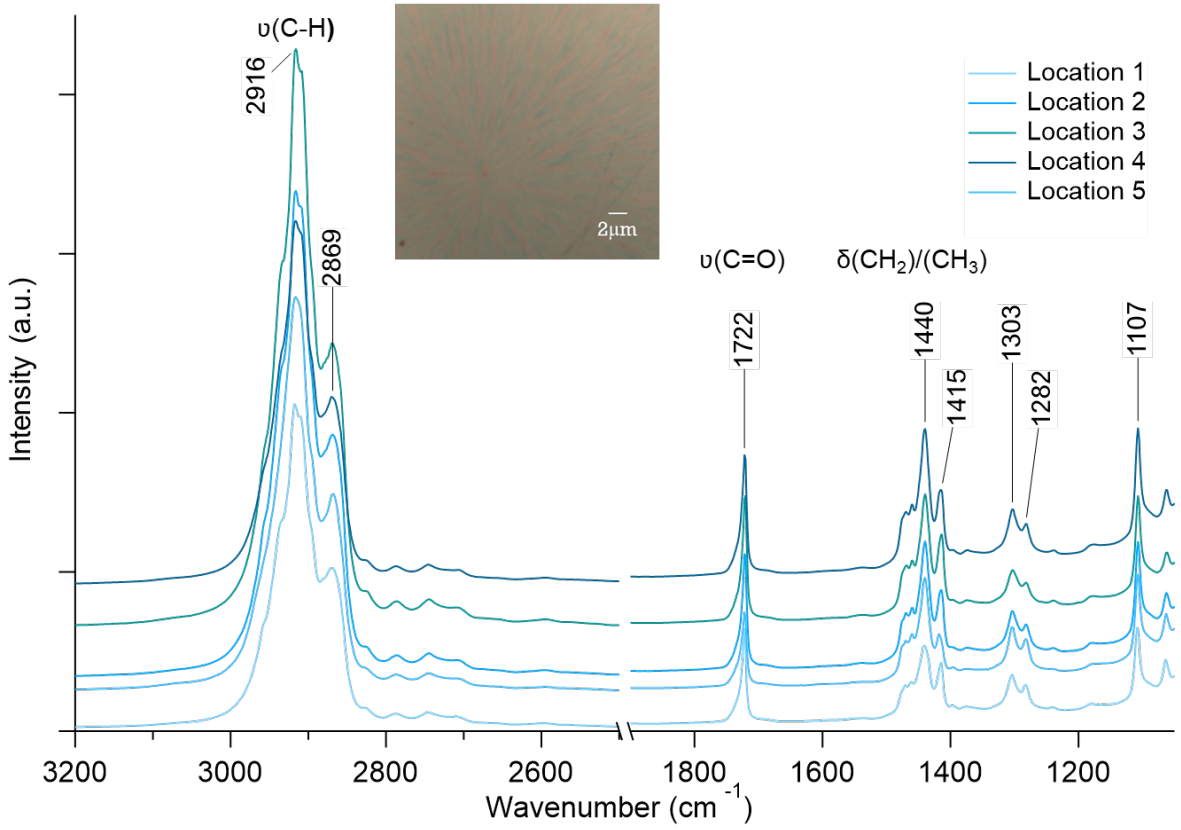

Figure A.5 Raman spectra and optical image of 400 nm thick non-degraded PCL film; the colors represent individual Raman spectra collected at different points spatially on a single PCL film.

A.6 AFM-IR spectra of non-degraded PCL

AFM image and PTIR spectra of a non-degraded PCL film were collected, and the result is consistent with the Raman spectra. The main IR peaks are: the ν(C-H) stretching region at 2852 – 2956 cm^{-1}, ν(C=O) mode at 1728 cm^{-1}, and δ(C-H) of the methylene groups at 1364 cm^{-1}.[73]

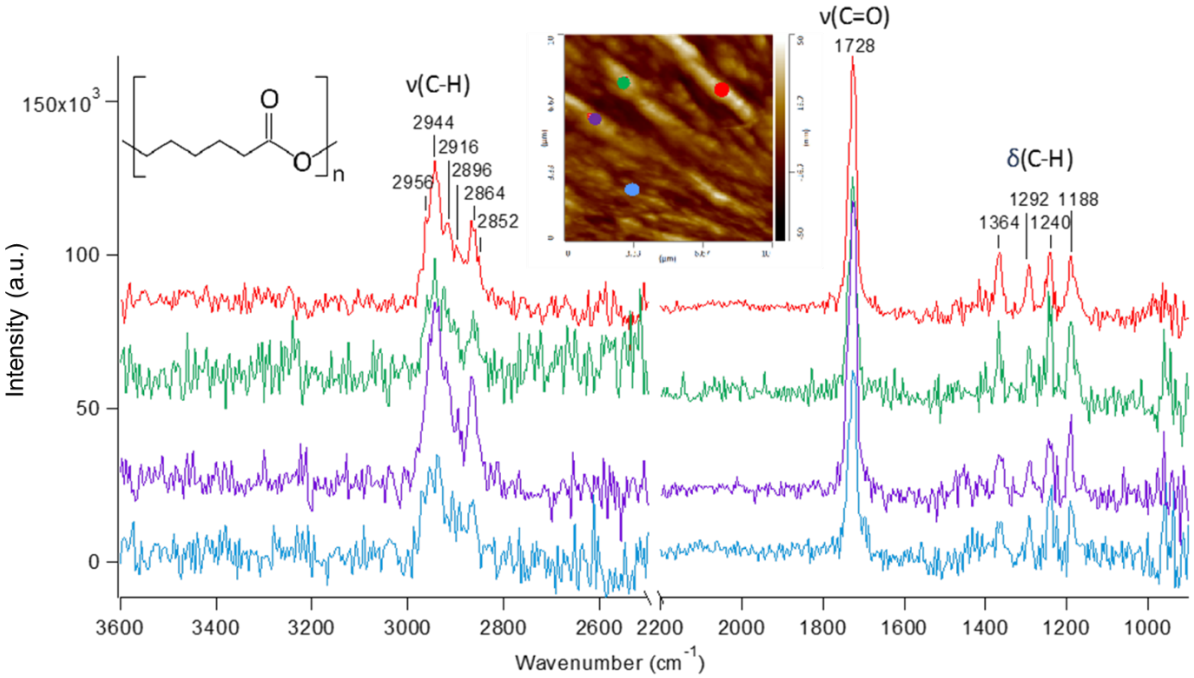

Figure A.6 AFM-IR spectra of 400 nm thick initial non-degraded PCL film; colors indicate the location at which each spectrum was acquired. The four spectra from different locations on the PCL film are consistent.

A.7 Numbers of individual particles characterized in Figure 2.4 and Figure 2.5

Table A.1 Numbers of individual particles were examined

Number of individual particles were characterized			
Figure 4	**3 days**	**7 days**	**15 days**
	46	**41**	**40**
Figure 5	**320-560 nm**	**180-320 nm**	**<180 nm**
	27	**34**	**29**

A.8 pH indicator paper measurement of acidic aerosol particles with varying sizes

The pH values of aerosol particles generated from the pH 0 sulfuric acid bulk solution were confirmed using colorimetric pH measurements.[147] The particles were collected on stages 6, 7 and 8 with size ranges of 320-560 nm, 180-320 nm, and < 180 nm, respectively, of the mini-MOUDI on pH indicator paper. The image of the pH indicator strip for each sample was taken immediately and analyzed with a custom MATLAB script based on the pH color scale.[147]

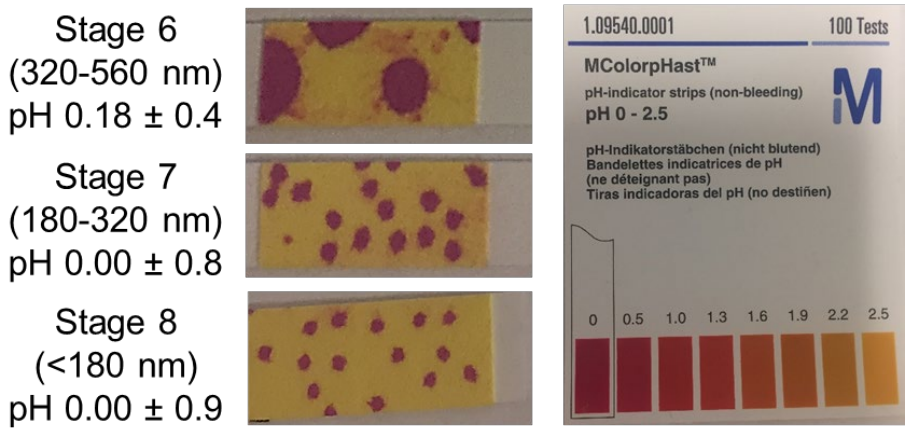

Figure A.7 Sulfuric acid (pH = 0) aerosol particles were generated and impacted on pH indicator paper by mini-MOUDI on stage 6, 7, and 8 with aerodynamic diameter size cuts of 320-560 nm, 180-320 nm and < 180 nm, respectively.

Appendix B. Morphology and Viscosity Change after Reactive Uptake Isoprene Epoxydiols in Submicrometer Phase Separated Particles with Secondary Organic Aerosol Formed from Different Volatile Organic Compounds Supplemental Information[2]

B.1 Size Distribution of Four Types of SOA

The size distribution of four types of SOA were collected using a scanning electrical mobility spectrometer (SEMS, BMI Inc., Model 2100) to ensure the inorganic sulfate particles were coated uniformly, and to monitor the particle growth after IEPOX uptake. Based on the size distribution of the four SOA types after IEPOX uptake, 150, 200, and 250 nm inorganic-SOA mixed particles were investigated in this study.

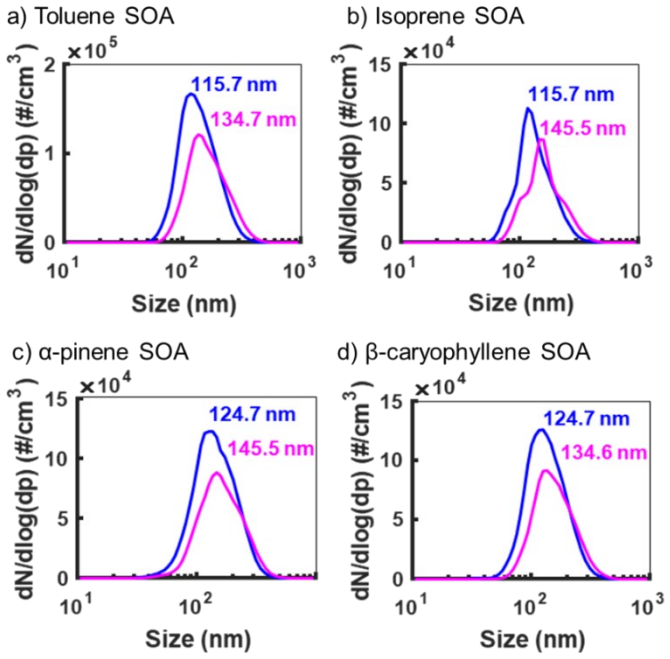

Figure B.1 Size distribution plots of a) toluene SOA; b) isoprene SOA; c) *α*-pinene SOA; d) *β*-caryophyllene SOA. Blue lines represent the size distribution of SOA-coated inorganic sulfate particles, and the pink lines represent the size distribution of SOA-coated inorganic sulfate particles after IEPOX uptake.

[2] Appendix B details supplemental information corresponding to Chapter 3

B.2 Experimental Details

The inorganic seed particles were generated by atomizing $(NH_4)_2HSO_4$ and passed through a diffusion drier that lowers the relative humidity (RH), but above efflorescence RH (30%).[291] Particles with an electrical mobility diameter of 100 nm were selected by differential mobility analyzer (DMA) and entered the potential aerosol mass (PAM) reactor to coat inorganic seed particles with SOA coatings generated from the oxidation of either toluene, isoprene, α-pinene, or *β*-caryophyllene. The charcoal denuders and an O_3 scrubber were used to remove excess VOCs and O_3 before entering the UNC indoor chamber facility. A scanning mobility particle sizer (SMPS) was used to ensure particles were coated with SOA before entering the indoor chamber. After injection of SOA-coated inorganic seed particles, the chamber was left static to ensure the particles were uniformly mixed. Then gaseous *trans*-□-IEPOX was injected into the chamber. Particles with 150 nm diameter were collected before IEPOX uptake, and 150, 200 and 250 nm particles were collected after IEPOX uptake using a microanalysis particle sampler (MPS).

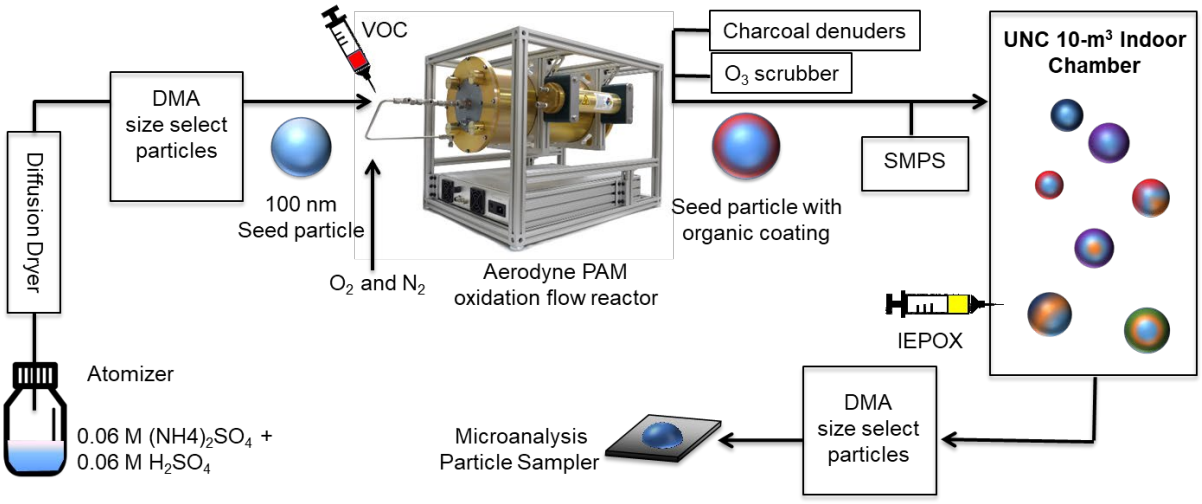

Figure B.2 Experimental design showing instrumental setup and SOA formation.

B.3 AFM Phase Images of Four Types of SOA Particles Before and After IEPOX Uptake

The larger size of AFM phase images shows the morphology and phase of 150 nm α-pinene SOA-, β-caryophyllene SOA-, isoprene SOA-, and toluene SOA-coated sulfate particles before and after IEPOX reactive uptake.

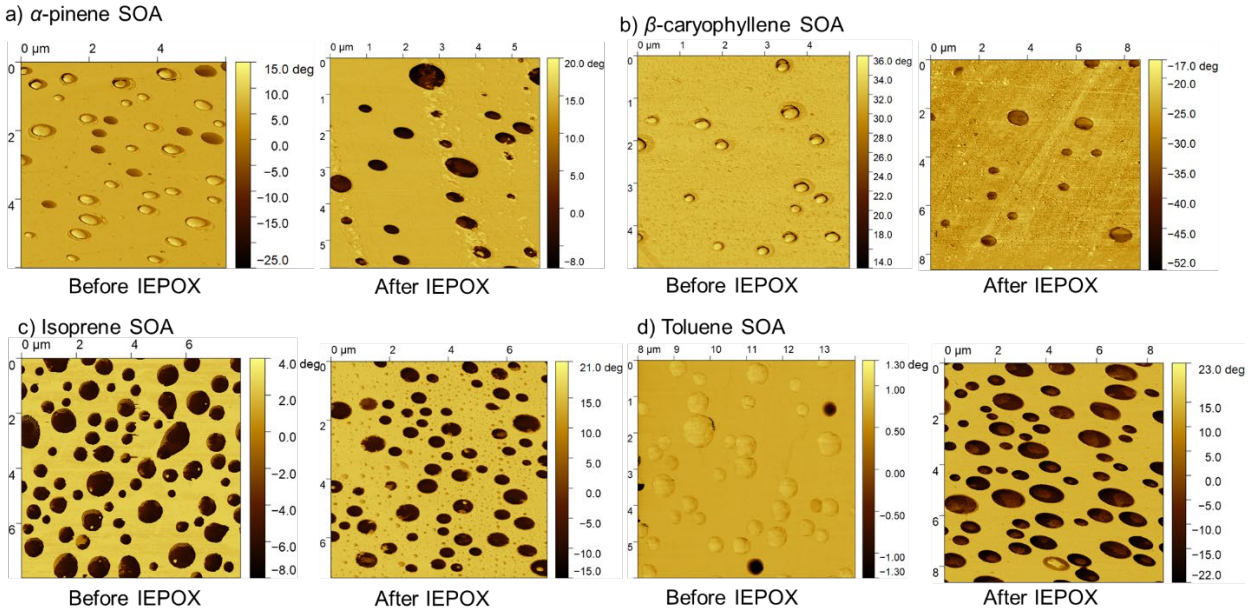

Figure B.3 AFM phase images of 150 nm SOA-coated sulfate particles before and after IEPOX uptake: a) α-pinene SOA; b) β-caryophyllene SOA; c) isoprene SOA; d) toluene SOA.

B.4 Morphology and Spreading Ratio of *β*-caryophyllene SOA Particles

After IEPOX reactive uptake, the detailed morphology and viscosity changes for *β*-caryophyllene SOA-coated sulfate particles with different sizes were investigated. A clear core-shell morphology was observed for larger particles (200 nm and 250 nm) (**Figure B.3).** This result is consistent with a previous study that showed phase separation of aerosol particles is strong size-dependent.[254] The spreading ratio of all sizes of *β*-caryophyllene SOA-coated sulfate particles ranges from 4.6 ± 0.3 to 5.4 ± 0.2. With an increase of *β*-caryophyllene SOA-coated sulfate particle size, the spreading ratios decreased significantly, suggesting larger particles were more viscous.

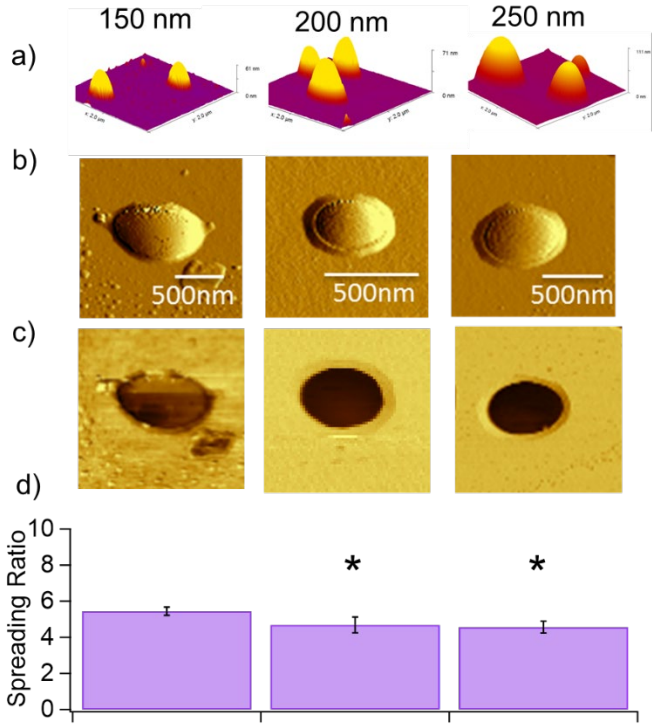

Figure B.4 Morphology and spreading ratio of size-selected *β*-caryophyllene SOA-coated sulfate particles after IEPOX uptake. a) Representative 3D AFM images; b) AFM amplitude images; c) AFM phase images; d) Bar charts show the average spreading ratio of individual particles for *β*-caryophyllene SOA with 150 nm (49 particles), 200 nm (195 particles), and 250 nm (116 particles) diameters; single asterisks denote spreading ratios of larger particles that are statistically different than 150 nm particles ($p < 0.05$) and error bars represent 2σ from gaussian fit.

B.5 Morphology and Spreading Ratio of Toluene SOA Particles

For toluene SOA-coated sulfate particles, complex morphologies were observed after IEPOX uptake and the core-shell morphologies were observed for larger particles (200 nm and 250 nm) (**Figure B.3**). The irregular shape suggests the IEPOX diffused through the organic shell and reacted with inorganic core. The average spreading ratio for toluene SOA-coated sulfate particles with different sizes ranges from 4.0 ± 0.3 to 5.2 ± 1.4. Following the same trend as other SOA particle types, the toluene SOA with 250 nm diameter is more viscous than smaller sizes (i.e., 150 nm).

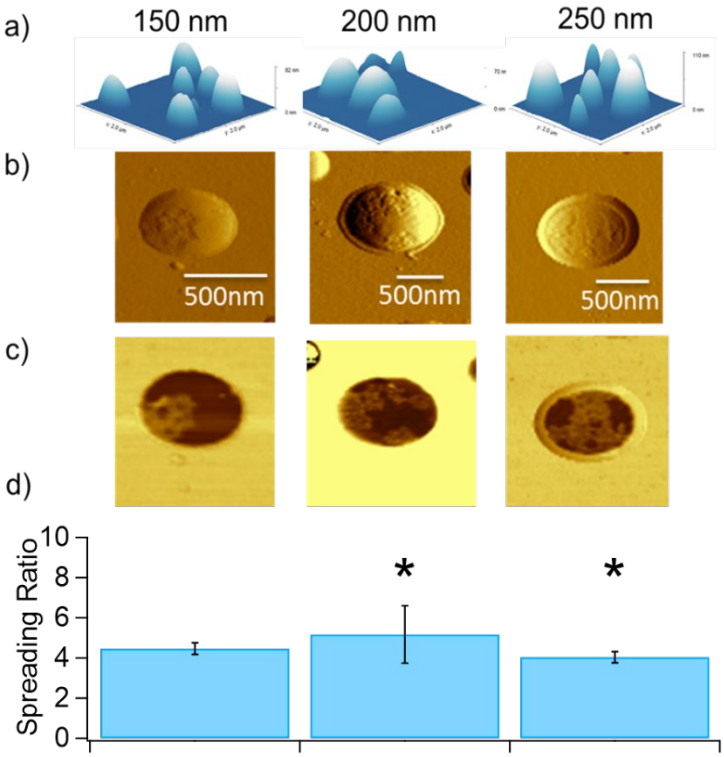

Figure B.5 Morphology and spreading ratio of size-selected toluene SOA-coated sulfate particles after IEPOX uptake. a) Representative 3D AFM images; b) AFM amplitude images; c) AFM phase images; d) Bar charts show the average spreading ratio of individual particles for toluene SOA with 150 nm (248 particles), 200 nm (136 particles), and 250 nm (262 particles) diameters; single asterisks denote spreading ratios of larger particles that are statistically different than 150 nm particles ($p < 0.05$) and error bars represent 2σ from gaussian fit.

B.6 Raman Spectra of *β*-caryophyllene SOA

For *β*-caryophyllene SOA, the Raman spectra of particle core and shell were collected for both before and after IEPOX uptake. The peak at 975 cm^{-1} is be assigned to sulfate $\nu_s(SO_4^{2-})$ and it only was observed in particle core. More organic peaks at 2889 cm^{-1}, 2936 cm^{-1}, and 2976 cm^{-1} were observed after IEPOX uptake, which are corresponding to symmetric stretches of C-H in methyl groups, asymmetric stretches of C-H in methylene group, and asymmetric stretches of C-H in methyl groups, respectively.[217]

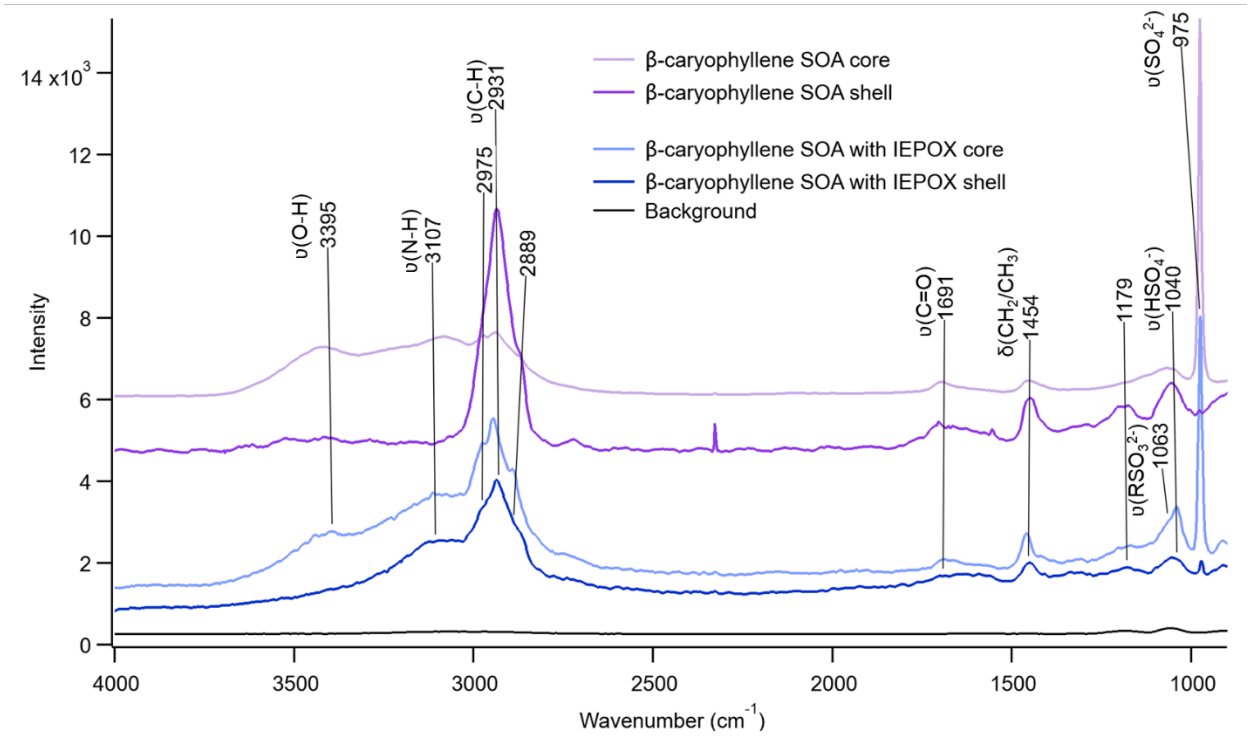

Figure B.6 Raman spectra of representative individual *β*-caryophyllene SOA particle core and shell before and after IEPOX uptake, spectra were offset vertically for clarity.

B.7 Raman Spectra of Isoprene SOA

Raman spectra were collected for isoprene SOA before and after IEPOX uptake. The $\nu_s(SO_4^{2-})$ at 975 cm^{-1} was observed before IEPOX, while after IEPOX uptake the peaks at 1012 cm^{-1} and 1052 cm^{-1} are assigned to IEPOX-derived organosulfates and bisulfate,[211] respectively. A peak at 1446 cm^{-1} is assigned to the asymmetric methylene group δ(C-H). Peaks at 2845 cm^{-1} and 2941 cm^{-1} are assigned to the symmetric and asymmetric stretches of C-H in methylene groups, respectively, whereas peaks at 2879 cm^{-1} and 2981 cm^{-1} are assigned to the symmetric and asymmetric stretches of C-H in methyl groups, respectively.

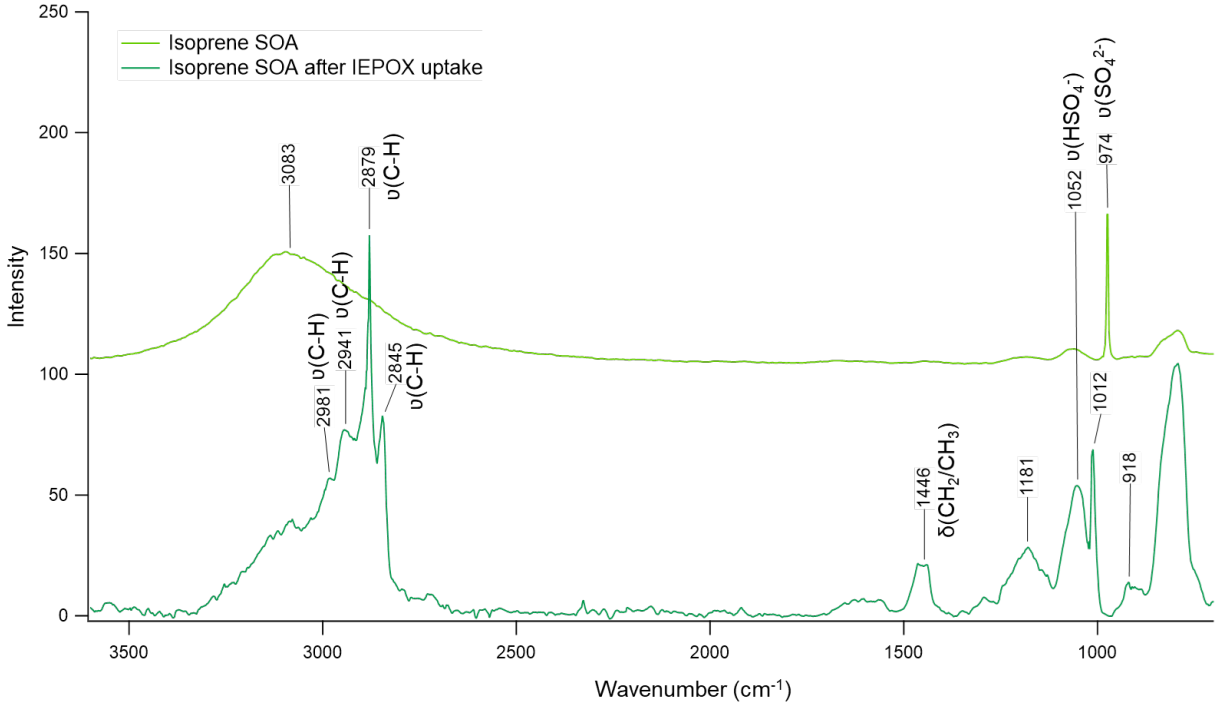

Figure B.7 Raman spectra of representative individual isoprene SOA-coated sulfate particles before and after IEPOX uptake.

B.8 Raman Spectra of Toluene SOA

Raman spectra were collected for toluene SOA before and after IEPOX uptake to understand the chemical composition modification. Raman spectra show the $\nu_s(SO_4^{2-})$ at 975 cm^{-1} before and after IEPOX uptake, and the strong band at 1039 cm^{-1} suggests bisulfate.[292] A strong peak at 1064 cm^{-1} was observed, and can be assigned to IEPOX-derived organosulfates.[168] Before IEPOX uptake, the peaks observed at 1175 cm^{-1}, 1343 cm^{-1}, 1457 cm^{-1} are corresponding to C-H group and the peaks at 1583 cm^{-1} and 1602 cm^{-1} are corresponding to carbon-carbon double bond (C=C).[293] After IEPOX uptake, the symmetric stretches of C-H in methyl group and asymmetric stretches in methylene group were observed at 2888 cm^{-1} and 2948 cm^{-1}, respectively.[211]

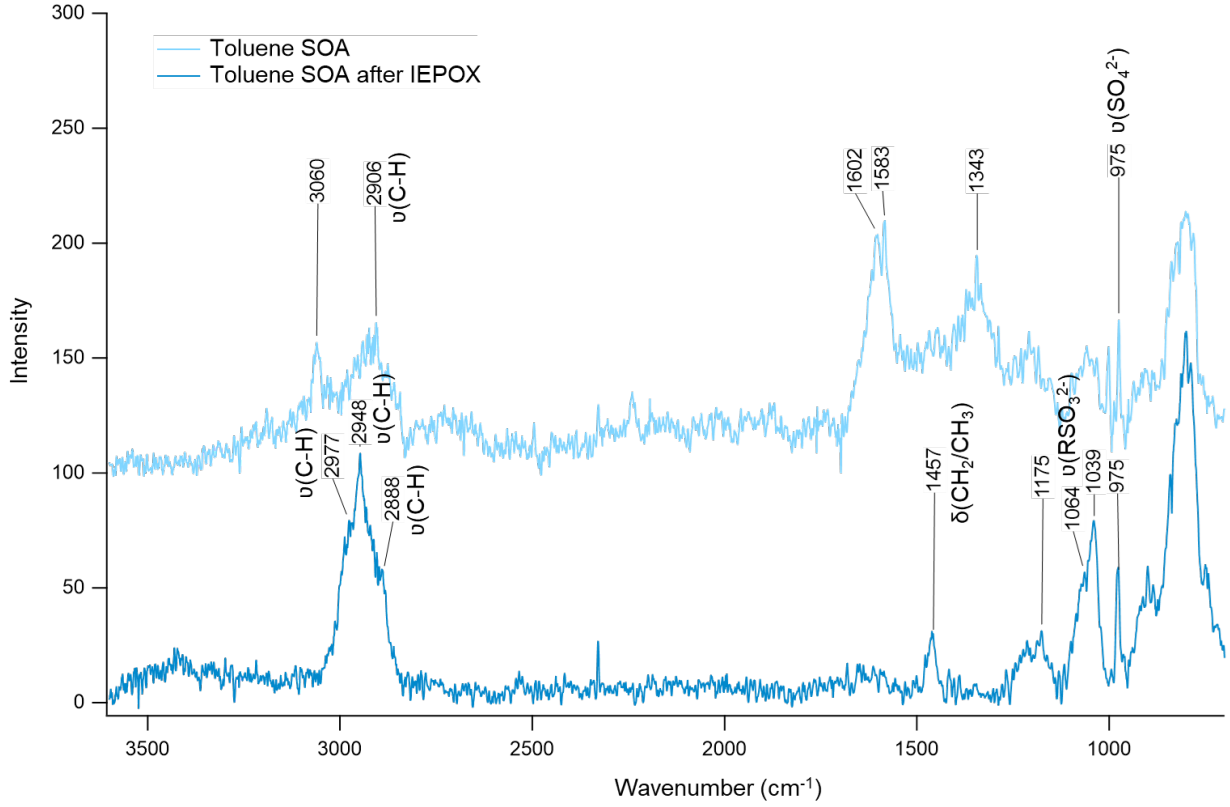

Figure B.8 Raman spectra of representative individual toluene SOA-coated sulfate particles before and after IEPOX uptake.

B.9 SEM-EDX Characterization

Scanning electron microscopy coupled to energy dispersive x-ray spectroscopy (SEM-EDX) was used to analyze the elemental composition and morphology of the four SOA-coated sulfate particle types. The spectra show particle cores contained sulfur and oxygen, indicative of sulfate and organosulfate, while the particle shells mainly contained organic compounds, which is similar to previous observations.[19]

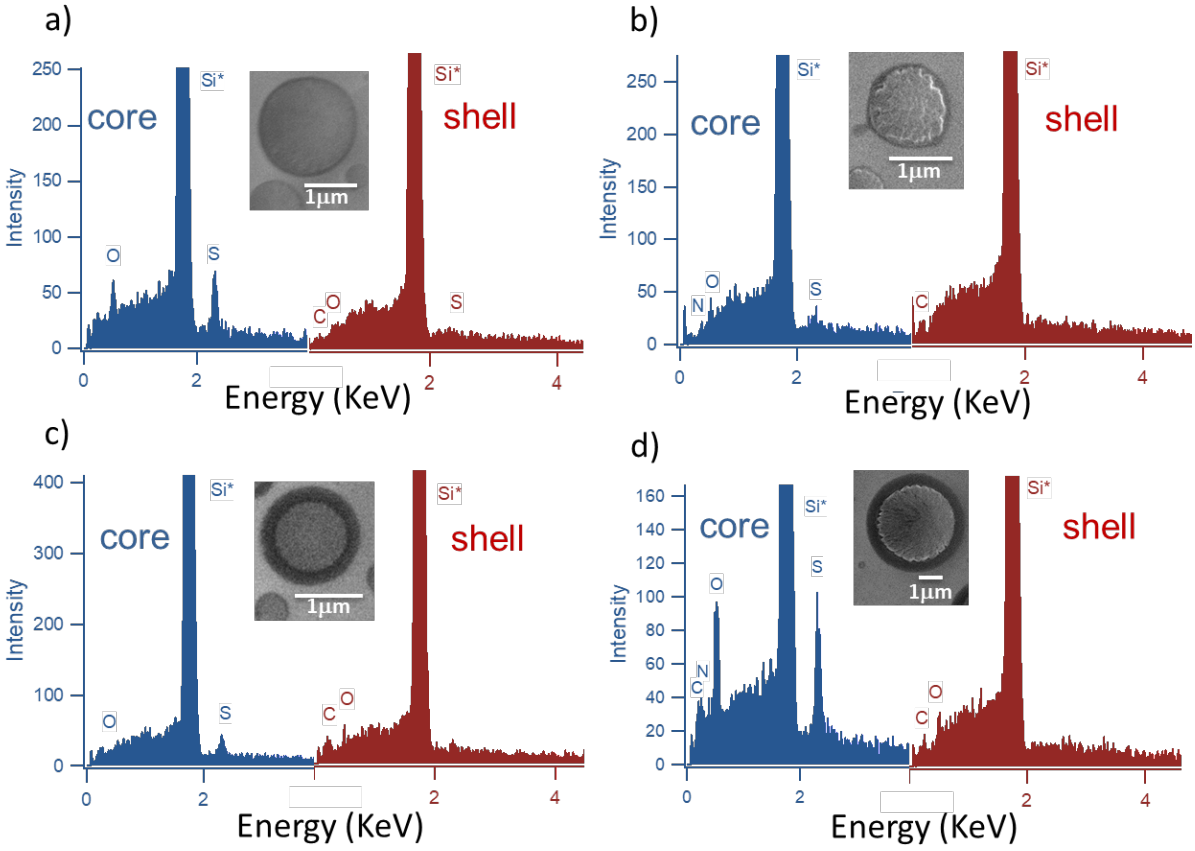

Figure B.9 SEM images and EDX spectra of representative individual particles for the 4 different SOA-coated sulfate particle types after IEPOX uptake: a) toluene SOA; b) isoprene SOA; c) α-pinene SOA; and d) β-caryophyllene SOA. Blue color represents the spectrum was collected at particle core and red color represents the spectrum was collected at particle shell.

Appendix C. Initial pH Governs Secondary Organic Aerosol Viscosity and Morphology after Uptake of Isoprene Epoxydiols (IEPOX) Supplemental Information[3]

C.1 Size Distribution of Seed Particles

Size distribution of seed particles were measured to understand particle growth after IEPOX uptake.

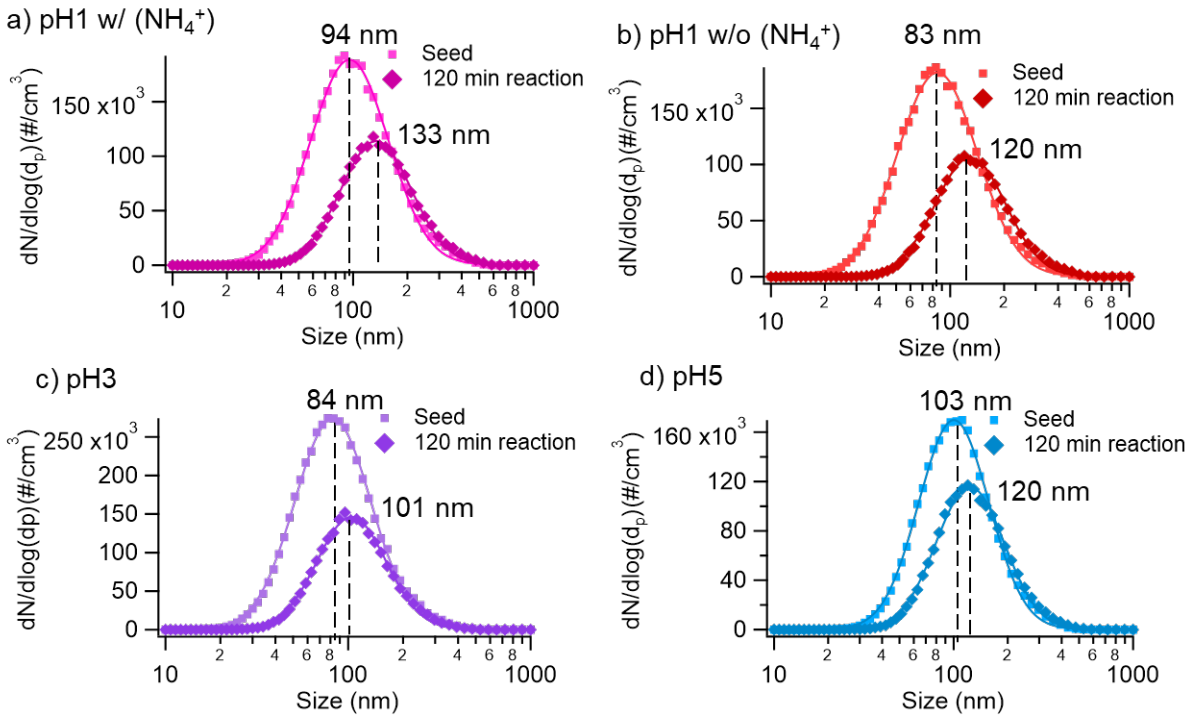

Figure C.1 Size distributions of seed aerosol particles with varying pH values were measured using a scanning electrical mobility spectrometer (SEMS, BMI Inc., Model 2100) with a size range of 10 – 1000 nm: a) pH 1 with ammonium (NH_4^+); b) pH 1 without NH_4^+; c) pH 3 ammonium sulfate; and d) pH 5 ammonium sulfate.

[3] Appendix C details supplemental information corresponding to Chapter 4

C.2 Initial Sulfate Concentration of a Seed Aerosol Only Experiment

A seed aerosol (i.e., ammonium bisulfate) only experiment was conducted, and the aerosol samples were collected for IC measurements. Comparing to the IEPOX-derived SOA experiments in Figure 4.6, this plot demonstrates that the IEPOX was converting inorganic sulfate to organosulfates and was not due to chamber wall loss.

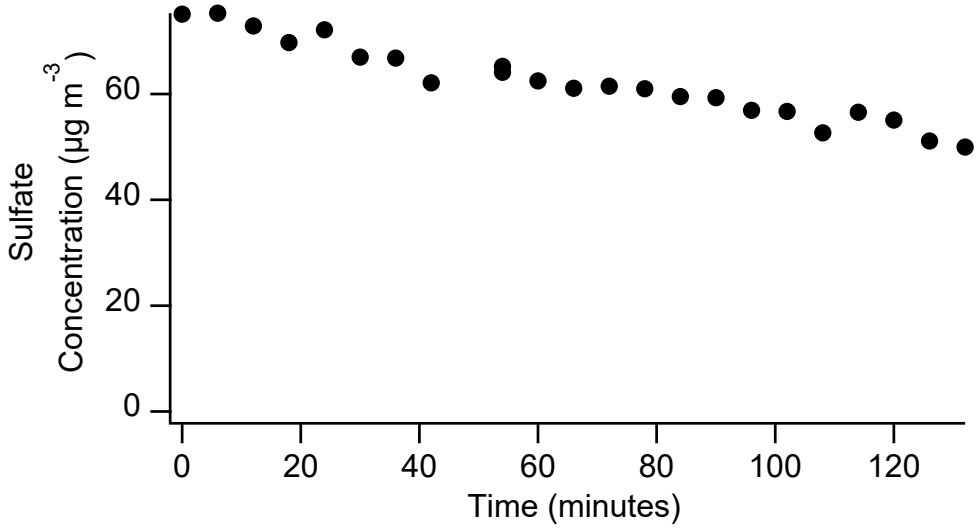

Figure C.2 Initial sulfate concentration of ammonium bisulfate seed only experiment, the data has been corrected for wall loss.

C.3 Relative Fraction of the HSO_4^- and SO_4^{2-} Ions

The relative fraction of the HSO_4^- and SO_4^{2-} ions as a function of solution pH, which suggests that HSO_4^- is dominant in the pH 1 solution while SO_4^{2-} is dominant in the pH 3 and 5 solutions.

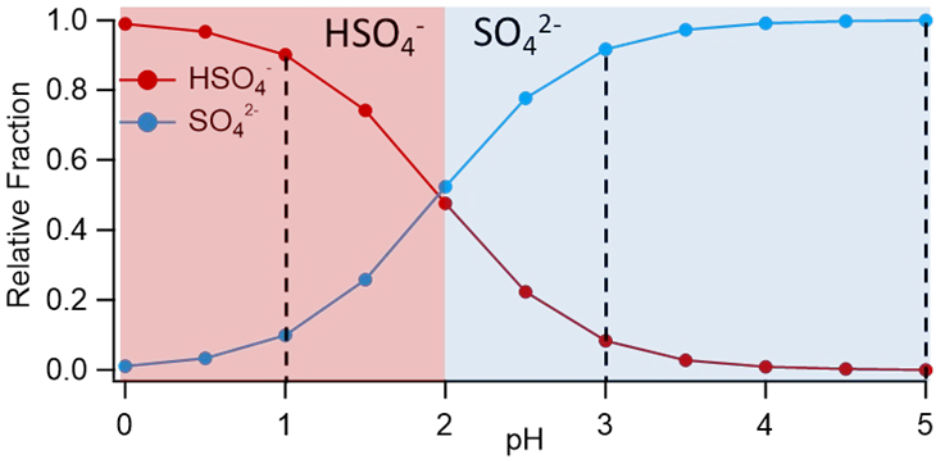

Figure C.3 Relative fraction for HSO_4^- (red) and SO_4^{2-} (blue) concentrations as a function of pH, using the dissociation constant ($K_a = 0.01$)[294] and assuming equilibrium conditions.

C.4 Chemical Composition Characterization

The SOA particles formed from pH 1 seed particles without ammonium were characterized by hydrophilic interaction liquid chromatography (HILIC)/ESI-HR-quadrupole time-of-flight mass spectrometry (QTOFMS). The concentration of 2-methyltetrols (2-MT) and its OS derivative (2-methyltetrol sulfate, IEPOX-OS) were measured, which suggests SO_4^{2-} was incorporate into organosulfates.

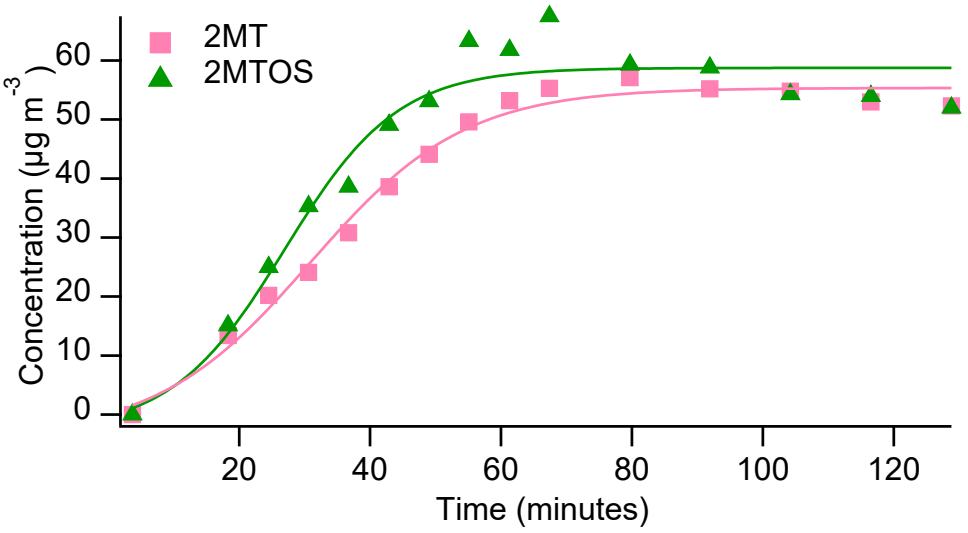

Figure C.4 2MT (pink) and 2MTOS (green) concentrations of IEPOX-derived SOA particles formed from pH 1 seed particles without ammonium. The lines represent sigmoid fit.

C.5 SEM Images for Morphology Characterization

SEM images were collected to confirm the morphology of different acidic inorganic particles exposed to IEPOX during the first hour. The images show that phase separation occurred under acidic conditions (pH=1, with or without NH_4^+), while the increased pH limited the IEPOX reactive uptake (e.g., pH=5 homogeneous particles).

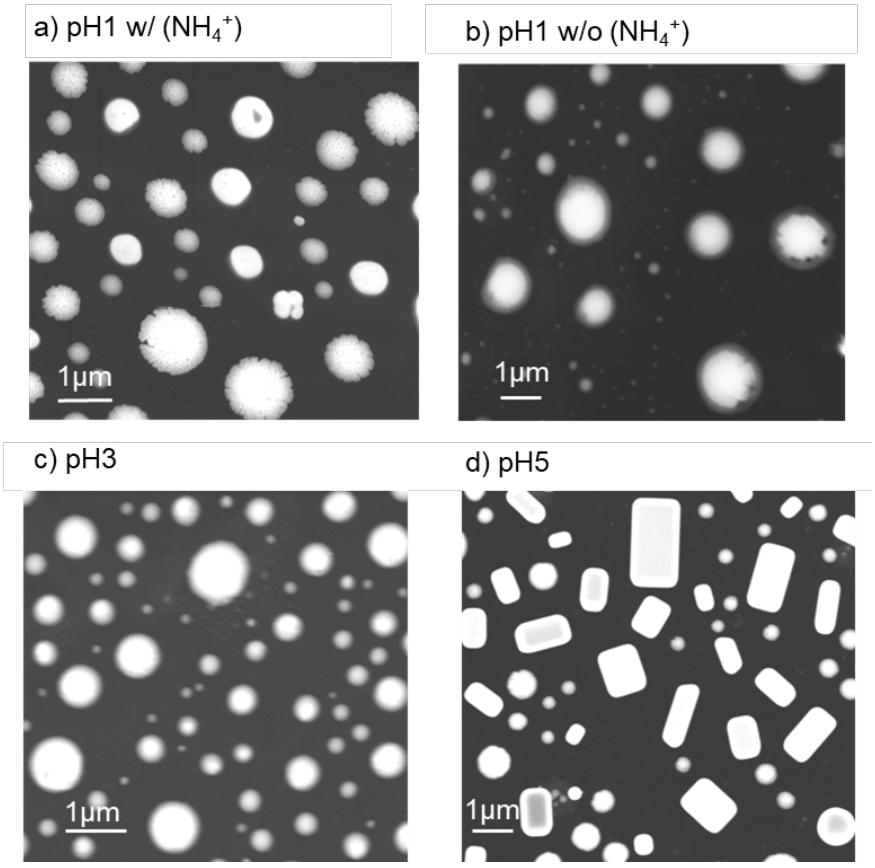

Figure C.5 SEM (FEI Helios 650) images of four types of inorganic sulfate particles after IEPOX reactive uptake for an hour, a) pH 1 seed particles without NH_4^+; b) pH 1 seed particles with NH_4^+; c) pH 3 ammonium bisulfate seed particles; d) pH5 ammonium sulfate seed particles.

C.6 Raman and PTIR Vibration Modes Assignments

Raman and PTIR spectra were collected for pH 1 seed particles with ammonium after reactive uptake of IEPOX during the first hour, the specific vibration modes were assigned for chemical characterization for representative individual particles.

Table C. 1 Experimentally determined Raman modes and tentative assignments for pH1 ammonium bisulfate particle after IEPOX uptake for an hour.[168]

Assignments	Raman (cm^{-1})	PTIR (cm^{-1})
$\nu_s(SO_4^{2-})$	978	-
$\nu_s(HSO_4^-)$	1045	-
$\nu_s(RO\text{-}SO_3^-)$	1069	880
$\nu_s(RO\text{-}SO_3^-)$	-	914
$\nu_s(RO\text{-}SO_3^-)$	-	1034
$\nu_s(SO_4^{2-})$	-	1076
$\nu_{as}(SO_4^{2-})$	1096	1108
$\nu_s(ROSO_3^-)$	-	1206
$\delta(COO^-)$	1413	-
$\delta(CH_2$ & $CH_3)$	1461	-
$\delta(CH_2)$	1616	-
$\nu_s(CH_3)$	2890	-
ν_{as} (CH_3)	2944	-
$\nu_s(NH_4^+)$	3124	1448
ν(OH)	3431	-

Appendix D. Direct Measurement of Glass Transition Temperature for Individual Submicron Atmospheric Aerosol Supplemental Information[4]

D.1 AFM thermal analysis was calibrate using HDPE, PCL, and PET

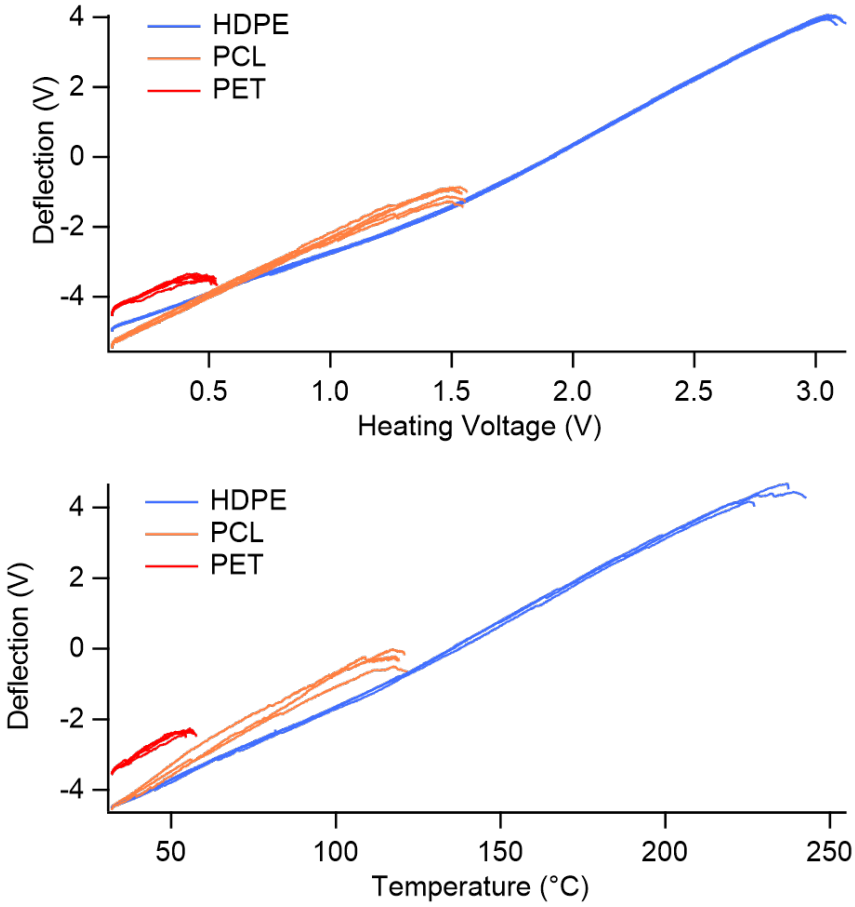

Figure D.1 Heating voltage of calibration standards were collected and converted to corresponding temperature.

[4] Appendix D details supplemental information corresponding to Chapter 5

D.2 Single temperature ramps were collected for four standards including: sucrose, ouabain, raffinose, and maltoheptaose.

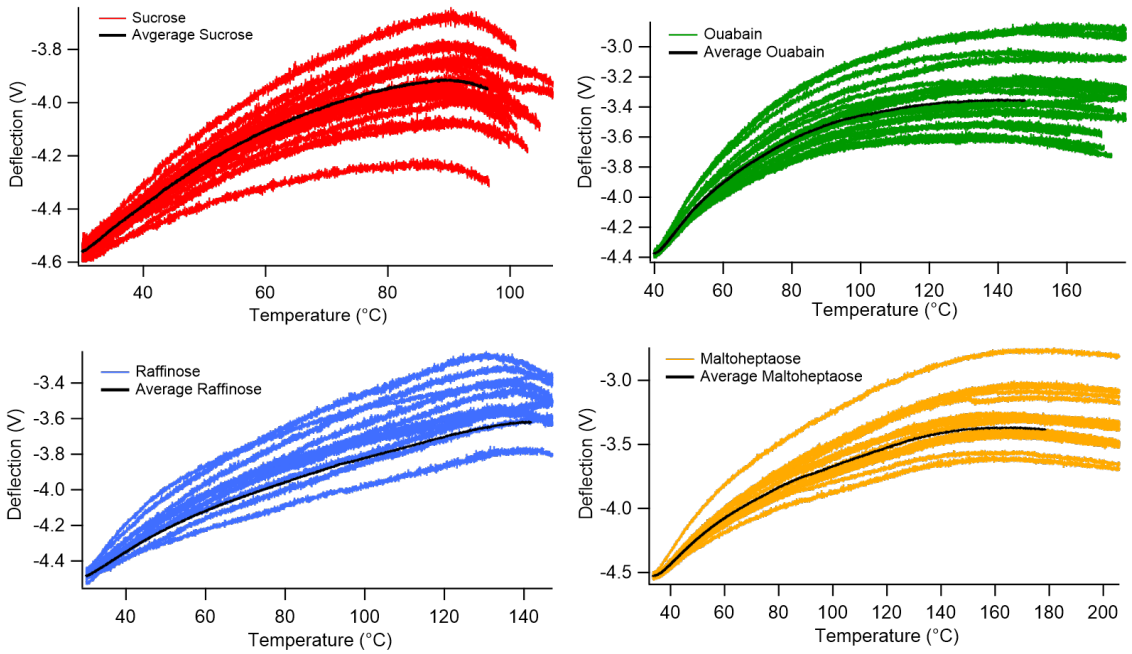

Figure D.2 Temperature ramp of individual particles made from sucrose, ouabain, raffinose, and maltoheptaose, the black line represents the average of individual temperature ramp.

D.3 PTIR spectra of phase-separated particles

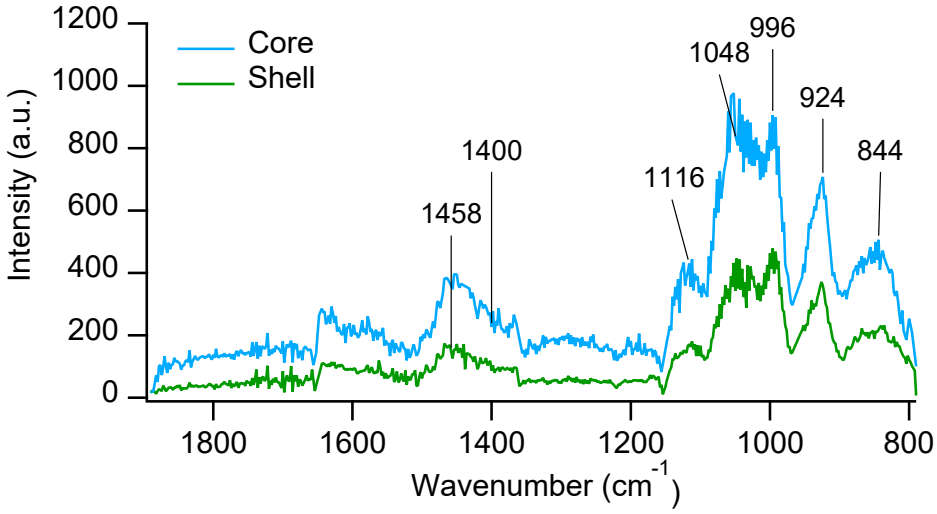

Figure D.3 PTIR spectra of individual phase separated particle core (blue) and shell (green)

References

1. Seinfeld, J.; Pandis, S. In *Atmospheric Chemistry and Physics: From Air Pollution to Climate Change*, John Wiley& Sons, Inc New York: 2006.
2. Pöschl, U., Atmospheric aerosols: composition, transformation, climate and health effects. *Angew Chem Int Ed Engl* **2005,** *44* (46), 7520-40.
3. Prather, K. A.; Hatch, C. D.; Grassian, V. H., Analysis of atmospheric aerosols. *Annu Rev Anal Chem (Palo Alto Calif)* **2008,** *1*, 485-514.
4. Lambe, A. T.; Onasch, T. B.; Massoli, P.; Croasdale, D. R.; Wright, J. P.; Ahern, A. T.; Williams, L. R.; Worsnop, D. R.; Brune, W. H.; Davidovits, P., Laboratory studies of the chemical composition and cloud condensation nuclei (CCN) activity of secondary organic aerosol (SOA) and oxidized primary organic aerosol (OPOA). *Atmos. Chem. Phys.* **2011,** *11* (17), 8913-8928.
5. Stocker, T. F. Q., D. *Climate change 2013: The physical science basis. Working group I contribution to the fifth assessment report of the intergovernmental panel on climate change.*; Cambridge, UK and New York, NY, USA, 2013.
6. Evaluation-IHME, I. f. H. M. a. Global Burden of Disease Compare Data Visualization. . http://www.healthdata.org/data-visualization/gbd-compare.
7. Pope, C. A.; Dockery, D. W., Health Effects of Fine Particulate Air Pollution: Lines that Connect. *Journal of the Air & Waste Management Association* **2006,** *56* (6), 709-742.
8. Ren-Jian, Z.; Kin-Fai, H.; Zhen-Xing, S., The Role of Aerosol in Climate Change, the Environment, and Human Health. *Atmospheric and Oceanic Science Letters* **2012,** *5* (2), 156-161.
9. Shiraiwa, M.; Ueda, K.; Pozzer, A.; Lammel, G.; Kampf, C. J.; Fushimi, A.; Enami, S.; Arangio, A. M.; Fröhlich-Nowoisky, J.; Fujitani, Y.; Furuyama, A.; Lakey, P. S. J.; Lelieveld, J.; Lucas, K.; Morino, Y.; Pöschl, U.; Takahama, S.; Takami, A.; Tong, H.; Weber, B.; Yoshino, A.; Sato, K., Aerosol Health Effects from Molecular to Global Scales. *Environmental Science & Technology* **2017,** *51* (23), 13545-13567.
10. Arashiro, M.; Lin, Y. H.; Zhang, Z.; Sexton, K. G.; Gold, A.; Jaspers, I.; Fry, R. C.; Surratt, J. D., Effect of secondary organic aerosol from isoprene-derived hydroxyhydroperoxides on the expression of oxidative stress response genes in human bronchial epithelial cells. *Environ Sci Process Impacts* **2018,** *20* (2), 332-339.
11. Lakey, P. S. J.; Berkemeier, T.; Tong, H.; Arangio, A. M.; Lucas, K.; Pöschl, U.; Shiraiwa, M., Chemical exposure-response relationship between air pollutants and reactive oxygen species in the human respiratory tract. *Scientific Reports* **2016,** *6* (1), 32916.
12. Shiraiwa, M.; Ueda, K.; Pozzer, A.; Lammel, G.; Kampf, C. J.; Fushimi, A.; Enami, S.; Arangio, A. M.; Fröhlich-Nowoisky, J.; Fujitani, Y.; Furuyama, A.; Lakey, P. S. J.; Lelieveld, J.; Lucas, K.; Morino, Y.; Pöschl, U.; Takahama, S.; Takami, A.; Tong, H.; Weber, B.; Yoshino, A.; Sato, K., Aerosol Health Effects from Molecular to Global Scales. *Environ Sci Technol* **2017,** *51* (23), 13545-13567.
13. Pope, C. A., 3rd; Dockery, D. W., Health effects of fine particulate air pollution: lines that connect. *J Air Waste Manag Assoc* **2006,** *56* (6), 709-42.
14. Pöschl, U., Atmospheric Aerosols: Composition, Transformation, Climate and Health Effects. *Angewandte Chemie International Edition* **2005,** *44* (46), 7520-7540.

15. Tomasi, C.; Lupi, A., Primary and Secondary Sources of Atmospheric Aerosol. In *Atmospheric Aerosols*, 2017; pp 1-86.
16. Andreae, M. O.; Rosenfeld, D., Aerosol–cloud–precipitation interactions. Part 1. The nature and sources of cloud-active aerosols. *Earth-Science Reviews* **2008,** *89* (1), 13-41.
17. Hallquist, M.; Wenger, J. C.; Baltensperger, U.; Rudich, Y.; Simpson, D.; Claeys, M.; Dommen, J.; Donahue, N. M.; George, C.; Goldstein, A. H.; Hamilton, J. F.; Herrmann, H.; Hoffmann, T.; Iinuma, Y.; Jang, M.; Jenkin, M. E.; Jimenez, J. L.; Kiendler-Scharr, A.; Maenhaut, W.; McFiggans, G.; Mentel, T. F.; Monod, A.; Prévôt, A. S. H.; Seinfeld, J. H.; Surratt, J. D.; Szmigielski, R.; Wildt, J., The formation, properties and impact of secondary organic aerosol: current and emerging issues. *Atmos. Chem. Phys.* **2009,** *9* (14), 5155-5236.
18. Ziemann, P. J.; Atkinson, R., Kinetics, products, and mechanisms of secondary organic aerosol formation. *Chemical Society Reviews* **2012,** *41* (19), 6582-6605.
19. Olson, N. E.; Lei, Z.; Craig, R. L.; Zhang, Y.; Chen, Y.; Lambe, A. T.; Zhang, Z.; Gold, A.; Surratt, J. D.; Ault, A. P., Reactive Uptake of Isoprene Epoxydiols Increases the Viscosity of the Core of Phase-Separated Aerosol Particles. *ACS Earth Space Chem.* **2019,** *3* (8), 1402-1414.
20. Riva, M.; Budisulistiorini, S. H.; Zhang, Z.; Gold, A.; Thornton, J. A.; Turpin, B. J.; Surratt, J. D., Multiphase reactivity of gaseous hydroperoxide oligomers produced from isoprene ozonolysis in the presence of acidified aerosols. *Atmospheric Environment* **2017,** *152*, 314-322.
21. Zhang, Y.; Chen, Y.; Lambe, A. T.; Olson, N. E.; Lei, Z.; Craig, R. L.; Zhang, Z.; Gold, A.; Onasch, T. B.; Jayne, J. T.; Worsnop, D. R.; Gaston, C. J.; Thornton, J. A.; Vizuete, W.; Ault, A. P.; Surratt, J. D., Effect of the Aerosol-Phase State on Secondary Organic Aerosol Formation from the Reactive Uptake of Isoprene-Derived Epoxydiols (IEPOX). *Environmental Science & Technology Letters* **2018,** *5* (3), 167-174.
22. Stocker, T. F.; Qin, D., *Climate change 2013: The physical science basis. Working group I contribution to the fifth assessment report of the intergovernmental panel on climate change*. Cambridge University Press: Cambridge, UK and New York, NY, USA, 2013.
23. Zhang, Q.; Jimenez, J. L.; Worsnop, D. R.; Canagaratna, M., A Case Study of Urban Particle Acidity and Its Influence on Secondary Organic Aerosol. *Environmental Science & Technology* **2007,** *41* (9), 3213-3219.
24. Surratt, J. D.; Lewandowski, M.; Offenberg, J. H.; Jaoui, M.; Kleindienst, T. E.; Edney, E. O.; Seinfeld, J. H., Effect of Acidity on Secondary Organic Aerosol Formation from Isoprene. *Environmental Science & Technology* **2007,** *41* (15), 5363-5369.
25. Zhang, Y.; Chen, Y.; Lei, Z.; Olson, N. E.; Riva, M.; Koss, A. R.; Zhang, Z.; Gold, A.; Jayne, J. T.; Worsnop, D. R.; Onasch, T. B.; Kroll, J. H.; Turpin, B. J.; Ault, A. P.; Surratt, J. D., Joint Impacts of Acidity and Viscosity on the Formation of Secondary Organic Aerosol from Isoprene Epoxydiols (IEPOX) in Phase Separated Particles. *ACS Earth and Space Chemistry* **2019,** *3* (12), 2646-2658.
26. Gaston, C. J.; Riedel, T. P.; Zhang, Z.; Gold, A.; Surratt, J. D.; Thornton, J. A., Reactive Uptake of an Isoprene-Derived Epoxydiol to Submicron Aerosol Particles. *Environmental Science & Technology* **2014,** *48* (19), 11178-11186.
27. Surratt, J. D.; Murphy, S. M.; Kroll, J. H.; Ng, N. L.; Hildebrandt, L.; Sorooshian, A.; Szmigielski, R.; Vermeylen, R.; Maenhaut, W.; Claeys, M.; Flagan, R. C.; Seinfeld, J. H., Chemical Composition of Secondary Organic Aerosol Formed from the Photooxidation of Isoprene. *The Journal of Physical Chemistry A* **2006,** *110* (31), 9665-9690.

28. Tolocka, M. P.; Jang, M.; Ginter, J. M.; Cox, F. J.; Kamens, R. M.; Johnston, M. V., Formation of Oligomers in Secondary Organic Aerosol. *Environmental Science & Technology* **2004,** *38* (5), 1428-1434.
29. Guo, H.; Xu, L.; Bougiatioti, A.; Cerully, K. M.; Capps, S. L.; Hite Jr, J. R.; Carlton, A. G.; Lee, S. H.; Bergin, M. H.; Ng, N. L.; Nenes, A.; Weber, R. J., Fine-particle water and pH in the southeastern United States. *Atmos. Chem. Phys.* **2015,** *15* (9), 5211-5228.
30. Lin, Y.-H.; Zhang, Z.; Docherty, K. S.; Zhang, H.; Budisulistiorini, S. H.; Rubitschun, C. L.; Shaw, S. L.; Knipping, E. M.; Edgerton, E. S.; Kleindienst, T. E.; Gold, A.; Surratt, J. D., Isoprene epoxydiols as precursors to secondary organic aerosol formation: acid-catalyzed reactive uptake studies with authentic compounds. *Environmental science & technology* **2012,** *46* (1), 250-258.
31. Desboeufs, K. V.; Sofikitis, A.; Losno, R.; Colin, J. L.; Ausset, P., Dissolution and solubility of trace metals from natural and anthropogenic aerosol particulate matter. *Chemosphere* **2005,** *58* (2), 195-203.
32. Pye, H. O. T.; Nenes, A.; Alexander, B.; Ault, A. P.; Barth, M. C.; Clegg, S. L.; Collett Jr, J. L.; Fahey, K. M.; Hennigan, C. J.; Herrmann, H.; Kanakidou, M.; Kelly, J. T.; Ku, I. T.; McNeill, V. F.; Riemer, N.; Schaefer, T.; Shi, G.; Tilgner, A.; Walker, J. T.; Wang, T.; Weber, R.; Xing, J.; Zaveri, R. A.; Zuend, A., The acidity of atmospheric particles and clouds. *Atmos. Chem. Phys.* **2020,** *20* (8), 4809-4888.
33. Craig, R. L.; Peterson, P. K.; Nandy, L.; Lei, Z.; Hossain, M. A.; Camarena, S.; Dodson, R. A.; Cook, R. D.; Dutcher, C. S.; Ault, A. P., Direct Determination of Aerosol pH: Size-Resolved Measurements of Submicrometer and Supermicrometer Aqueous Particles. *Analytical Chemistry* **2018,** *90* (19), 11232-11239.
34. Rindelaub, J. D.; Craig, R. L.; Nandy, L.; Bondy, A. L.; Dutcher, C. S.; Shepson, P. B.; Ault, A. P., Direct Measurement of pH in Individual Particles via Raman Microspectroscopy and Variation in Acidity with Relative Humidity. *The Journal of Physical Chemistry A* **2016,** *120* (6), 911-917.
35. Ault, A. P., Aerosol Acidity: Novel Measurements and Implications for Atmospheric Chemistry. *Accounts of Chemical Research* **2020,** *53* (9), 1703-1714.
36. Freedman, M. A., Phase separation in organic aerosol. *Chemical Society Reviews* **2017,** *46* (24), 7694-7705.
37. Qiu, Y.; Molinero, V., Morphology of Liquid–Liquid Phase Separated Aerosols. *Journal of the American Chemical Society* **2015,** *137* (33), 10642-10651.
38. Riva, M.; Chen, Y.; Zhang, Y.; Lei, Z.; Olson, N. E.; Boyer, H. C.; Narayan, S.; Yee, L. D.; Green, H. S.; Cui, T.; Zhang, Z.; Baumann, K.; Fort, M.; Edgerton, E.; Budisulistiorini, S. H.; Rose, C. A.; Ribeiro, I. O.; e Oliveira, R. L.; dos Santos, E. O.; Machado, C. M. D.; Szopa, S.; Zhao, Y.; Alves, E. G.; de Sá, S. S.; Hu, W.; Knipping, E. M.; Shaw, S. L.; Duvoisin Junior, S.; de Souza, R. A. F.; Palm, B. B.; Jimenez, J.-L.; Glasius, M.; Goldstein, A. H.; Pye, H. O. T.; Gold, A.; Turpin, B. J.; Vizuete, W.; Martin, S. T.; Thornton, J. A.; Dutcher, C. S.; Ault, A. P.; Surratt, J. D., Increasing Isoprene Epoxydiol-to-Inorganic Sulfate Aerosol Ratio Results in Extensive Conversion of Inorganic Sulfate to Organosulfur Forms: Implications for Aerosol Physicochemical Properties. *Environmental Science & Technology* **2019,** *53* (15), 8682-8694.
39. Shiraiwa, M.; Zuend, A.; Bertram, A. K.; Seinfeld, J. H., Gas–particle partitioning of atmospheric aerosols: interplay of physical state, non-ideal mixing and morphology. *Physical Chemistry Chemical Physics* **2013,** *15* (27), 11441-11453.

40. Song, M.; Ham, S.; Andrews, R. J.; You, Y.; Bertram, A. K., Liquid–liquid phase separation in organic particles containing one and two organic species: importance of the average O : C. *Atmos. Chem. Phys.* **2018,** *18* (16), 12075-12084.
41. Song, M.; Marcolli, C.; Krieger, U. K.; Lienhard, D. M.; Peter, T., Morphologies of mixed organic/inorganic/aqueous aerosol droplets. *Faraday Discussions* **2013,** *165* (0), 289-316.
42. Song, M.; Marcolli, C.; Krieger, U. K.; Zuend, A.; Peter, T., Liquid-liquid phase separation and morphology of internally mixed dicarboxylic acids/ammonium sulfate/water particles. *Atmos. Chem. Phys.* **2012,** *12* (5), 2691-2712.
43. Xu, L.; Fukushima, S.; Sobanska, S.; Murata, K.; Naganuma, A.; Liu, L.; Wang, Y.; Niu, H.; Shi, Z.; Kojima, T.; Zhang, D.; Li, W., Tracing the evolution of morphology and mixing state of soot particles along with the movement of an Asian dust storm. *Atmos. Chem. Phys.* **2020,** *20* (22), 14321-14332.
44. Freedman, M. A., Liquid–Liquid Phase Separation in Supermicrometer and Submicrometer Aerosol Particles. *Accounts of Chemical Research* **2020,** *53* (6), 1102-1110.
45. Martin, S. T., Phase Transitions of Aqueous Atmospheric Particles. *Chemical Reviews* **2000,** *100* (9), 3403-3454.
46. O'Brien, R. E.; Wang, B.; Kelly, S. T.; Lundt, N.; You, Y.; Bertram, A. K.; Leone, S. R.; Laskin, A.; Gilles, M. K., Liquid–Liquid Phase Separation in Aerosol Particles: Imaging at the Nanometer Scale. *Environmental Science & Technology* **2015,** *49* (8), 4995-5002.
47. Pajunoja, A.; Hu, W.; Leong, Y. J.; Taylor, N. F.; Miettinen, P.; Palm, B. B.; Mikkonen, S.; Collins, D. R.; Jimenez, J. L.; Virtanen, A., Phase state of ambient aerosol linked with water uptake and chemical aging in the southeastern US. *Atmos. Chem. Phys.* **2016,** *16* (17), 11163-11176.
48. Pankow, J. F., Gas/particle partitioning of neutral and ionizing compounds to single and multi-phase aerosol particles. 1. Unified modeling framework. *Atmospheric Environment* **2003,** *37* (24), 3323-3333.
49. Cosman, L. M.; Knopf, D. A.; Bertram, A. K., N2O5 reactive uptake on aqueous sulfuric acid solutions coated with branched and straight-chain insoluble organic surfactants. *J Phys Chem A* **2008,** *112* (11), 2386-96.
50. Huang, Y.; Mahrt, F.; Xu, S.; Shiraiwa, M.; Zuend, A.; Bertram, A. K., Coexistence of three liquid phases in individual atmospheric aerosol particles. *Proc Natl Acad Sci U S A* **2021,** *118* (16).
51. Ham, S.; Babar, Z. B.; Lee, J. B.; Lim, H. J.; Song, M., Liquid–liquid phase separation in secondary organic aerosol particles produced from α-pinene ozonolysis and α-pinene photooxidation with/without ammonia. *Atmos. Chem. Phys.* **2019,** *19* (14), 9321-9331.
52. Zuend, A.; Seinfeld, J. H., Modeling the gas-particle partitioning of secondary organic aerosol: the importance of liquid-liquid phase separation. *Atmos. Chem. Phys.* **2012,** *12* (9), 3857-3882.
53. You, Y.; Renbaum-Wolff, L.; Carreras-Sospedra, M.; Hanna, S. J.; Hiranuma, N.; Kamal, S.; Smith, M. L.; Zhang, X.; Weber, R. J.; Shilling, J. E.; Dabdub, D.; Martin, S. T.; Bertram, A. K., Images reveal that atmospheric particles can undergo liquid–liquid phase separations. *Proceedings of the National Academy of Sciences* **2012,** *109* (33), 13188.
54. Fuzzi, S.; Andreae, M. O.; Huebert, B. J.; Kulmala, M.; Bond, T. C.; Boy, M.; Doherty, S. J.; Guenther, A.; Kanakidou, M.; Kawamura, K.; Kerminen, V. M.; Lohmann, U.; Russell, L. M.; Pöschl, U., Critical assessment of the current state of scientific knowledge, terminology,

and research needs concerning the role of organic aerosols in the atmosphere, climate, and global change. *Atmos. Chem. Phys.* **2006,** *6* (7), 2017-2038.
55. Shiraiwa, M.; Li, Y.; Tsimpidi, A. P.; Karydis, V. A.; Berkemeier, T.; Pandis, S. N.; Lelieveld, J.; Koop, T.; Pöschl, U., Global distribution of particle phase state in atmospheric secondary organic aerosols. *Nature Communications* **2017,** *8* (1), 15002.
56. Reid, J. P.; Bertram, A. K.; Topping, D. O.; Laskin, A.; Martin, S. T.; Petters, M. D.; Pope, F. D.; Rovelli, G., The viscosity of atmospherically relevant organic particles. *Nature Communications* **2018,** *9* (1), 956.
57. Schmedding, R.; Rasool, Q. Z.; Zhang, Y.; Pye, H. O. T.; Zhang, H.; Chen, Y.; Surratt, J. D.; Lopez-Hilfiker, F. D.; Thornton, J. A.; Goldstein, A. H.; Vizuete, W., Predicting secondary organic aerosol phase state and viscosity and its effect on multiphase chemistry in a regional-scale air quality model. *Atmos. Chem. Phys.* **2020,** *20* (13), 8201-8225.
58. Koop, T.; Bookhold, J.; Shiraiwa, M.; Pöschl, U., Glass transition and phase state of organic compounds: dependency on molecular properties and implications for secondary organic aerosols in the atmosphere. *Physical Chemistry Chemical Physics* **2011,** *13* (43), 19238-19255.
59. Virtanen, A.; Joutsensaari, J.; Koop, T.; Kannosto, J.; Yli-Pirilä, P.; Leskinen, J.; Mäkelä, J. M.; Holopainen, J. K.; Pöschl, U.; Kulmala, M.; Worsnop, D. R.; Laaksonen, A., An amorphous solid state of biogenic secondary organic aerosol particles. *Nature* **2010,** *467* (7317), 824-827.
60. Zobrist, B.; Marcolli, C.; Pedernera, D. A.; Koop, T., Do atmospheric aerosols form glasses? *Atmos. Chem. Phys.* **2008,** *8* (17), 5221-5244.
61. Mikhailov, E.; Vlasenko, S.; Martin, S. T.; Koop, T.; Pöschl, U., Amorphous and crystalline aerosol particles interacting with water vapor: conceptual framework and experimental evidence for restructuring, phase transitions and kinetic limitations. *Atmospheric Chemistry & Physics* **2009,** *9*, 9491.
62. Gervasi, N. R.; Topping, D. O.; Zuend, A., A predictive group-contribution model for the viscosity of aqueous organic aerosol. *Atmos. Chem. Phys.* **2020,** *20* (5), 2987-3008.
63. Huang, W.; Saathoff, H.; Pajunoja, A.; Shen, X.; Naumann, K. H.; Wagner, R.; Virtanen, A.; Leisner, T.; Mohr, C., α-Pinene secondary organic aerosol at low temperature: chemical composition and implications for particle viscosity. *Atmos. Chem. Phys.* **2018,** *18* (4), 2883-2898.
64. Reid, J.; Bertram, A.; Topping, D.; Laskin, A.; Martin, S.; Petters, M.; Pope, F.; Rovelli, G., The viscosity of atmospherically relevant organic particles. *Nature Communications* **2018,** *9*.
65. Song, M.; Liu, P.; Hanna, S.; Li, Y.; Martin, S.; Bertram, A., Relative humidity-dependent viscosities of isoprene-derived secondary organic material and atmospheric implications for isoprene-dominant forests. *Atmospheric Chemistry and Physics* **2015,** *15*.
66. Song, M.; Liu, P. F.; Hanna, S. J.; Zaveri, R. A.; Potter, K.; You, Y.; Martin, S. T.; Bertram, A. K., Relative humidity-dependent viscosity of secondary organic material from toluene photo-oxidation and possible implications for organic particulate matter over megacities. *Atmos. Chem. Phys.* **2016,** *16* (14), 8817-8830.
67. Maclean, A. M.; Smith, N. R.; Li, Y.; Huang, Y.; Hettiyadura, A. P. S.; Crescenzo, G. V.; Shiraiwa, M.; Laskin, A.; Nizkorodov, S. A.; Bertram, A. K., Humidity-Dependent Viscosity of Secondary Organic Aerosol from Ozonolysis of β-Caryophyllene: Measurements, Predictions, and Implications. *ACS Earth and Space Chemistry* **2021,** *5* (2), 305-318.

68. Maclean, A. M.; Butenhoff, C. L.; Grayson, J. W.; Barsanti, K.; Jimenez, J. L.; Bertram, A. K., Mixing times of organic molecules within secondary organic aerosol particles: a global planetary boundary layer perspective. *Atmos. Chem. Phys.* **2017,** *17* (21), 13037-13048.
69. Liu, P.; Li, Y. J.; Wang, Y.; Gilles, M. K.; Zaveri, R. A.; Bertram, A. K.; Martin, S. T., Lability of secondary organic particulate matter. *Proceedings of the National Academy of Sciences* **2016,** *113* (45), 12643.
70. Krieger, U. K.; Marcolli, C.; Reid, J. P., ChemInform Abstract: Exploring the Complexity of Aerosol Particle Properties and Processes Using Single Particles Techniques. *ChemInform* **2012,** *43* (48).
71. Fletcher, R. A.; Ritchie, N. W. M.; Anderson, I. M.; Small, J. A., Microscopy and Microanalysis of Individual Collected Particles. In *Aerosol Measurement*, 2011; pp 179-232.
72. Ault, A. P.; Axson, J. L., Atmospheric Aerosol Chemistry: Spectroscopic and Microscopic Advances. *Analytical Chemistry* **2017,** *89* (1), 430-452.
73. Bondy, A. L.; Kirpes, R. M.; Merzel, R. L.; Pratt, K. A.; Banaszak Holl, M. M.; Ault, A. P., Atomic Force Microscopy-Infrared Spectroscopy of Individual Atmospheric Aerosol Particles: Subdiffraction Limit Vibrational Spectroscopy and Morphological Analysis. *Analytical Chemistry* **2017,** *89* (17), 8594-8598.
74. Craig, R. L.; Nandy, L.; Axson, J. L.; Dutcher, C. S.; Ault, A. P., Spectroscopic Determination of Aerosol pH from Acid–Base Equilibria in Inorganic, Organic, and Mixed Systems. *The Journal of Physical Chemistry A* **2017,** *121* (30), 5690-5699.
75. Investigation of the chemical mixing state of individual Asian dust particles by the combined use of electron probe X-ray microanalysis and Raman microspectrometry. **2012,** *84* (7), 3145-54.
76. Sobanska, S.; Hwang, H.; Choël, M.; Jung, H. J.; Eom, H. J.; Kim, H.; Barbillat, J.; Ro, C. U., Investigation of the chemical mixing state of individual Asian dust particles by the combined use of electron probe X-ray microanalysis and Raman microspectrometry. *Anal Chem* **2012,** *84* (7), 3145-54.
77. Sobanska, S.; Falgayrac, G.; Rimetz-Planchon, J.; Perdrix, E.; Brémard, C.; Barbillat, J., Resolving the internal structure of individual atmospheric aerosol particle by the combination of Atomic Force Microscopy, ESEM–EDX, Raman and ToF–SIMS imaging. *Microchemical Journal* **2014,** *114*, 89-98.
78. Olson, N. E.; Xiao, Y.; Lei, Z.; Ault, A. P., Simultaneous Optical Photothermal Infrared (O-PTIR) and Raman Spectroscopy of Submicrometer Atmospheric Particles. *Analytical Chemistry* **2020,** *92* (14), 9932-9939.
79. Kirpes, R. M.; Bondy, A. L.; Bonanno, D.; Moffet, R. C.; Wang, B.; Laskin, A.; Ault, A. P.; Pratt, K. A., Secondary sulfate is internally mixed with sea spray aerosol and organic aerosol in the winter Arctic. *Atmos. Chem. Phys.* **2018,** *18* (6), 3937-3949.
80. Ault, A. P.; Zhao, D.; Ebben, C. J.; Tauber, M. J.; Geiger, F. M.; Prather, K. A.; Grassian, V. H., Raman microspectroscopy and vibrational sum frequency generation spectroscopy as probes of the bulk and surface compositions of size-resolved sea spray aerosol particles. *Physical Chemistry Chemical Physics* **2013,** *15* (17), 6206-6214.
81. Kirpes, R. M.; Bonanno, D.; May, N. W.; Fraund, M.; Barget, A. J.; Moffet, R. C.; Ault, A. P.; Pratt, K. A., Wintertime Arctic Sea Spray Aerosol Composition Controlled by Sea Ice Lead Microbiology. *ACS Central Science* **2019,** *5* (11), 1760-1767.
82. Ault, A. P.; Guasco, T. L.; Baltrusaitis, J.; Ryder, O. S.; Trueblood, J. V.; Collins, D. B.; Ruppel, M. J.; Cuadra-Rodriguez, L. A.; Prather, K. A.; Grassian, V. H., Heterogeneous

Reactivity of Nitric Acid with Nascent Sea Spray Aerosol: Large Differences Observed between and within Individual Particles. *J Phys Chem Lett* **2014,** *5* (15), 2493-500.
83. Bondy, A. L.; Bonanno, D.; Moffet, R. C.; Wang, B.; Laskin, A.; Ault, A. P., The diverse chemical mixing state of aerosol particles in the southeastern United States. *Atmos. Chem. Phys.* **2018,** *18* (16), 12595-12612.
84. Craig, R. L.; Bondy, A. L.; Ault, A. P., Surface Enhanced Raman Spectroscopy Enables Observations of Previously Undetectable Secondary Organic Aerosol Components at the Individual Particle Level. *Analytical Chemistry* **2015,** *87* (15), 7510-7514.
85. Craig, R. L.; Bondy, A. L.; Ault, A. P., Computer-controlled Raman microspectroscopy (CC-Raman): A method for the rapid characterization of individual atmospheric aerosol particles. *Aerosol Science and Technology* **2017,** *51* (9), 1099-1112.
86. Tirella, P. N.; Craig, R. L.; Tubbs, D. B.; Olson, N. E.; Lei, Z.; Ault, A. P., Extending surface enhanced Raman spectroscopy (SERS) of atmospheric aerosol particles to the accumulation mode (150–800 nm). *Environmental Science: Processes & Impacts* **2018,** *20* (11), 1570-1580.
87. Ofner, J.; Deckert-Gaudig, T.; Kamilli, K. A.; Held, A.; Lohninger, H.; Deckert, V.; Lendl, B., Tip-Enhanced Raman Spectroscopy of Atmospherically Relevant Aerosol Nanoparticles. *Analytical Chemistry* **2016,** *88* (19), 9766-9772.
88. Doughty, D. C.; Hill, S. C., Raman spectra of atmospheric particles measured in Maryland, USA over 22.5 h using an automated aerosol Raman spectrometer. *Journal of Quantitative Spectroscopy and Radiative Transfer* **2020,** *244*, 106839.
89. Doughty, D. C.; Hill, S. C., Automated aerosol Raman spectrometer for semi-continuous sampling of atmospheric aerosol. *Journal of Quantitative Spectroscopy and Radiative Transfer* **2017,** *188*, 103-117.
90. Or, V. W.; Estillore, A. D.; Tivanski, A. V.; Grassian, V. H., Lab on a tip: atomic force microscopy – photothermal infrared spectroscopy of atmospherically relevant organic/inorganic aerosol particles in the nanometer to micrometer size range. *Analyst* **2018,** *143* (12), 2765-2774.
91. Dazzi, A.; Prater, C. B.; Hu, Q.; Chase, D. B.; Rabolt, J. F.; Marcott, C., AFM-IR: combining atomic force microscopy and infrared spectroscopy for nanoscale chemical characterization. *Appl Spectrosc* **2012,** *66* (12), 1365-84.
92. Dazzi, A.; Prazeres, R.; Glotin, F.; Ortega, J. M., Local infrared microspectroscopy with a subwavelength spatial resolution using an AFM tip as a photothermal sensor. *Optics letters* **2005,** *30*, 2388-90.
93. Lei, Z.; Bliesner, S. E.; Mattson, C. N.; Cooke, M. E.; Olson, N. E.; Chibwe, K.; Albert, J. N. L.; Ault, A. P., Aerosol Acidity Sensing via Polymer Degradation. *Analytical Chemistry* **2020,** *92* (9), 6502-6511.
94. Laskina, O.; Morris, H. S.; Grandquist, J. R.; Qin, Z.; Stone, E. A.; Tivanski, A. V.; Grassian, V. H., Size matters in the water uptake and hygroscopic growth of atmospherically relevant multicomponent aerosol particles. *J Phys Chem A* **2015,** *119* (19), 4489-97.
95. Morris, H. S.; Estillore, A. D.; Laskina, O.; Grassian, V. H.; Tivanski, A. V., Quantifying the Hygroscopic Growth of Individual Submicrometer Particles with Atomic Force Microscopy. *Analytical Chemistry* **2016,** *88* (7), 3647-3654.
96. Slade, J. H.; Ault, A. P.; Bui, A. T.; Ditto, J. C.; Lei, Z.; Bondy, A. L.; Olson, N. E.; Cook, R. D.; Desrochers, S. J.; Harvey, R. M.; Erickson, M. H.; Wallace, H. W.; Alvarez, S. L.; Flynn, J. H.; Boor, B. E.; Petrucci, G. A.; Gentner, D. R.; Griffin, R. J.; Shepson, P. B., Bouncier Particles at Night: Biogenic Secondary Organic Aerosol Chemistry and Sulfate Drive

Diel Variations in the Aerosol Phase in a Mixed Forest. *Environmental Science & Technology* **2019,** *53* (9), 4977-4987.
97. Dazzi, A.; Prater, C. B., AFM-IR: Technology and Applications in Nanoscale Infrared Spectroscopy and Chemical Imaging. *Chem Rev* **2017,** *117* (7), 5146-5173.
98. Morris, H. S.; Grassian, V. H.; Tivanski, A. V., Humidity-dependent surface tension measurements of individual inorganic and organic submicrometre liquid particles. *Chemical Science* **2015,** *6* (5), 3242-3247.
99. Hritz, A. D.; Raymond, T. M.; Dutcher, D. D., A method for the direct measurement of surface tension of collected atmospherically relevant aerosol particles using atomic force microscopy. *Atmos. Chem. Phys.* **2016,** *16* (15), 9761-9769.
100. Mostofa, M. G. Nano Mechanical Machining Using AFM Probe. 2014.
101. Hammiche, A.; Reading, M.; Pollock, H. M.; Song, M.; Hourston, D. J., Localized thermal analysis using a miniaturized resistive probe. *Review of Scientific Instruments* **1996,** *67* (12), 4268-4274.
102. Harding, L.; King, W. P.; Dai, X.; Craig, D. Q. M.; Reading, M., Nanoscale Characterisation and Imaging of Partially Amorphous Materials using Local Thermomechanical Analysis and Heated Tip AFM. *Pharmaceutical Research* **2007,** *24* (11), 2048-2054.
103. Hale, R. C.; Seeley, M. E.; La Guardia, M. J.; Mai, L.; Zeng, E. Y., A Global Perspective on Microplastics. *Journal of Geophysical Research: Oceans* **2020,** *125* (1), e2018JC014719.
104. Li, X.; Zhang, D.; Bai, Y.; Wang, W.; Liang, J.; Cheng, J.-X., Fingerprinting a Living Cell by Raman Integrated Mid-Infrared Photothermal Microscopy. *Analytical Chemistry* **2019,** *91* (16), 10750-10756.
105. Zhang, D.; Li, C.; Zhang, C.; Slipchenko, M. N.; Eakins, G.; Cheng, J.-X., Depth-resolved mid-infrared photothermal imaging of living cells and organisms with submicrometer spatial resolution. *Science Advances* **2016,** *2* (9), e1600521.
106. Takahama, S.; Johnson, A.; Russell, L. M., Quantification of Carboxylic and Carbonyl Functional Groups in Organic Aerosol Infrared Absorbance Spectra. *Aerosol Science and Technology* **2013,** *47* (3), 310-325.
107. Li, C.; Zhang, D.; Slipchenko, M. N.; Cheng, J.-X., Mid-Infrared Photothermal Imaging of Active Pharmaceutical Ingredients at Submicrometer Spatial Resolution. *Analytical Chemistry* **2017,** *89* (9), 4863-4867.
108. Furstenberg, R.; Kendziora, C. A.; Papantonakis, M. R.; Nguyen, V.; McGill, R. A. In *Chemical imaging using infrared photothermal microspectroscopy*, June 01, 2012; 2012; p 837411.
109. Gentner, D. R.; Jathar, S. H.; Gordon, T. D.; Bahreini, R.; Day, D. A.; El Haddad, I.; Hayes, P. L.; Pieber, S. M.; Platt, S. M.; de Gouw, J.; Goldstein, A. H.; Harley, R. A.; Jimenez, J. L.; Prévôt, A. S. H.; Robinson, A. L., Review of Urban Secondary Organic Aerosol Formation from Gasoline and Diesel Motor Vehicle Emissions. *Environ. Sci. Technol.* **2017,** *51* (3), 1074-1093.
110. Pye, H. O. T.; Nenes, A.; Alexander, B.; Ault, A. P.; Barth, M. C.; Clegg, S. L.; Collett Jr, J. L.; Fahey, K. M.; Hennigan, C. J.; Herrmann, H.; Kanakidou, M.; Kelly, J. T.; Ku, I. T.; McNeill, V. F.; Riemer, N.; Schaefer, T.; Shi, G.; Tilgner, A.; Walker, J. T.; Wang, T.; Weber, R.; Xing, J.; Zaveri, R. A.; Zuend, A., The Acidity of Atmospheric Particles and Clouds. *Atmos. Chem. Phys.* **2020,** *in press*.
111. Kennedy, I. M., The health effects of combustion-generated aerosols. *Proc. Combust. Inst.* **2007,** *31*, 2757-2770.

112. Fitzgerald, E.; Ault, A. P.; Zauscher, M. D.; Mayol-Bracero, O. L.; Prather, K. A., Comparison of the mixing state of long-range transported Asian and African mineral dust. *Atmos. Environ.* **2015,** *115* (0), 19-25.
113. Uno, I.; Eguchi, K.; Yumimoto, K.; Takemura, T.; Shimizu, A.; Uematsu, M.; Liu, Z. Y.; Wang, Z. F.; Hara, Y.; Sugimoto, N., Asian dust transported one full circuit around the globe. *Nature Geosci.* **2009,** *2* (8), 557-560.
114. Seinfeld, J. H.; Pandis, S. N., *Atmospheric chemistry and physics: from air pollution to climate change*. John Wiley & Sons: 2016.
115. Fang, T.; Guo, H. Y.; Zeng, L. H.; Verma, V.; Nenes, A.; Weber, R. J., Highly Acidic Ambient Particles, Soluble Metals, and Oxidative Potential: A Link between Sulfate and Aerosol Toxicity. *Environ. Sci. Technol.* **2017,** *51* (5), 2611-2620.
116. Eaves, L. A.; Smeester, L.; Hartwell, H. J.; Lin, Y.-H.; Arashiro, M.; Zhang, Z.; Gold, A.; Surratt, J. D.; Fry, R. C., Isoprene-derived Secondary Organic Aerosol Induces the Expression of micro RNAs (miRNAs) Associated with Inflammatory/Oxidative Stress Response in Lung Cells. *Chem. Res. Toxicol.* **2019**.
117. Fang, T.; Guo, H.; Verma, V.; Peltier, R. E.; Weber, R. J., PM2.5 water-soluble elements in the southeastern United States: automated analytical method development, spatiotemporal distributions, source apportionment, and implications for heath studies. *Atmos. Chem. Phys.* **2015,** *15* (20), 11667-11682.
118. Wang, G.; Zhang, R.; Gomez, M. E.; Yang, L.; Zamora, M. L.; Hu, M.; Lin, Y.; Peng, J.; Guo, S.; Meng, J.; Li, J.; Cheng, C.; Hu, T.; Ren, Y.; Wang, Y.; Gao, J.; Cao, J.; An, Z.; Zhou, W.; Li, G.; Wang, J.; Tian, P.; Marrero-Ortiz, W.; Secrest, J.; Du, Z.; Zheng, J.; Shang, D.; Zeng, L.; Shao, M.; Wang, W.; Huang, Y.; Wang, Y.; Zhu, Y.; Li, Y.; Hu, J.; Pan, B.; Cai, L.; Cheng, Y.; Ji, Y.; Zhang, F.; Rosenfeld, D.; Liss, P. S.; Duce, R. A.; Kolb, C. E.; Molina, M. J., Persistent sulfate formation from London Fog to Chinese haze. *Proc. Natl. Acad. Sci. U. S. A.* **2016,** *113* (48), 13630-13635.
119. Guo, H.; Weber, R. J.; Nenes, A., High levels of ammonia do not raise fine particle pH sufficiently to yield nitrogen oxide-dominated sulfate production. *Sci. Rep.* **2017,** *7*, 7.
120. Lin, Y. H.; Zhang, H. F.; Pye, H. O. T.; Zhang, Z. F.; Marth, W. J.; Park, S.; Arashiro, M.; Cui, T. Q.; Budisulistiorini, H.; Sexton, K. G.; Vizuete, W.; Xie, Y.; Luecken, D. J.; Piletic, I. R.; Edney, E. O.; Bartolotti, L. J.; Gold, A.; Surratt, J. D., Epoxide as a precursor to secondary organic aerosol formation from isoprene photooxidation in the presence of nitrogen oxides. *Proc. Natl. Acad. Sci. U. S. A.* **2013,** *110* (17), 6718-6723.
121. Lin, Y. H.; Zhang, Z. F.; Docherty, K. S.; Zhang, H. F.; Budisulistiorini, S. H.; Rubitschun, C. L.; Shaw, S. L.; Knipping, E. M.; Edgerton, E. S.; Kleindienst, T. E.; Gold, A.; Surratt, J. D., Isoprene Epoxydiols as Precursors to Secondary Organic Aerosol Formation: Acid-Catalyzed Reactive Uptake Studies with Authentic Compounds. *Environ. Sci. Technol.* **2012,** *46* (1), 250-258.
122. Jang, M.; Czoschke, N. M.; Lee, S.; Kamens, R. M., Heterogeneous Atmospheric Aerosol Production by Acid-Catalyzed Particle-Phase Reactions. *Science* **2002,** *298* (5594), 814-817.
123. Surratt, J. D.; Chan, A. W. H.; Eddingsaas, N. C.; Chan, M. N.; Loza, C. L.; Kwan, A. J.; Hersey, S. P.; Flagan, R. C.; Wennberg, P. O.; Seinfeld, J. H., Reactive intermediates revealed in secondary organic aerosol formation from isoprene. *Proc. Natl. Acad. Sci. U. S. A.* **2010,** *107* (15), 6640-6645.

124. Jang, M.; Carroll, B.; Chandramouli, B.; Kamens, R. M., Particle growth by acid-catalyzed heterogeneous reactions of organic carbonyls on preexisting aerosols. *Environ. Sci. Technol.* **2003,** *37* (17), 3828-3837.
125. Riva, M.; Bell, D. M.; Hansen, A. M. K.; Drozd, G. T.; Zhang, Z. F.; Gold, A.; Imre, D.; Surratt, J. D.; Glasius, M.; Zelenyuk, A., Effect of Organic Coatings, Humidity and Aerosol Acidity on Multiphase Chemistry of Isoprene Epoxydiols. *Environ. Sci. Technol.* **2016,** *50* (11), 5580-5588.
126. Gaston, C. J.; Riedel, T. P.; Zhang, Z. F.; Gold, A.; Surratt, J. D.; Thornton, J. A., Reactive Uptake of an Isoprene-Derived Epoxydiol to Submicron Aerosol Particles. *Environ. Sci. Technol.* **2014,** *48* (19), 11178-11186.
127. Prenni, A. J.; DeMott, P. J.; Kreidenweis, S. M., Water uptake of internally mixed particles containing ammonium sulfate and dicarboxylic acids. *Atmos. Environ.* **2003,** *37* (30), 4243-4251.
128. Ghorai, S.; Laskin, A.; Tivanski, A. V., Spectroscopic Evidence of Keto-Enol Tautomerism in Deliquesced Malonic Acid Particles. *J. Phys. Chem. A* **2011,** *115* (17), 4373-4380.
129. Losey, D. J.; Parker, R. G.; Freedman, M. A., pH Dependence of Liquid–Liquid Phase Separation in Organic Aerosol. *J. Phys. Chem. Lett.* **2016,** *7* (19), 3861-3865.
130. You, Y.; Smith, M. L.; Song, M.; Martin, S. T.; Bertram, A. K., Liquid–liquid phase separation in atmospherically relevant particles consisting of organic species and inorganic salts. *Int. Rev. Phys. Chem.* **2014,** *33* (1), 43-77.
131. Feng, J.; Guo, Z.; Zhang, T.; Yao, X.; Chan, C.-K.; Fang, M., Source and formation of secondary particulate matter in PM2. 5 in Asian continental outflow. *J. Geophys. Res.: Atmos.* **2012,** *117* (D3).
132. Hennigan, C. J.; Izumi, J.; Sullivan, A. P.; Weber, R. J.; Nenes, A., A critical evaluation of proxy methods used to estimate the acidity of atmospheric particles. *Atmos. Chem. Phys.* **2015,** *15* (5), 2775-2790.
133. Guo, H.; Xu, L.; Bougiatioti, A.; Cerully, K. M.; Capps, S. L.; Hite, J. R., Jr.; Carlton, A. G.; Lee, S. H.; Bergin, M. H.; Ng, N. L.; Nenes, A.; Weber, R. J., Fine-particle water and pH in the southeastern United States. *Atmos. Chem. Phys.* **2015,** *15* (9), 5211-5228.
134. Trebs, I.; Metzger, S.; Meixner, F. X.; Helas, G.; Hoffer, A.; Rudich, Y.; Falkovich, A. H.; Moura, M. A.; da Silva Jr, R. S.; Artaxo, P., The NH4+-NO3−-Cl−-SO42−-H2O aerosol system and its gas phase precursors at a pasture site in the Amazon Basin: How relevant are mineral cations and soluble organic acids? *J. Geophys. Res.: Atmos.* **2005,** *110* (D7).
135. Brauer, M.; Koutrakis, P.; Keeler, G. J.; Spengler, J. D., Indoor and Outdoor Concentrations of Inorganic Acidic Aerosols and Gases. *J. Air Waste Manage.* **1991,** *41* (2), 171-181.
136. Koutrakis, P.; Wolfson, J. M.; Slater, J. L.; Brauer, M.; Spengler, J. D.; Stevens, R. K.; Stone, C. L., Evaluation of an annular denuder/filter pack system to collect acidic aerosols and gases. *Environ. Sci. Technol.* **1988,** *22* (12), 1463-1468.
137. Weber, R. J.; Guo, H. Y.; Russell, A. G.; Nenes, A., High aerosol acidity despite declining atmospheric sulfate concentrations over the past 15 years. *Nature Geosci.* **2016,** *9* (4), 282-285.
138. Bougiatioti, A.; Nikolaou, P.; Stavroulas, I.; Kouvarakis, G.; Weber, R.; Nenes, A.; Kanakidou, M.; Mihalopoulos, N., Particle water and pH in the eastern Mediterranean: source variability and implications for nutrient availability. *Atmos. Chem. Phys.* **2016,** *16* (7), 4579-4591.
139. Tao, Y.; Murphy, J. G., The sensitivity of PM2.5 acidity to meteorological parameters and chemical composition changes: 10-year records from six Canadian monitoring sites. *Atmos. Chem. Phys.* **2019,** *19* (14), 9309-9320.

140. Riva, M.; Chen, Y.; Zhang, Y.; Lei, Z.; Olson, N.; Boyer, H. C.; Narayan, S.; Yee, L. D.; Green, H.; Cui, T.; Zhang, Z.; Baumann, K. D.; Fort, M.; Edgerton, E. S.; Budisulistiorini, S.; Rose, C. A.; Ribeiro, I.; e Oliveira, R. L.; Santos, E.; Szopa, S.; Machado, C.; Zhao, Y.; Alves, E.; de Sa, S.; Hu, W.; Knipping, E.; Shaw, S.; Duvoisin Junior, S.; Souza, R. A. F. d.; Palm, B. B.; Jimenez, J. L.; Glasius, M.; Goldstein, A. H.; Pye, H. O. T.; Gold, A.; Turpin, B. J.; Vizuete, W.; Martin, S. T.; Thornton, J.; Dutcher, C. S.; Ault, A. P.; Surratt, J. D., Increasing Isoprene Epoxydiol-to-Inorganic Sulfate Aerosol (IEPOX:Sulfinorg) Ratio Results in Extensive Conversion of Inorganic Sulfate to Organosulfur Forms: Implications for Aerosol Physicochemical Properties. *Environ. Sci. Technol.* **2019**.
141. Guo, H.; Sullivan, A. P.; Campuzano-Jost, P.; Schroder, J. C.; Lopez-Hilfiker, F. D.; Dibb, J. E.; Jimenez, J. L.; Thornton, J. A.; Brown, S. S.; Nenes, A., Fine particle pH and the partitioning of nitric acid during winter in the northeastern United States. *J. Geophys. Res.: Atmos.* **2016,** *121* (17).
142. Bougiatioti, A.; Nikolaou, P.; Stavroulas, I.; Kouvarakis, G.; Weber, R.; Nenes, A.; Kanakidou, M.; Mihalopoulos, N., Particle water and pH in the eastern Mediterranean: source variability and implications for nutrient availability. *Atmos. Chem. Phys.* **2016,** *16* (7), 4579-4591.
143. Battaglia Jr, M. A.; Douglas, S.; Hennigan, C. J., Effect of the urban heat island on aerosol pH. *Environ. Sci. Technol.* **2017,** *51* (22), 13095-13103.
144. Liu, M.; Song, Y.; Zhou, T.; Xu, Z.; Yan, C.; Zheng, M.; Wu, Z.; Hu, M.; Wu, Y.; Zhu, T., Fine particle pH during severe haze episodes in northern China. *Geophys. Res. Lett.* **2017,** *44* (10), 5213-5221.
145. Craig, R. L.; Ault, A. P., Aerosol Acidity: Direct Measurement from a Spectroscopic Method. In *Multiphase Environmental Chemistry in the Atmosphere*, American Chemical Society: 2018; Vol. 1299, pp 171-191.
146. Kroll, J. H.; Seinfeld, J. H., Chemistry of secondary organic aerosol: Formation and evolution of low-volatility organics in the atmosphere. *Atmospheric Environment* **2008,** *42* (16), 3593-3624.
147. Craig, R. L.; Peterson, P. K.; Nandy, L.; Lei, Z.; Hossain, M. A.; Camarena, S.; Dodson, R. A.; Cook, R. D.; Dutcher, C. S.; Ault, A. P., Direct Determination of Aerosol pH: Size-Resolved Measurements of Submicrometer and Supermicrometer Aqueous Particles. *Anal. Chem.* **2018**.
148. Riemer, N.; Ault, A. P.; West, M.; Craig, R. L.; Curtis, J. H., Aerosol Mixing State: Measurements, Modeling, and Impacts. *Rev. Geophys.* **2019,** *57* (2), 187-249.
149. Bauer, S. E.; Ault, A.; Prather, K. A., Evaluation of aerosol mixing state classes in the GISS modelE-MATRIX climate model using single-particle mass spectrometry measurements. *J. Geophys. Res.: Atmos.* **2013,** *118* (17), 9834-9844.
150. Bondy, A. L.; Bonanno, D.; Moffet, R. C.; Wang, B.; Laskin, A.; Ault, A. P., The diverse chemical mixing state of aerosol particles in the southeastern United States. *Atmos. Chem. Phys.* **2018,** *18* (16), 12595-12612.
151. Li, S.; Vert, M., Biodegradation of Aliphatic Polyesters. 1995; pp 43-87.
152. Tserki, V.; Matzinos, P.; Pavlidou, E.; Vachliotis, D.; Panayiotou, C., Biodegradable aliphatic polyesters. Part I. Properties and biodegradation of poly(butylene succinate-co-butylene adipate). *Polymer Degradation and Stability* **2006,** *91* (2), 367-376.
153. Woodruff, M. A.; Hutmacher, D. W., The return of a forgotten polymer—Polycaprolactone in the 21st century. *Prog. Polym. Sci.* **2010,** *35* (10), 1217-1256.

154. Li, S., Hydrolytic degradation characteristics of aliphatic polyesters derived from lactic and glycolic acids. *J. Biomed. Mater. Res.* **1999,** *48* (3), 342-353.
155. Jung, J. H.; Ree, M.; Kim, H., Acid- and base-catalyzed hydrolyses of aliphatic polycarbonates and polyesters. *Catal. Today* **2006,** *115* (1-4), 283-287.
156. Freedman, M. A.; Ott, E.-J. E.; Marak, K. E., Role of pH in Aerosol Processes and Measurement Challenges. *J. Phys. Chem. A* **2019,** *123* (7), 1275-1284.
157. Kelly, G. M.; Albert, J. N. L., Ultrathin film crystallization of poly(ε-caprolactone) in blends containing styrene-isoprene block copolymers: The nano-rose morphology. *Polymer* **2017,** *117*, 295-305.
158. Ma, M.; He, Z.; Yang, J.; Chen, F.; Wang, K.; Zhang, Q.; Deng, H.; Fu, Q., Effect of Film Thickness on Morphological Evolution in Dewetting and Crystallization of Polystyrene/Poly(ε-caprolactone) Blend Films. *Langmuir* **2011,** *27* (21), 13072-13081.
159. Reiter, G., Unstable thin polymer films: rupture and dewetting processes. *Langmuir* **1993,** *9* (5), 1344-1351.
160. Nenes, A.; Krom, M. D.; Mihalopoulos, N.; Van Cappellen, P.; Shi, Z.; Bougiatioti, A.; Zarmpas, P.; Herut, B., Atmospheric acidification of mineral aerosols: a source of bioavailable phosphorus for the oceans. *Atmos. Chem. Phys.* **2011,** *11* (13), 6265-6272.
161. Sobanska, S.; Falgayrac, G.; Rimetz-Planchon, J.; Perdrix, E.; Bremard, C.; Barbillat, J., Resolving the internal structure of individual atmospheric aerosol particle by the combination of Atomic Force Microscopy, ESEM-EDX, Raman and ToF-SIMS imaging. *Microchem J.* **2014,** *114*, 89-98.
162. Ray, K. K.; Lee, H. D.; Gutierrez, M. A.; Chang, F. J.; Tivanski, A. V., Correlating 3D Morphology, Phase State, and Viscoelastic Properties of Individual Substrate-Deposited Particles. *Analytical Chemistry* **2019,** *91* (12), 7621-7630.
163. Imre, D. G.; Xu, J.; Tang, I.; McGraw, R., Ammonium bisulfate/water equilibrium and metastability phase diagrams. *J. Phys. Chem. A* **1997,** *101* (23), 4191-4195.
164. Cziczo, D.; Abbatt, J., Deliquescence, efflorescence, and supercooling of ammonium sulfate aerosols at low temperature: Implications for cirrus cloud formation and aerosol phase in the atmosphere. *J. Geophys. Res.: Atmos.* **1999,** *104* (D11), 13781-13790.
165. Tang, I.; Fung, K.; Imre, D.; Munkelwitz, H., Phase transformation and metastability of hygroscopic microparticles. *Aerosol Sci. Technol.* **1995,** *23* (3), 443-453.
166. Onasch, T. B.; Siefert, R. L.; Brooks, S. D.; Prenni, A. J.; Murray, B.; Wilson, M. A.; Tolbert, M. A., Infrared spectroscopic study of the deliquescence and efflorescence of ammonium sulfate aerosol as a function of temperature. *Journal of Geophysical Research: Atmospheres* **1999,** *104* (D17), 21317-21326.
167. Ault, A. P.; Guasco, T. L.; Baltrusaitis, J.; Ryder, O. S.; Trueblood, J. V.; Collins, D. B.; Ruppel, M. J.; Cuadra-Rodriguez, L. A.; Prather, K. A.; Grassian, V. H., Heterogeneous reactivity of nitric acid with nascent sea spray aerosol: large differences observed between and within individual particles. *J. Phys. Chem. Lett.* **2014**, 2493-2500.
168. Bondy, A. L.; Craig, R. L.; Zhang, Z.; Gold, A.; Surratt, J. D.; Ault, A. P., Isoprene-Derived Organosulfates: Vibrational Mode Analysis by Raman Spectroscopy, Acidity-Dependent Spectral Modes, and Observation in Individual Atmospheric Particles. *The Journal of Physical Chemistry A* **2018,** *122* (1), 303-315.
169. Tirella, P. N.; Craig, R. L.; Tubbs, D. B.; Olson, N. E.; Lei, Z.; Ault, A., Extending Surface Enhanced Raman Spectroscopy (SERS) of Atmospheric Aerosol Particles to the Accumulation Mode (150-800 nm). *Environ. Sci.: Processes Impacts* **2018**.

170. Slade, J. H.; Ault, A. P.; Bui, A. T.; Ditto, J. C.; Lei, Z.; Bondy, A. L.; Olson, N. E.; Cook, R. D.; Desrochers, S. J.; Harvey, R. M.; Erickson, M. H.; Wallace, H. W.; Alvarez, S. L.; Flynn, J. H.; Boor, B. E.; Petrucci, G. A.; Gentner, D. R.; Griffin, R. J.; Shepson, P. B., Bouncier Particles at Night: Biogenic Secondary Organic Aerosol Chemistry and Sulfate Drive Diel Variations in the Aerosol Phase in a Mixed Forest. *Environ. Sci. Technol.* **2019**.
171. Hernández, A. R.; Contreras, O. C.; Acevedo, J. C.; Moreno, L. G. N., Poly (ε-caprolactone) degradation under acidic and alkaline conditions. *Am. J. Polym. Sci,* **2013,** *3*, 70-75.
172. Zhang, Y.; Chen, Y.; Lei, Z.; Olson, N.; Riva, M.; Koss, A. R.; Zhang, Z.; Gold, A.; Jayne, J. T.; Worsnop, D. R.; Onasch, T. B.; Kroll, J. H.; Turpin, B. J.; Ault, A. P.; Surratt, J. D., Joint Impacts of Acidity and Viscosity on the Formation of Secondary Organic Aerosol from Isoprene Epoxydiols (IEPOX) in Phase Separated Particles. *ACS Earth Space Chem.* **2019,** *3* (12), 2646-2658.
173. Carlton, A. M.; Wiedinmyer, C.; Kroll, J., A review of Secondary Organic Aerosol (SOA) formation from isoprene. *Atmospheric Chemistry and Physics* **2009,** *9*.
174. Surratt, J. D.; Chan, A. W. H.; Eddingsaas, N. C.; Chan, M.; Loza, C. L.; Kwan, A. J.; Hersey, S. P.; Flagan, R. C.; Wennberg, P. O.; Seinfeld, J. H., Reactive intermediates revealed in secondary organic aerosol formation from isoprene. *Proceedings of the National Academy of Sciences* **2010,** *107* (15), 6640.
175. Surratt, J. D.; Gómez-González, Y.; Chan, A. W. H.; Vermeylen, R.; Shahgholi, M.; Kleindienst, T. E.; Edney, E. O.; Offenberg, J. H.; Lewandowski, M.; Jaoui, M.; Maenhaut, W.; Claeys, M.; Flagan, R. C.; Seinfeld, J. H., Organosulfate Formation in Biogenic Secondary Organic Aerosol. *The Journal of Physical Chemistry A* **2008,** *112* (36), 8345-8378.
176. Zhang, Y.; Katira, S.; Lee, A.; Lambe, A. T.; Onasch, T. B.; Xu, W.; Brooks, W. A.; Canagaratna, M. R.; Freedman, A.; Jayne, J. T.; Worsnop, D. R.; Davidovits, P.; Chandler, D.; Kolb, C. E., Kinetically controlled glass transition measurement of organic aerosol thin films using broadband dielectric spectroscopy. *Atmos. Meas. Tech.* **2018,** *11* (6), 3479-3490.
177. Zhang, Y.; Nichman, L.; Spencer, P.; Jung, J. I.; Lee, A.; Heffernan, B. K.; Gold, A.; Zhang, Z.; Chen, Y.; Canagaratna, M. R.; Jayne, J. T.; Worsnop, D. R.; Onasch, T. B.; Surratt, J. D.; Chandler, D.; Davidovits, P.; Kolb, C. E., The Cooling Rate- and Volatility-Dependent Glass-Forming Properties of Organic Aerosols Measured by Broadband Dielectric Spectroscopy. *Environmental Science & Technology* **2019,** *53* (21), 12366-12378.
178. Renbaum-Wolff, L.; Grayson, J. W.; Bateman, A. P.; Kuwata, M.; Sellier, M.; Murray, B. J.; Shilling, J. E.; Martin, S. T.; Bertram, A. K., Viscosity of α-pinene secondary organic material and implications for particle growth and reactivity. *Proceedings of the National Academy of Sciences* **2013,** *110* (20), 8014.
179. Hatch, L. E.; Creamean, J. M.; Ault, A. P.; Surratt, J. D.; Chan, M. N.; Seinfeld, J. H.; Edgerton, E. S.; Su, Y. X.; Prather, K. A., Measurements of Isoprene-Derived Organosulfates in Ambient Aerosols by Aerosol Time-of-Flight Mass Spectrometry-Part 2: Temporal Variability and Formation Mechanisms. *Environ. Sci. Technol.* **2011,** *45* (20), 8648-8655.
180. Surratt, J. D.; Kroll, J. H.; Kleindienst, T. E.; Edney, E. O.; Claeys, M.; Sorooshian, A.; Ng, N. L.; Offenberg, J. H.; Lewandowski, M.; Jaoui, M.; Flagan, R. C.; Seinfeld, J. H., Evidence for organosulfates in secondary organic aerosol. *Environ. Sci. Technol.* **2007,** *41* (2), 517-527.
181. Hettiyadura, A. P. S.; Al-Naiema, I. M.; Hughes, D. D.; Fang, T.; Stone, E. A., Organosulfates in Atlanta, Georgia: anthropogenic influences on biogenic secondary organic aerosol formation. *Atmos. Chem. Phys.* **2019,** *19* (5), 3191-3206.

182. Li, Y.; Day, D. A.; Stark, H.; Jimenez, J. L.; Shiraiwa, M., Predictions of the glass transition temperature and viscosity of organic aerosols from volatility distributions. *Atmos. Chem. Phys.* **2020,** *20* (13), 8103-8122.
183. Tikkanen, O. P.; Hämäläinen, V.; Rovelli, G.; Lipponen, A.; Shiraiwa, M.; Reid, J. P.; Lehtinen, K. E. J.; Yli-Juuti, T., Optimization of process models for determining volatility distribution and viscosity of organic aerosols from isothermal particle evaporation data. *Atmos. Chem. Phys.* **2019,** *19* (14), 9333-9350.
184. DeRieux, W. S. W.; Li, Y.; Lin, P.; Laskin, J.; Laskin, A.; Bertram, A. K.; Nizkorodov, S. A.; Shiraiwa, M., Predicting the glass transition temperature and viscosity of secondary organic material using molecular composition. *Atmos. Chem. Phys.* **2018,** *18* (9), 6331-6351.
185. Marcolli, C.; Krieger, U. K., Relevance of Particle Morphology for Atmospheric Aerosol Processing. *Trends in Chemistry* **2020,** *2* (1), 1-3.
186. Järvinen, E.; Ignatius, K.; Nichman, L.; Kristensen, T.; Fuchs, C.; Höppel, N.; Corbin, J.; Craven, J.; Duplissy, J.; Ehrhart, S.; Haddad, I.; Frege, C.; Gates, S.; Gordon, H.; Hoyle, C.; Jokinen, T.; Kallinger, P.; Kirkby, J.; Kiselev, A.; Schnaiter, M., Observation of viscosity transition in α-pinene secondary organic aerosol. *Atmospheric Chemistry and Physics Discussions* **2015,** *15*, 28575-28617.
187. Zhang, Y.; Sanchez, M. S.; Douet, C.; Wang, Y.; Bateman, A. P.; Gong, Z.; Kuwata, M.; Renbaum-Wolff, L.; Sato, B. B.; Liu, P. F.; Bertram, A. K.; Geiger, F. M.; Martin, S. T., Changing shapes and implied viscosities of suspended submicron particles. *Atmos. Chem. Phys.* **2015,** *15* (14), 7819-7829.
188. Kwamena, N. O. A.; Buajarern, J.; Reid, J. P., Equilibrium Morphology of Mixed Organic/Inorganic/Aqueous Aerosol Droplets: Investigating the Effect of Relative Humidity and Surfactants. *The Journal of Physical Chemistry A* **2010,** *114* (18), 5787-5795.
189. O'Brien, R. E.; Neu, A.; Epstein, S. A.; MacMillan, A. C.; Wang, B.; Kelly, S. T.; Nizkorodov, S. A.; Laskin, A.; Moffet, R. C.; Gilles, M. K., Physical properties of ambient and laboratory-generated secondary organic aerosol. *Geophysical Research Letters* **2014,** *41* (12), 4347-4353.
190. Carlton, A. G.; Wiedinmyer, C.; Kroll, J. H., A review of Secondary Organic Aerosol (SOA) formation from isoprene. *Atmos. Chem. Phys.* **2009,** *9* (14), 4987-5005.
191. Tsigaridis, K.; Daskalakis, N.; Kanakidou, M.; Adams, P. J.; Artaxo, P.; Bahadur, R.; Balkanski, Y.; Bauer, S. E.; Bellouin, N.; Benedetti, A.; Bergman, T.; Berntsen, T. K.; Beukes, J. P.; Bian, H.; Carslaw, K. S.; Chin, M.; Curci, G.; Diehl, T.; Easter, R. C.; Ghan, S. J.; Gong, S. L.; Hodzic, A.; Hoyle, C. R.; Iversen, T.; Jathar, S.; Jimenez, J. L.; Kaiser, J. W.; Kirkevåg, A.; Koch, D.; Kokkola, H.; Lee, Y. H.; Lin, G.; Liu, X.; Luo, G.; Ma, X.; Mann, G. W.; Mihalopoulos, N.; Morcrette, J. J.; Müller, J. F.; Myhre, G.; Myriokefalitakis, S.; Ng, N. L.; O'Donnell, D.; Penner, J. E.; Pozzoli, L.; Pringle, K. J.; Russell, L. M.; Schulz, M.; Sciare, J.; Seland, Ø.; Shindell, D. T.; Sillman, S.; Skeie, R. B.; Spracklen, D.; Stavrakou, T.; Steenrod, S. D.; Takemura, T.; Tiitta, P.; Tilmes, S.; Tost, H.; van Noije, T.; van Zyl, P. G.; von Salzen, K.; Yu, F.; Wang, Z.; Wang, Z.; Zaveri, R. A.; Zhang, H.; Zhang, K.; Zhang, Q.; Zhang, X., The AeroCom evaluation and intercomparison of organic aerosol in global models. *Atmos. Chem. Phys.* **2014,** *14* (19), 10845-10895.
192. Zheng, G.; Su, H.; Wang, S.; Andreae, M. O.; Pöschl, U.; Cheng, Y., Multiphase buffer theory explains contrasts in atmospheric aerosol acidity. *Science* **2020,** *369* (6509), 1374-1377.
193. Lambe, A. T.; Ahern, A. T.; Williams, L. R.; Slowik, J. G.; Wong, J. P. S.; Abbatt, J. P. D.; Brune, W. H.; Ng, N. L.; Wright, J. P.; Croasdale, D. R.; Worsnop, D. R.; Davidovits, P.;

Onasch, T. B., Characterization of aerosol photooxidation flow reactors: heterogeneous oxidation, secondary organic aerosol formation and cloud condensation nuclei activity measurements. *Atmos. Meas. Tech.* **2011,** *4* (3), 445-461.
194. Riva, M.; Budisulistiorini, S. H.; Zhang, Z.; Gold, A.; Surratt, J. D., Chemical characterization of secondary organic aerosol constituents from isoprene ozonolysis in the presence of acidic aerosol. *Atmospheric Environment* **2016,** *130*, 5-13.
195. Zhang, Z.; Lin, Y. H.; Zhang, H.; Surratt, J. D.; Ball, L. M.; Gold, A., Technical Note: Synthesis of isoprene atmospheric oxidation products: isomeric epoxydiols and the rearrangement products *cis*- and *trans*-3-methyl-3,4-dihydroxytetrahydrofuran. *Atmos. Chem. Phys.* **2012,** *12* (18), 8529-8535.
196. Riedel, T. P.; Lin, Y.-H.; Budisulistiorini, S. H.; Gaston, C. J.; Thornton, J. A.; Zhang, Z.; Vizuete, W.; Gold, A.; Surratt, J. D., Heterogeneous Reactions of Isoprene-Derived Epoxides: Reaction Probabilities and Molar Secondary Organic Aerosol Yield Estimates. *Environmental Science & Technology Letters* **2015,** *2* (2), 38-42.
197. Champion, W. M.; Rothfuss, N. E.; Petters, M. D.; Grieshop, A. P., Volatility and Viscosity Are Correlated in Terpene Secondary Organic Aerosol Formed in a Flow Reactor. *Environmental Science & Technology Letters* **2019,** *6* (9), 513-519.
198. Robinson, E. S.; Saleh, R.; Donahue, N. M., Probing the Evaporation Dynamics of Mixed SOA/Squalane Particles Using Size-Resolved Composition and Single-Particle Measurements. *Environmental Science & Technology* **2015,** *49* (16), 9724-9732.
199. Gao, S.; Keywood, M.; Ng, N. L.; Surratt, J.; Varutbangkul, V.; Bahreini, R.; Flagan, R. C.; Seinfeld, J. H., Low-Molecular-Weight and Oligomeric Components in Secondary Organic Aerosol from the Ozonolysis of Cycloalkenes and α-Pinene. *The Journal of Physical Chemistry A* **2004,** *108* (46), 10147-10164.
200. Docherty, K. S.; Wu, W.; Lim, Y. B.; Ziemann, P. J., Contributions of Organic Peroxides to Secondary Aerosol Formed from Reactions of Monoterpenes with O3. *Environmental Science & Technology* **2005,** *39* (11), 4049-4059.
201. Witkowski, B.; Gierczak, T., Early stage composition of SOA produced by α-pinene/ozone reaction: α-Acyloxyhydroperoxy aldehydes and acidic dimers. *Atmospheric Environment* **2014,** *95*, 59-70.
202. Kundu, S.; Fisseha, R.; Putman, A. L.; Rahn, T. A.; Mazzoleni, L. R., Molecular formula composition of β-caryophyllene ozonolysis SOA formed in humid and dry conditions. *Atmospheric Environment* **2017,** *154*, 70-81.
203. Kanawati, B.; Herrmann, F.; Joniec, S.; Winterhalter, R.; Moortgat, G., Mass spectrometric characterization of β -caryophyllene ozonolysis products in the aerosol studied using an electrospray triple quadrupole and time-of-flight analyzer hybrid system and density functional theory. *Rapid communications in mass spectrometry : RCM* **2008,** *22*, 165-86.
204. Kahnt, A.; Vermeylen, R.; Iinuma, Y.; Safi Shalamzari, M.; Maenhaut, W.; Claeys, M., High-molecular-weight esters in α-pinene ozonolysis secondary organic aerosol: structural characterization and mechanistic proposal for their formation from highly oxygenated molecules. *Atmos. Chem. Phys.* **2018,** *18* (11), 8453-8467.
205. D'Ambro, E. L.; Lee, B. H.; Liu, J.; Shilling, J. E.; Gaston, C. J.; Lopez-Hilfiker, F. D.; Schobesberger, S.; Zaveri, R. A.; Mohr, C.; Lutz, A.; Zhang, Z.; Gold, A.; Surratt, J. D.; Rivera-Rios, J. C.; Keutsch, F. N.; Thornton, J. A., Molecular composition and volatility of isoprene photochemical oxidation secondary organic aerosol under low- and high-NOx conditions. *Atmos. Chem. Phys.* **2017,** *17* (1), 159-174.

206. Surratt, J. D.; Chan, A. W. H.; Eddingsaas, N. C.; Chan, M.; Loza, C. L.; Kwan, A. J.; Hersey, S. P.; Flagan, R. C.; Wennberg, P. O.; Seinfeld, J. H., Reactive intermediates revealed in secondary organic aerosol formation from isoprene. *Proceedings of the National Academy of Sciences* **2010,** *107* (15), 6640-6645.
207. Song, M.; Liu, P. F.; Hanna, S. J.; Martin, S. T.; Bertram, A. K., Relative humidity-dependent viscosities of isoprene-derived secondary organic material and atmospheric implications for isoprene-dominant forests. *Atmospheric Chemistry and Physics Discussions* **2015,** *15* (1), 1131-1169.
208. Budisulistiorini, S. H.; Nenes, A.; Carlton, A. G.; Surratt, J. D.; McNeill, V. F.; Pye, H. O. T., Simulating Aqueous-Phase Isoprene-Epoxydiol (IEPOX) Secondary Organic Aerosol Production During the 2013 Southern Oxidant and Aerosol Study (SOAS). *Environmental Science & Technology* **2017,** *51* (9), 5026-5034.
209. Surratt, J. D.; Chan, A. W.; Eddingsaas, N. C.; Chan, M.; Loza, C. L.; Kwan, A. J.; Hersey, S. P.; Flagan, R. C.; Wennberg, P. O.; Seinfeld, J. H., Reactive intermediates revealed in secondary organic aerosol formation from isoprene. *Proc Natl Acad Sci U S A* **2010,** *107* (15), 6640-5.
210. Riva, M.; Bell, D. M.; Hansen, A.-M. K.; Drozd, G. T.; Zhang, Z.; Gold, A.; Imre, D.; Surratt, J. D.; Glasius, M.; Zelenyuk, A., Effect of Organic Coatings, Humidity and Aerosol Acidity on Multiphase Chemistry of Isoprene Epoxydiols. *Environmental Science & Technology* **2016,** *50* (11), 5580-5588.
211. Ault, A. P.; Zhao, D.; Ebben, C. J.; Tauber, M. J.; Geiger, F. M.; Prather, K. A.; Grassian, V. H., Raman microspectroscopy and vibrational sum frequency generation spectroscopy as probes of the bulk and surface compositions of size-resolved sea spray aerosol particles. *Phys Chem Chem Phys* **2013,** *15* (17), 6206-14.
212. Venkateswarlu, P.; Bist, H. D.; Jain, Y. S., Laser excited Raman spectrum of ammonium sulfate single crystal. *Journal of Raman Spectroscopy* **1975,** *3* (2-3), 143-151.
213. Vargas Jentzsch, P.; Kampe, B.; Ciobota, V.; Rosch, P.; Popp, J., Inorganic salts in atmospheric particulate matter: Raman spectroscopy as an analytical tool. *Spectrochim Acta A Mol Biomol Spectrosc* **2013,** *115*, 697-708.
214. Sobanska, S.; Hwang, H.; Choël, M.; Jung, H.-J.; Eom, H.-J.; Kim, H.; Barbillat, J.; Ro, C.-U., Investigation of the Chemical Mixing State of Individual Asian Dust Particles by the Combined Use of Electron Probe X-ray Microanalysis and Raman Microspectrometry. *Analytical Chemistry* **2012,** *84* (7), 3145-3154.
215. Zhou, Q.; Pang, S.-F.; Wang, Y.; Ma, J.-B.; Zhang, Y.-H., Confocal Raman Studies of the Evolution of the Physical State of Mixed Phthalic Acid/Ammonium Sulfate Aerosol Droplets and the Effect of Substrates. *The Journal of Physical Chemistry B* **2014,** *118* (23), 6198-6205.
216. Hyttinen, N.; Elm, J.; Malila, J.; Calderón, S. M.; Prisle, N. L., Thermodynamic properties of isoprene- and monoterpene-derived organosulfates estimated with COSMOtherm. *Atmos. Chem. Phys.* **2020,** *20* (9), 5679-5696.
217. Larkin, P., *Infrared and raman spectroscopy : principles and spectral interpretation / Peter Larkin*. Amsterdam
Boston : Elsevier, c2011.: Amsterdam
Boston, 2011; p x, 228 p. : ill.
218. Feltracco, M.; Barbaro, E.; Contini, D.; Zangrando, R.; Toscano, G.; Battistel, D.; Barbante, C.; Gambaro, A., Photo-oxidation products of α-pinene in coarse, fine and ultrafine

aerosol: A new high sensitive HPLC-MS/MS method. *Atmospheric Environment* **2018,** *180*, 149-155.
219. Yu, J.; Cocker, D. R.; Griffin, R. J.; Flagan, R. C.; Seinfeld, J. H., Gas-Phase Ozone Oxidation of Monoterpenes: Gaseous and Particulate Products. *Journal of Atmospheric Chemistry* **1999,** *34* (2), 207-258.
220. Cahill, T. M.; Seaman, V. Y.; Charles, M. J.; Holzinger, R.; Goldstein, A. H., Secondary organic aerosols formed from oxidation of biogenic volatile organic compounds in the Sierra Nevada Mountains of California. *Journal of Geophysical Research: Atmospheres* **2006,** *111* (D16).
221. Fankhauser, A. M.; Lei, Z.; Daley, K. R.; Xiao, Y.; Ault, B. S.; Surratt, J. D., Atmospheric Organosulfate Protonation State as a Function of Aerosol Acidity from Raman and Infrared Spectroscopy *in prep* **2021**.
222. Veghte, D. P.; Altaf, M. B.; Freedman, M. A., Size dependence of the structure of organic aerosol. *J Am Chem Soc* **2013,** *135* (43), 16046-9.
223. Pierce, J. R.; Leaitch, W. R.; Liggio, J.; Westervelt, D. M.; Wainwright, C. D.; Abbatt, J. P. D.; Ahlm, L.; Al-Basheer, W.; Cziczo, D. J.; Hayden, K. L.; Lee, A. K. Y.; Li, S. M.; Russell, L. M.; Sjostedt, S. J.; Strawbridge, K. B.; Travis, M.; Vlasenko, A.; Wentzell, J. J. B.; Wiebe, H. A.; Wong, J. P. S.; Macdonald, A. M., Nucleation and condensational growth to CCN sizes during a sustained pristine biogenic SOA event in a forested mountain valley. *Atmos. Chem. Phys.* **2012,** *12* (7), 3147-3163.
224. Wolf, M. J.; Zhang, Y.; Zawadowicz, M. A.; Goodell, M.; Froyd, K.; Freney, E.; Sellegri, K.; Rösch, M.; Cui, T.; Winter, M.; Lacher, L.; Axisa, D.; DeMott, P. J.; Levin, E. J. T.; Gute, E.; Abbatt, J.; Koss, A.; Kroll, J. H.; Surratt, J. D.; Cziczo, D. J., A biogenic secondary organic aerosol source of cirrus ice nucleating particles. *Nature Communications* **2020,** *11* (1), 4834.
225. Murray, B. J.; Wilson, T. W.; Dobbie, S.; Cui, Z.; Al-Jumur, S. M. R. K.; Möhler, O.; Schnaiter, M.; Wagner, R.; Benz, S.; Niemand, M.; Saathoff, H.; Ebert, V.; Wagner, S.; Kärcher, B., Heterogeneous nucleation of ice particles on glassy aerosols under cirrus conditions. *Nature Geoscience* **2010,** *3* (4), 233-237.
226. Ehn, M.; Thornton, J. A.; Kleist, E.; Sipilä, M.; Junninen, H.; Pullinen, I.; Springer, M.; Rubach, F.; Tillmann, R.; Lee, B.; Lopez-Hilfiker, F.; Andres, S.; Acir, I.-H.; Rissanen, M.; Jokinen, T.; Schobesberger, S.; Kangasluoma, J.; Kontkanen, J.; Nieminen, T.; Kurtén, T.; Nielsen, L. B.; Jørgensen, S.; Kjaergaard, H. G.; Canagaratna, M.; Maso, M. D.; Berndt, T.; Petäjä, T.; Wahner, A.; Kerminen, V.-M.; Kulmala, M.; Worsnop, D. R.; Wildt, J.; Mentel, T. F., A large source of low-volatility secondary organic aerosol. *Nature* **2014,** *506* (7489), 476-479.
227. Scott, C. E.; Spracklen, D. V.; Pierce, J. R.; Riipinen, I.; D'Andrea, S. D.; Rap, A.; Carslaw, K. S.; Forster, P. M.; Artaxo, P.; Kulmala, M.; Rizzo, L. V.; Swietlicki, E.; Mann, G. W.; Pringle, K. J., Impact of gas-to-particle partitioning approaches on the simulated radiative effects of biogenic secondary organic aerosol. *Atmos. Chem. Phys.* **2015,** *15* (22), 12989-13001.
228. Riipinen, I.; Yli-Juuti, T.; Pierce, J. R.; Petäjä, T.; Worsnop, D. R.; Kulmala, M.; Donahue, N. M., The contribution of organics to atmospheric nanoparticle growth. *Nature Geoscience* **2012,** *5* (7), 453-458.
229. Seinfeld, J. H.; Pandis, S. N., *Atmospheric Chemistry and Physics*. John Wiley & Sons, Inc.: NJ, 2016.

230. Au - Zhang, Y.; Au - Gong, Z.; Au - Sa, S. d.; Au - Bateman, A. P.; Au - Liu, Y.; Au - Li, Y.; Au - Geiger, F. M.; Au - Martin, S. T., Production and Measurement of Organic Particulate Matter in the Harvard Environmental Chamber. *JoVE* **2018,** (141), e55685.
231. Jimenez, J. L.; Canagaratna, M. R.; Donahue, N. M.; Prevot, A. S. H.; Zhang, Q.; Kroll, J. H.; DeCarlo, P. F.; Allan, J. D.; Coe, H.; Ng, N. L.; Aiken, A. C.; Docherty, K. S.; Ulbrich, I. M.; Grieshop, A. P.; Robinson, A. L.; Duplissy, J.; Smith, J. D.; Wilson, K. R.; Lanz, V. A.; Hueglin, C.; Sun, Y. L.; Tian, J.; Laaksonen, A.; Raatikainen, T.; Rautiainen, J.; Vaattovaara, P.; Ehn, M.; Kulmala, M.; Tomlinson, J. M.; Collins, D. R.; Cubison, M. J.; Dunlea, J.; Huffman, J. A.; Onasch, T. B.; Alfarra, M. R.; Williams, P. I.; Bower, K.; Kondo, Y.; Schneider, J.; Drewnick, F.; Borrmann, S.; Weimer, S.; Demerjian, K.; Salcedo, D.; Cottrell, L.; Griffin, R.; Takami, A.; Miyoshi, T.; Hatakeyama, S.; Shimono, A.; Sun, J. Y.; Zhang, Y. M.; Dzepina, K.; Kimmel, J. R.; Sueper, D.; Jayne, J. T.; Herndon, S. C.; Trimborn, A. M.; Williams, L. R.; Wood, E. C.; Middlebrook, A. M.; Kolb, C. E.; Baltensperger, U.; Worsnop, D. R., Evolution of Organic Aerosols in the Atmosphere. *Science* **2009,** *326* (5959), 1525.
232. Ng, N. L.; Canagaratna, M. R.; Zhang, Q.; Jimenez, J. L.; Tian, J.; Ulbrich, I. M.; Kroll, J. H.; Docherty, K. S.; Chhabra, P. S.; Bahreini, R.; Murphy, S. M.; Seinfeld, J. H.; Hildebrandt, L.; Donahue, N. M.; DeCarlo, P. F.; Lanz, V. A.; Prévôt, A. S. H.; Dinar, E.; Rudich, Y.; Worsnop, D. R., Organic aerosol components observed in Northern Hemispheric datasets from Aerosol Mass Spectrometry. *Atmos. Chem. Phys.* **2010,** *10* (10), 4625-4641.
233. Zhang, H.; Yee, L. D.; Lee, B. H.; Curtis, M. P.; Worton, D. R.; Isaacman-VanWertz, G.; Offenberg, J. H.; Lewandowski, M.; Kleindienst, T. E.; Beaver, M. R.; Holder, A. L.; Lonneman, W. A.; Docherty, K. S.; Jaoui, M.; Pye, H. O. T.; Hu, W.; Day, D. A.; Campuzano-Jost, P.; Jimenez, J. L.; Guo, H.; Weber, R. J.; de Gouw, J.; Koss, A. R.; Edgerton, E. S.; Brune, W.; Mohr, C.; Lopez-Hilfiker, F. D.; Lutz, A.; Kreisberg, N. M.; Spielman, S. R.; Hering, S. V.; Wilson, K. R.; Thornton, J. A.; Goldstein, A. H., Monoterpenes are the largest source of summertime organic aerosol in the southeastern United States. *Proceedings of the National Academy of Sciences* **2018,** *115* (9), 2038.
234. Khan, F.; Kwapiszewska, K.; Zhang, Y.; Chen, Y.; Lambe, A. T.; Kołodziejczyk, A.; Jalal, N.; Rudzinski, K.; Martínez-Romero, A.; Fry, R. C.; Surratt, J. D.; Szmigielski, R., Toxicological Responses of α-Pinene-Derived Secondary Organic Aerosol and Its Molecular Tracers in Human Lung Cell Lines. *Chemical Research in Toxicology* **2021,** *34* (3), 817-832.
235. Chowdhury, P. H.; He, Q.; Lasitza Male, T.; Brune, W. H.; Rudich, Y.; Pardo, M., Exposure of Lung Epithelial Cells to Photochemically Aged Secondary Organic Aerosol Shows Increased Toxic Effects. *Environmental Science & Technology Letters* **2018,** *5* (7), 424-430.
236. Chowdhury, P. H.; He, Q.; Carmieli, R.; Li, C.; Rudich, Y.; Pardo, M., Connecting the Oxidative Potential of Secondary Organic Aerosols with Reactive Oxygen Species in Exposed Lung Cells. *Environmental Science & Technology* **2019,** *53* (23), 13949-13958.
237. Jason D. Surratt, Y.-H. L., Maiko Arashiro, William G. Vizuete, Zhenfa Zhang, Avram Gold, Ilona Jaspers, and Rebecca C. Fry *Understanding the Early Biological Effects of Isoprene-Derived Particulate Matter Enhanced by Anthropogenic Pollutants*; Health Effects Institute: Boston, Massachusetts, 2019.
238. Guenther, A.; Jiang, X.; Shah, T.; Huang, L.; Kemball-Cook, S.; Yarwood, G. In *Model of Emissions of Gases and Aerosol from Nature Version 3 (MEGAN3) for Estimating Biogenic Emissions*, Air Pollution Modeling and its Application XXVI, Cham, 2020//; Mensink, C.; Gong, W.; Hakami, A., Eds. Springer International Publishing: Cham, 2020; pp 187-192.

239. Guenther, A.; Karl, T.; Harley, P.; Wiedinmyer, C.; Palmer, P. I.; Geron, C., Estimates of global terrestrial isoprene emissions using MEGAN (Model of Emissions of Gases and Aerosols from Nature). *Atmospheric Chemistry & Physics* **2006,** *6*, 3181.
240. Paulot, F.; Crounse Jd Fau - Kjaergaard, H. G.; Kjaergaard Hg Fau - Kürten, A.; Kürten A Fau - St Clair, J. M.; St Clair Jm Fau - Seinfeld, J. H.; Seinfeld Jh Fau - Wennberg, P. O.; Wennberg, P. O., Unexpected epoxide formation in the gas-phase photooxidation of isoprene. (1095-9203 (Electronic)).
241. Bates, K. H.; Crounse, J. D.; St. Clair, J. M.; Bennett, N. B.; Nguyen, T. B.; Seinfeld, J. H.; Stoltz, B. M.; Wennberg, P. O., Gas Phase Production and Loss of Isoprene Epoxydiols. *The Journal of Physical Chemistry A* **2014,** *118* (7), 1237-1246.
242. Jang, M.; Czoschke, N. M.; Lee, S.; Kamens, R. M., Heterogeneous Atmospheric Aerosol Production by Acid-Catalyzed Particle-Phase Reactions. *Science* **2002,** *298* (5594), 814.
243. Czoschke, N. M.; Jang, M.; Kamens, R. M., Effect of acidic seed on biogenic secondary organic aerosol growth. *Atmospheric Environment* **2003,** *37* (30), 4287-4299.
244. Budisulistiorini, S. H.; Baumann, K.; Edgerton, E. S.; Bairai, S. T.; Mueller, S.; Shaw, S. L.; Knipping, E. M.; Gold, A.; Surratt, J. D., Seasonal characterization of submicron aerosol chemical composition and organic aerosol sources in the southeastern United States: Atlanta, Georgia,and Look Rock, Tennessee. *Atmos. Chem. Phys.* **2016,** *16* (8), 5171-5189.
245. Xu, L.; Guo, H.; Boyd, C. M.; Klein, M.; Bougiatioti, A.; Cerully, K. M.; Hite, J. R.; Isaacman-VanWertz, G.; Kreisberg, N. M.; Knote, C.; Olson, K.; Koss, A.; Goldstein, A. H.; Hering, S. V.; de Gouw, J.; Baumann, K.; Lee, S.-H.; Nenes, A.; Weber, R. J.; Ng, N. L., Effects of anthropogenic emissions on aerosol formation from isoprene and monoterpenes in the southeastern United States. *Proceedings of the National Academy of Sciences* **2015,** *112* (1), 37.
246. Budisulistiorini, S. H.; Li, X.; Bairai, S. T.; Renfro, J.; Liu, Y.; Liu, Y. J.; McKinney, K. A.; Martin, S. T.; McNeill, V. F.; Pye, H. O. T.; Nenes, A.; Neff, M. E.; Stone, E. A.; Mueller, S.; Knote, C.; Shaw, S. L.; Zhang, Z.; Gold, A.; Surratt, J. D., Examining the effects of anthropogenic emissions on isoprene-derived secondary organic aerosol formation during the 2013 Southern Oxidant and Aerosol Study (SOAS) at the Look Rock, Tennessee ground site. *Atmos. Chem. Phys.* **2015,** *15* (15), 8871-8888.
247. Budisulistiorini, S. H.; Canagaratna, M. R.; Croteau, P. L.; Marth, W. J.; Baumann, K.; Edgerton, E. S.; Shaw, S. L.; Knipping, E. M.; Worsnop, D. R.; Jayne, J. T.; Gold, A.; Surratt, J. D., Real-Time Continuous Characterization of Secondary Organic Aerosol Derived from Isoprene Epoxydiols in Downtown Atlanta, Georgia, Using the Aerodyne Aerosol Chemical Speciation Monitor. *Environmental Science & Technology* **2013,** *47* (11), 5686-5694.
248. Hu, W. W.; Campuzano-Jost, P.; Palm, B. B.; Day, D. A.; Ortega, A. M.; Hayes, P. L.; Krechmer, J. E.; Chen, Q.; Kuwata, M.; Liu, Y. J.; de Sá, S. S.; McKinney, K.; Martin, S. T.; Hu, M.; Budisulistiorini, S. H.; Riva, M.; Surratt, J. D.; St. Clair, J. M.; Isaacman-Van Wertz, G.; Yee, L. D.; Goldstein, A. H.; Carbone, S.; Brito, J.; Artaxo, P.; de Gouw, J. A.; Koss, A.; Wisthaler, A.; Mikoviny, T.; Karl, T.; Kaser, L.; Jud, W.; Hansel, A.; Docherty, K. S.; Alexander, M. L.; Robinson, N. H.; Coe, H.; Allan, J. D.; Canagaratna, M. R.; Paulot, F.; Jimenez, J. L., Characterization of a real-time tracer for isoprene epoxydiols-derived secondary organic aerosol (IEPOX-SOA) from aerosol mass spectrometer measurements. *Atmos. Chem. Phys.* **2015,** *15* (20), 11807-11833.
249. Chan, L. P.; Chan, C. K., Role of the Aerosol Phase State in Ammonia/Amines Exchange Reactions. *Environmental Science & Technology* **2013,** *47* (11), 5755-5762.

250. Pajunoja, A.; Malila, J.; Hao, L.; Joutsensaari, J.; Lehtinen, K. E. J.; Virtanen, A., Estimating the Viscosity Range of SOA Particles Based on Their Coalescence Time. *Aerosol Science and Technology* **2014,** *48* (2), i-iv.
251. Claeys, M.; Graham, B.; Vas, G.; Wang, W.; Vermeylen, R.; Pashynska, V.; Cafmeyer, J.; Guyon, P.; Andreae, M. O.; Artaxo, P.; Maenhaut, W., Formation of Secondary Organic Aerosols Through Photooxidation of Isoprene. *Science* **2004,** *303* (5661), 1173.
252. Claeys, M.; Wang, W.; Ion, A. C.; Kourtchev, I.; Gelencsér, A.; Maenhaut, W., Formation of secondary organic aerosols from isoprene and its gas-phase oxidation products through reaction with hydrogen peroxide. *Atmospheric Environment* **2004,** *38* (25), 4093-4098.
253. Lin, Y.-H.; Budisulistiorini, S. H.; Chu, K.; Siejack, R. A.; Zhang, H.; Riva, M.; Zhang, Z.; Gold, A.; Kautzman, K. E.; Surratt, J. D., Light-Absorbing Oligomer Formation in Secondary Organic Aerosol from Reactive Uptake of Isoprene Epoxydiols. *Environmental Science & Technology* **2014,** *48* (20), 12012-12021.
254. Veghte, D. P.; Altaf, M. B.; Freedman, M. A., Size Dependence of the Structure of Organic Aerosol. *Journal of the American Chemical Society* **2013,** *135* (43), 16046-16049.
255. Lienhard, D. M.; Huisman, A. J.; Krieger, U. K.; Rudich, Y.; Marcolli, C.; Luo, B. P.; Bones, D. L.; Reid, J. P.; Lambe, A. T.; Canagaratna, M. R.; Davidovits, P.; Onasch, T. B.; Worsnop, D. R.; Steimer, S. S.; Koop, T.; Peter, T., Viscous organic aerosol particles in the upper troposphere: diffusivity-controlled water uptake and ice nucleation? *Atmos. Chem. Phys.* **2015,** *15* (23), 13599-13613.
256. Zhou, S.; Hwang, B. C. H.; Lakey, P. S. J.; Zuend, A.; Abbatt, J. P. D.; Shiraiwa, M., Multiphase reactivity of polycyclic aromatic hydrocarbons is driven by phase separation and diffusion limitations. *Proceedings of the National Academy of Sciences* **2019,** *116* (24), 11658.
257. Drozd, G.; Woo, J.; McNeill, V. F., Self-limited uptake of α-pinene oxide to acidic aerosol: The effects of liquid-liquid phase separation and implications for the formation of secondary organic aerosol and organosulfates from epoxides. *Atmospheric Chemistry & Physics Discussions* **2013,** *13*, 7151-7174.
258. Guo, H.; Otjes, R.; Schlag, P.; Kiendler-Scharr, A.; Nenes, A.; Weber, R. J., Effectiveness of ammonia reduction on control of fine particle nitrate. *Atmos. Chem. Phys.* **2018,** *18* (16), 12241-12256.
259. Rindelaub, J. D.; McAvey, K. M.; Shepson, P. B., The photochemical production of organic nitrates from α-pinene and loss via acid-dependent particle phase hydrolysis. *Atmospheric Environment* **2015,** *100*, 193-201.
260. Dubois, C.; Cholleton, D.; Gemayel, R.; Chen, Y.; Surratt, J. D.; George, C.; Rairoux, P.; Miffre, A.; Riva, M., Decrease in sulfate aerosol light backscattering by reactive uptake of isoprene epoxydiols. *Physical Chemistry Chemical Physics* **2021**.
261. Nenes, A.; Krom, M. D.; Mihalopoulos, N.; Van Cappellen, P.; Shi, Z.; Bougiatioti, A.; Zarmpas, P.; Herut, B., Atmospheric acidification of mineral aerosols: a source of bioavailable phosphorus for the oceans. *Atmos. Chem. Phys.* **2011,** *11* (13), 6265-6272.
262. Battaglia, M. A.; Douglas, S.; Hennigan, C. J., Effect of the Urban Heat Island on Aerosol pH. *Environmental Science & Technology* **2017,** *51* (22), 13095-13103.
263. Bondy, A. L.; Wang, B.; Laskin, A.; Craig, R. L.; Nhliziyo, M. V.; Bertman, S. B.; Pratt, K. A.; Shepson, P. B.; Ault, A. P., Inland Sea Spray Aerosol Transport and Incomplete Chloride Depletion: Varying Degrees of Reactive Processing Observed during SOAS. *Environmental Science & Technology* **2017,** *51* (17), 9533-9542.

264. Riva, M.; Budisulistiorini, S. H.; Chen, Y.; Zhang, Z.; D'Ambro, E. L.; Zhang, X.; Gold, A.; Turpin, B. J.; Thornton, J. A.; Canagaratna, M. R.; Surratt, J. D., Chemical Characterization of Secondary Organic Aerosol from Oxidation of Isoprene Hydroxyhydroperoxides. *Environmental Science & Technology* **2016,** *50* (18), 9889-9899.
265. Cui, T.; Zeng, Z.; dos Santos, E. O.; Zhang, Z.; Chen, Y.; Zhang, Y.; Rose, C. A.; Budisulistiorini, S. H.; Collins, L. B.; Bodnar, W. M.; de Souza, R. A. F.; Martin, S. T.; Machado, C. M. D.; Turpin, B. J.; Gold, A.; Ault, A. P.; Surratt, J. D., Development of a hydrophilic interaction liquid chromatography (HILIC) method for the chemical characterization of water-soluble isoprene epoxydiol (IEPOX)-derived secondary organic aerosol. *Environmental Science: Processes & Impacts* **2018,** *20* (11), 1524-1536.
266. Imre, D. G.; Xu, J.; Tang, I. N.; McGraw, R., Ammonium Bisulfate/Water Equilibrium and Metastability Phase Diagrams. *The Journal of Physical Chemistry A* **1997,** *101* (23), 4191-4195.
267. Cziczo, D. J.; Abbatt, J. P. D., Deliquescence, efflorescence, and supercooling of ammonium sulfate aerosols at low temperature: Implications for cirrus cloud formation and aerosol phase in the atmosphere. *Journal of Geophysical Research: Atmospheres* **1999,** *104* (D11), 13781-13790.
268. Cheng, Z.; Sharma, N.; Tseng, K.-P.; Kovarik, L.; China, S., Direct observation and assessment of phase states of ambient and lab-generated sub-micron particles upon humidification. *RSC Advances* **2021,** *11* (25), 15264-15272.
269. Ault, A. P.; Moffet, R. C.; Baltrusaitis, J.; Collins, D. B.; Ruppel, M. J.; Cuadra-Rodriguez, L. A.; Zhao, D.; Guasco, T. L.; Ebben, C. J.; Geiger, F. M.; Bertram, T. H.; Prather, K. A.; Grassian, V. H., Size-Dependent Changes in Sea Spray Aerosol Composition and Properties with Different Seawater Conditions. *Environmental Science & Technology* **2013,** *47* (11), 5603-5612.
270. May, N. W.; Axson, J. L.; Watson, A.; Pratt, K. A.; Ault, A. P., Lake spray aerosol generation: a method for producing representative particles from freshwater wave breaking. *Atmos. Meas. Tech.* **2016,** *9* (9), 4311-4325.
271. Vargas Jentzsch, P.; Kampe, B.; Ciobotă, V.; Rösch, P.; Popp, J., Inorganic salts in atmospheric particulate matter: Raman spectroscopy as an analytical tool. *Spectrochimica Acta Part A: Molecular and Biomolecular Spectroscopy* **2013,** *115*, 697-708.
272. Doughty, D. C.; Hill, S. C., Raman spectra of atmospheric aerosol particles: Clusters and time-series for a 22.5 hr sampling period. *Journal of Quantitative Spectroscopy and Radiative Transfer* **2020,** *248*, 106907.
273. Eddingsaas, N. C.; VanderVelde, D. G.; Wennberg, P. O., Kinetics and Products of the Acid-Catalyzed Ring-Opening of Atmospherically Relevant Butyl Epoxy Alcohols. *The Journal of Physical Chemistry A* **2010,** *114* (31), 8106-8113.
274. Piletic, I. R.; Edney, E. O.; Bartolotti, L. J., A computational study of acid catalyzed aerosol reactions of atmospherically relevant epoxides. *Physical Chemistry Chemical Physics* **2013,** *15* (41), 18065-18076.
275. Fitzgerald, E.; Ault, A. P.; Zauscher, M. D.; Mayol-Bracero, O. L.; Prather, K. A., Comparison of the mixing state of long-range transported Asian and African mineral dust. *Atmos. Environ.* **2015,** *115*, 19-25.
276. Gunsch, M. J.; May, N. W.; Wen, M.; Bottenus, C. L. H.; Gardner, D. J.; VanReken, T. M.; Bertman, S. B.; Hopke, P. K.; Ault, A. P.; Pratt, K. A., Ubiquitous influence of wildfire

emissions and secondary organic aerosol on summertime atmospheric aerosol in the forested Great Lakes region. *Atmos. Chem. Phys.* **2018,** *18* (5), 3701-3715.
277. Gunsch, M. J.; Schmidt, S. A.; Gardner, D. J.; Bondy, A. L.; May, N. W.; Bertman, S. B.; Pratt, K. A.; Ault, A. P., Particle growth in an isoprene-rich forest: Influences of urban, wildfire, and biogenic air masses. *Atmos. Environ.* **2018,** *178*, 255-264.
278. May, N. W.; Gunsch, M. J.; Olson, N. E.; Bondy, A. L.; Kirpes, R. M.; Bertman, S. B.; China, S.; Laskin, A.; Hopke, P. K.; Ault, A. P.; Pratt, K. A., Unexpected Contributions of Sea Spray and Lake Spray Aerosol to Inland Particulate Matter. *Env. Sci. Tech. Lett.* **2018,** *5* (7), 405-412.
279. Einstein, A., The motion of elements suspended in static liquids as claimed in the molecular kinetic theory of heat. *Annalen der Physik* **1905,** *322* (8), 549-560.
280. Seinfeld, J. H. a. P., S.N., *Atmospheric Chemistry and Physics: From Air Pollution to Climate Change.* John Wiley & Sons: Hoboken, 2016.
281. Shiraiwa, M.; Ammann, M.; Koop, T.; Pöschl, U., Gas uptake and chemical aging of semisolid organic aerosol particles. *Proceedings of the National Academy of Sciences* **2011,** *108* (27), 11003-11008.
282. Renbaum-Wolff, L.; Grayson, J. W.; Bertram, A. K., Technical Note: New methodology for measuring viscosities in small volumes characteristic of environmental chamber particle samples. *Atmos. Chem. Phys.* **2013,** *13* (2), 791-802.
283. Dette, H. P.; Qi, M.; Schroder, D. C.; Godt, A.; Koop, T., Glass-forming properties of 3-methylbutane-1,2,3-tricarboxylic acid and its mixtures with water and pinonic acid. *J Phys Chem A* **2014,** *118* (34), 7024-33.
284. Bzdek, B. R.; Collard, L.; Sprittles, J. E.; Hudson, A. J.; Reid, J. P., Dynamic measurements and simulations of airborne picolitre-droplet coalescence in holographic optical tweezers. *J Chem Phys* **2016,** *145* (5), 054502.
285. Bateman, A. P.; Belassein, H.; Martin, S. T., Impactor Apparatus for the Study of Particle Rebound: Relative Humidity and Capillary Forces. *Aerosol Science and Technology* **2014,** *48* (1), 42-52.
286. Brizuela, A. B.; Bichara, L. C.; Romano, E.; Yurquina, A.; Locatelli, S.; Brandan, S. A., A complete characterization of the vibrational spectra of sucrose. *Carbohydr Res* **2012,** *361*, 212-8.
287. Slade, L.; Levine, H., Water and the Glass Transition — Dependence of the Glass Transition on Composition and Chemical Structure: Special Implications for Flour Functionality in Cookie Baking**The full version of this paper, complete with ali Tables and accompanying references, will appear in a later issue of Journal of Food Engineering. (Slade, L. & Levine, H. (1994). J. Food Engng, in press). In *Water in Foods*, Fito, P.; Mulet, A.; McKenna, B., Eds. Pergamon: Amsterdam, 1994; pp 143-188.
288. Kalika, D. S.; Gibson, D. G.; Quiram, D. J.; Register, R. A., Relationship between morphology and glass transition temperature in solvent-crystallized poly(aryl ether ketones). *Journal of Polymer Science Part B: Polymer Physics* **1998,** *36* (1), 65-73.
289. Drake, A. C.; Lee, Y.; Burgess, E. M.; Karlsson, J. O. M.; Eroglu, A.; Higgins, A. Z., Effect of water content on the glass transition temperature of mixtures of sugars, polymers, and penetrating cryoprotectants in physiological buffer. *PLoS One* **2018,** *13* (1), e0190713.
290. Kumar, B. R.; Rao, T. S., AFM Studies on surface morphology, topography and texture of nanostructured zinc aluminum oxide thin films. *Dig. J. Nanomater. Bios.* **2012,** *7* (4), 1881-1889.

291. Potukuchi, S.; Wexler, A. S., Identifying solid-aqueous phase transitions in atmospheric aerosols—I. Neutral-acidity solutions. *Atmospheric Environment* **1995,** *29* (14), 1663-1676.
292. Atha, D. H.; Gaigalas, A. K.; Reipa, V., Structural Analysis of Heparin by Raman Spectroscopy. *Journal of Pharmaceutical Sciences* **1996,** *85* (1), 52-56.
293. Ghosh, A.; Raha, S.; Dey, S.; Chatterjee, K.; Roy Chowdhury, A.; Barui, A., Chemometric analysis of integrated FTIR and Raman spectra obtained by non-invasive exfoliative cytology for the screening of oral cancer. *Analyst* **2019,** *144* (4), 1309-1325.
294. Hodgman, C. D., *Handbook of Chemistry and Physics: A Ready-Reference Book of Chemical and Physical Data*. Chemical Rubber Company: Cleveland, Ohio, 1961.